

Master Thesis

Experimental Characterization and Optimization of a High-Resolution X-Ray Grating Interferometer Setup With Respect to Material Research

MARKUS BAIER

Tuesday 17th November, 2015

Supervisor: Prof. Dr. Franz Pfeiffer



Physics Department

Technische Universität München



Acknowledgements

I would like to thank various people for their help and support during the last year. First of all, my sincere gratitude belongs to Franz Pfeiffer, who gave me the opportunity to be a part of his group for preparing my thesis and who had always an open ear for helpfully answering my questions.

A big thank you goes to Florian Schaff and Friedrich Prade for introducing me to 'their baby' the high resolution X-ray grating interferometer setup, which I hopefully always treated well in their eyes during my thesis. They also got never tired discussing many aspects of my work and providing me helpful material. Last but not least, I would like to thank them for patiently proof reading my thesis and the very helpful comments and their time they took for me.

Furthermore, I would thank Johannes Wolf for lining up the AMPTEK and the people from the crystallographic laboratory providing me the well polished knife-edge.

Special thanks go to the IMETUM people especially Simone Ferstl, Karin Burger, Jonathan Schock, Pidassa Bidola, Fabio de Marco, Markus Schüttler, Mark Müller and Rico Burkhardt for helping with all kind of issues and the pleasant working atmosphere in the office.

A thank you goes also the whole E17 group for a very nice year in the group and also to the people taking care of the IT related issues.

Finally, I want to thank my family and my girlfriend for their big support during my whole studies and for always being there for me!

Contents

1	Introduction	1
1.1	Outline	2
2	Theory	3
2.1	Interaction of X-rays with matter	3
2.1.1	Complex refraction-index	4
2.1.2	Attenuation	4
2.1.3	Refraction	5
2.2	Phase contrast imaging	6
2.2.1	Wave-Front propagation	6
2.2.2	Talbot effect	7
2.2.3	Grating interferometer	8
2.2.4	Grating Types	9
2.2.5	Coherence requirements	10
2.2.6	Visibility and Phase stepping routine	12
2.2.7	Magnification in curved wave geometry	16
2.2.8	Induced uncertainty by an expanded edge thickness at different magnifications	18
2.3	Spatial system response	21
2.3.1	Real- and frequency-space response functions	21
2.3.2	Edge- and Line- spread function (ESF/LSF)	22
2.3.3	PSF of a complex system	23
3	The Setup	25
3.1	The source	26
3.1.1	Dimensions and structure	26
3.1.2	Properties of the source	28
3.2	Sample handling	29
3.3	Detector properties	29
4	Time- Power-Stability	31
4.1	Time-stability	31
4.2	Power-stability	33

5 SSR characterization	37
5.1 Knife edge measurements	37
5.1.1 Data acquisition	37
5.1.2 Data processing	41
5.1.3 Results and discussion	44
5.1.4 Shape of the source-spot	53
5.2 R-target measurement	56
5.2.1 Data acquisition	56
5.2.2 Data processing	58
5.2.3 Results and discussion	61
5.3 Summary	63
6 Spectra measurements	65
6.1 Measurement procedure of the different spectra	65
6.2 Results and discussion	66
6.2.1 Source spectra at different photon- energies	67
6.2.2 Influence of the gratings onto the source-spectrum	68
6.2.3 Energy resolved phase-stepping and Energy-visibility map	69
6.3 Conclusion	71
7 Application of the obtained results for new measurement structures	73
7.1 Different interferometer setups	73
7.1.1 Measurement procedure	73
7.1.2 Results and Discussion	74
7.2 Electromagnetic phase-stepping	76
7.3 Conclusion	79
8 Summary and Outlook	81
List of Figures	83
List of Tables	84
Glossary	85
Acronyms	87
Bibliography	89

1 Introduction

The ability of X-rays to penetrate matter makes them an indispensable tool in both medical diagnostics as well as non destructive testing. Especially for industrial applications, where radiation dose and measurement time are not nearly as big of a defining factor as with all medical applications, a high spatial resolution is often times desired. This can be achieved using X-ray tubes with very small spot-sizes. In addition the recent invention of interferometer setups for X-ray phase-contrast imaging [8] can be used to enhance image quality, both for industrial and clinical applications. Subsequent the combination of both, small spot-sizes and such interferometer setups is capable to further increase the image quality.

In order to be able to optimize imaging results, the exact investigation of the properties of the measurement setup is just as important as the investigation of samples itself. An imaging system consists of several different parts that need to be characterized, e.g. the source, detector and possible additional parts such as a grating interferometer. This may help understand the origin of artefacts, which are often induced by intrinsic properties of the setup. Subsequently, the knowledge of e.g. the behaviour of the Point-spread-function (PSF) of the entire system can be used to correct the images for some artefacts.

Hence, this thesis is based on the characterization and optimization of a high-resolution X-ray interferometer setup for material research. The setup consists of a micro-focus X-ray tube [42], a Varian flat-panel detector [33], as used for medical imaging, and a Talbot-Lau grating-interferometer [25]. A grating-interferometer can be built by a minimum of two gratings, whereupon in the case of a Talbot-Lau interferometer a third grating is added in front of the source to reach sufficiently high spatial coherence. Without this third grating the Talbot pattern vanishes caused by the extent of the source size.

The thesis is mainly focussed on the characterization of the source properties, especially on the determination of the spot-size with different techniques, the influence of the interferometer parts onto the flux and the source spectrum, and the investigation of new measurement methods which can be derived from the results obtained by the previous characterization. The main advantage of such micro-focus tubes is the small spot-size in the μm range, which firstly allows for measurements with great geometrical magnification, without losing resolution due to source induced blurring. Secondly, a small source-spot should in principle provide sufficient spatial coherence, so that the source grating can be omitted without losing the ability to perform interferometry measure-

ments. Hence, the determination of the exact spot-size for various X-ray tube settings is of great interest.

1.1 Outline

At the beginning of this thesis, a short introduction about the theory for the different measurements and applied techniques is given. Subsequently, a detailed description of the setup characterized in this thesis is given. Afterwards, the stability of the source with respect to power-output was characterized. Following, the behaviour of the source size for various different acceleration voltages and powers was determined. The spectrum of the source and influences of the interferometer gratings onto the spectrum were investigated followed by the measurement of the energy resolved visibility of the entire setup. Finally, the obtained results were used to proof investigate the possibility of operating the setup without a source grating.

2 Theory

The focus of this thesis lies on the experimental characterization of the micro-focus X-ray setup at the biophysical chair E17 at TUM. There, special care is taken on the source properties and the interferometric parts. Hence the underlying theory of the physical principles of this work are presented restricted to the most essential basics.

The interested reader is referred to the recommendations at the beginning of each section for a detailed overview of the respective topic.

Since the discovery of X-rays by Wilhelm Conrad Roentgen in 1895, several different ways generating X-rays were developed and have since been continuously improved. X-rays used for clinical applications are generally produced using conventional X-ray tubes. In an X-ray tube, electrons are produced by thermal emission from a heated cathode. Applying a strong electric field between cathode and anode the electrons are accelerated towards the anode. Upon hitting the anode the electrons are decelerated under the emission of a broad spectrum of X-rays, known as *Bremsstrahlung*. Additionally, radiation of characteristic energies depending on the anode material is emitted. Detailed description about X-ray sources and the interaction of X-rays with matter can be found in [1, 36].

2.1 Interaction of X-rays with matter

X-rays are part of the electromagnetic spectrum with frequencies lying between the extreme ultraviolet and gamma radiation. The corresponding photon energies range from approximately 100 eV up to a few hundred keV. The relation between the energy and the wavelength of an electromagnetic wave is given by:

$$\lambda [\text{\AA}] = \frac{hc}{E} = \frac{12.398}{E [\text{keV}]} . \quad (2.1)$$

While there is no upper bound for the energy of electromagnetic waves, the wavelengths of X-rays range from 12.4×10^{-10} m at 100 eV down to 0.775×10^{-11} m for 160 keV. The region of a few 100 eV is called soft X-rays, photons of higher energies are called hard X-rays.

2.1.1 Complex refraction-index

Just like visible light, X-rays are electromagnetic waves, thus their behaviour when passing through matter can be described by the complex index of refraction n :[1]

$$n = 1 - \delta + i\beta. \quad (2.2)$$

δ and β depend on the material properties of the traversed medium and the energy of the X-rays. A plane unpolarized monochromatic wave propagating along the z-axis in vacuum ($n = 1$), can be described by a scalar wave function $\Psi(z)$:

$$\Psi(z) = E_0 e^{ikz}. \quad (2.3)$$

Here E_0 is the amplitude of the electric field and $k = 2\pi/\lambda$ the wavenumber. Within a medium this equation changes to:

$$\Psi(z) = E_0 e^{inkz} = E_0 e^{(1-\delta+i\beta)ikz} = E_0 e^{(1-\delta)ikz} e^{-\beta kz} \quad (2.4)$$

with the accumulated phase shift δkz and the attenuation factor $e^{-\beta kz}$ of the wave after travelling a distance z through a medium. The waves and the respective losses are shown in Fig. 2.1. In the following, the macroscopic effects of these two factors are separately discussed.

2.1.2 Attenuation

The attenuation of an electromagnetic wave corresponds to a loss of intensity of the beam. This macroscopic attenuation is dominated over a broad energy range by two main effects: At low energies attenuation is dominated by *photoelectric absorption*, while at high energies *Compton scattering*, an incoherent and inelastic scattering process, becomes prevalent [1]. According to the *Lambert-Beer Law*, the relation between the reduction of intensity and the imaginary part of the refraction index, β , of an object is given by:

$$I(d) = I_0 e^{-2\beta kd} = I_0 e^{-\mu d}, \quad (2.5)$$

with the linear attenuation coefficient $\mu = 4\pi\beta/\lambda$ and the initial intensity I_0 of the wave passing through the object [6]. The linear absorption coefficient μ depends on the incoming wavelength, and thus on the corresponding X-ray energy and the composition of the illuminated material. The formation of images in attenuation-based X-ray imaging is a measure of the material dependent attenuation coefficients as well as the corresponding intensity loss of the X-ray beam after propagating through the studied object.

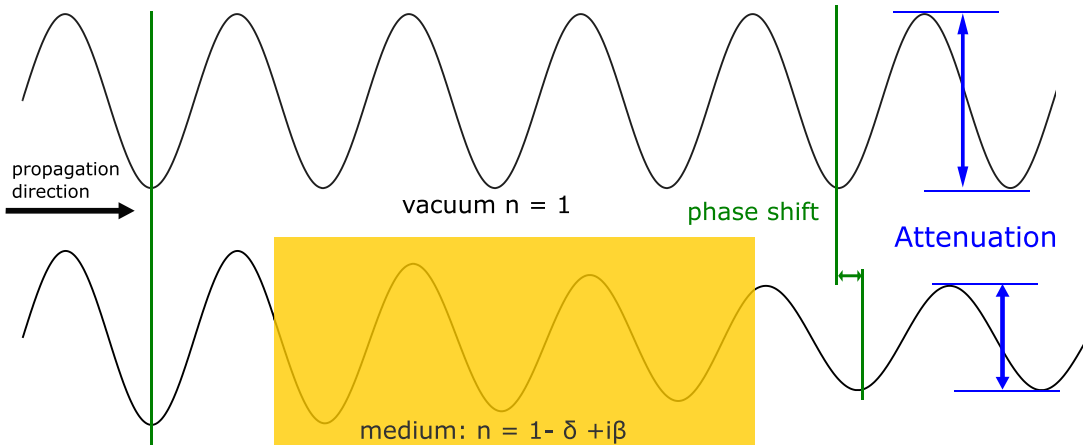


Figure 2.1: Two electromagnetic waves. The upper wave propagates through vacuum while the lower wave travels through a medium with complex index of refraction. The latter experiences an attenuation in amplitude as well as a shift in phase. The attenuation and phase shift are depicted as blue and green arrows, respectively.

2.1.3 Refraction

For a medium of thickness d , the total phase shift Φ is given by the real part of the refractive index, $\delta k z$, in equation 2.4:

$$\Phi = \delta k d. \quad (2.6)$$

For an object which changes in thickness or refractivity in a direction normal to the wave propagation, the total phase shift depends on the position of the sample. Consequently, the propagation direction of the incoming X-ray beam is changed. In general, this angle of refraction α is equivalent to the local gradient of the phase shift perpendicular to the direction of incidence - in this case the z-direction- divided by the wave vector $k = 2\pi/\lambda$. For reasons of simplicity the problem here is restricted to the x-direction and thus the gradient reduces to a simple derivative in x. The corresponding equation for the refraction angle then simplifies to:

$$\alpha = \frac{1}{k} \frac{\partial \Phi(x)}{\partial x}. \quad (2.7)$$

One main difference between visible light and X-rays is the deviation of the refractive index from unity. For visible light, the frequency-dependent index of refraction can deviate appreciably from 1, whereas the deviation of the refractive index for x-rays is very small. Considering the dependencies of the refractive index decrement δ , this behavior becomes easily clear. The material-dependent term δ strongly depends on the energy of the X-ray beam, and is described as:

$$\delta = \frac{\lambda^2 r_e n_e}{2\pi}, \quad (2.8)$$

with the classical electron radius $r_e = 2.818 \times 10^{-15}$ m and the electron density n_e of the material. As an example at energies above 12.4 keV $\equiv 1 \times 10^{-10}$ m δ is of the order of 10^{-6} . This very small effect leads to tiny refraction angles, which makes detecting X-ray refraction very difficult. On the elementary particle level, the process of X-ray refraction can be described by the elastic scattering of the photons at the electrons. This is known as *Thomson scattering* [1]. The key to phase contrast imaging relies on the measurement of these refraction angles. One way to do this is explained further in the following section.

2.2 Phase contrast imaging

There are several different approaches to making changes in the direction of an X-ray beam visible. For this thesis, however, the focus lies on the grating-based phase contrast imaging technique. For further detail about other techniques and the topics in this section see: [4, 5, 22, 25, 36, 39, 40].

2.2.1 Wave-Front propagation

One way to describe electromagnetic waves is to consider them as a wave-front. According to *Huygens principle* a wave-front can be described at any time by the sum of spherical wavelets distributed over the whole border of the wave. This leads to the Fresnel diffraction integral (valid in the homonym *Fresnel regime*, also: near-field regime), which is the integral over the contributions of all spherical waves:

$$\Psi(x, y, z) = \frac{e^{ikz}}{i\lambda z} \int \int \Psi(x_0, y_0, 0) e^{\frac{ik}{2z}((x-x_0)^2 + (y-y_0)^2)} dx_0 dy_0, \quad (2.9)$$

whereupon x_0 and y_0 are the values in the $z = 0$ plane. With this equation it is possible to calculate the wave-front at any point in time.

The propagation itself can be considered as the convolution of the wave function $\Psi(x, y, z)$ at $z = z_0$ with a so called propagator function h_d :

$$h_d = \frac{e^{ikd}}{i\lambda d} e^{\frac{ik(x^2+y^2)}{2d}}, \quad (2.10)$$

where d denotes the propagation distance. With the convolution theorem, stating that the Fourier transform of a convolution of two functions is equal to the product of the Fourier transforms of these two functions, it is possible to propagate the wave-front over a distinct distance by simple multiplication in Fourier space. Here, the Fourier space propagator function $\tilde{P}_d(k_x, k_y)$ is the Fourier transform of the propagator function in real space, denoted by:

$$\tilde{P}_d(k_x, k_y) = \mathcal{F}(h_d(x, y)) = e^{ikd} e^{\frac{-id(k_x^2+k_y^2)}{2k}}, \quad (2.11)$$

which can be shown by simple physical considerations [4].

2.2.2 Talbot effect

The Fourier space propagator is an easy and efficient way to calculate the wave-front at any given propagation distance. In the case of a spatially periodic wave-front, such as sine or a cosine modulated wave-fronts, a self-image can be assumed after a distinct propagation distance. The repeat of a periodic wave-fronts initial shape after a distinct propagation distance was firstly discovered by Henry Fox Talbot in 1836. This distance is known as the Talbot distance d_T [34]. In his studies, Talbot used visible light and a grating to create a periodic wave-front, but the effect is also valid for the X-ray range [8].

The distinct distance the wave-front recreates can be simply calculated by multiplication of equation 2.3 with the propagator function defined in equation 2.2.1. With this calculation it can be shown that a periodic wave-front repeats itself at a certain distance d_T :

$$d_{T_n} = \frac{2np^2}{\lambda}, \quad (2.12)$$

at which $n = 1, 2, 3, \dots$ indicates the Talbot-order. Considering a well known wave-function, as an example a step-function induced by a periodic grating, so called *Fractional Talbot distances* arise [4]. A general relation for the fractional distances created by a phase grating with a phase shift of $\pi/2$ is given by:

$$d_{T_{frac}} = \frac{np^2}{8\lambda}, \quad (2.13)$$

where n again denotes the Talbot order and p the period of the grating. An important feature occurs at half the Talbot distance where the initial intensity pattern exactly repeats, besides of a shift in direction perpendicular to the grating lines. However, at

certain fractional Talbot distances, patterns of alternating low and high intensity arise, which is of great interest for phase contrast imaging using gratings. A main problem is the spectrum illuminating the grating, because the exact revival of the wave-front only appears by use of monochromatic waves. Otherwise the pattern lute due to the fact of to less spatial-coherence. Thus, for the case of a polychromatic spectrum the Talbot carpet has only bright and dark regions, which can be seen on the right side of figure 2.2. Nevertheless, phase contrast imaging is possible at fractional Talbot distances.

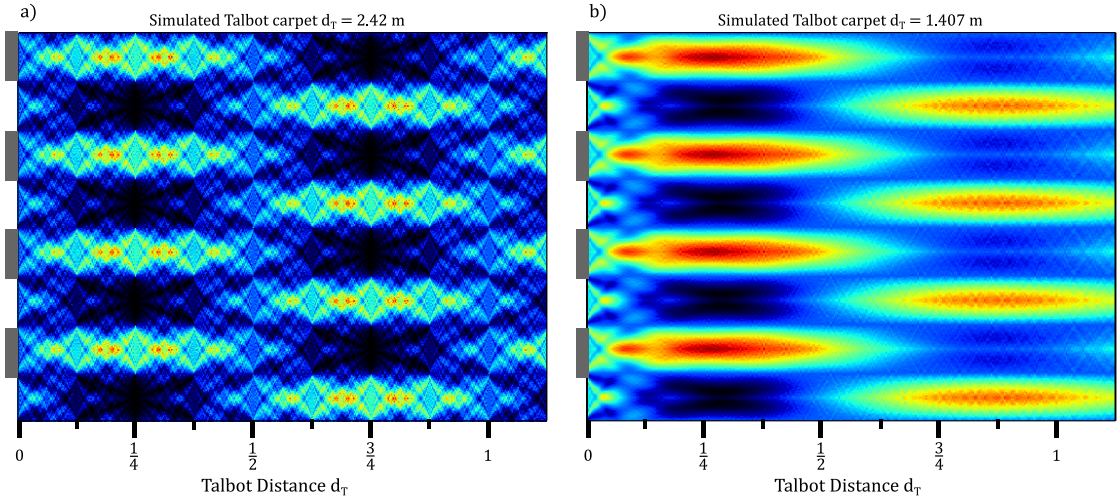


Figure 2.2: Simulated Talbot-carpets for a gold grating with a duty cycle of 0.5 a phase shift of $\pi/2$ and a grating period of $5 \mu\text{m}$. a) Intensity distribution for a monochromatc X-ray source with an x-ray energy of 60 keV. Besides a phase shift the initial wave-front revives at half and after one Talbot distance d_T . In between a strong periodic intensity modulation at $1/4$ and $3/4$ d_T occurs, which matches the period of the simulated grating. b) Simulation results for a polychromatc source, described by a tungsten spectrum with 60 kVp. Due to the polychromatc spectrum the resulting pattern is a superposition of the individual patterns of all energies. The Talbot distance depends on the wavelength and therefore the intensity modulations are smeared out. Hence just high and low contrast regions are still observable.

2.2.3 Grating interferometer

As mentioned in the sections above the underlying principle of phase contrast imaging is to quantify the refractive index distribution of a sample, or in other words to measure the induced angle of refraction onto the transmitted X-ray wave. The idea behind using a grating interferometer for this method is that a small angular change of the wave-front leads to a transverse shift of the interference pattern induced by the grating. In

the optimum case of a perfect wave-front, just two gratings are needed making this technique applicable. In practice, a third grating, is often used to perform grating interferometry measurements at conventional X-ray sources. Such a setup known as Talbot-Lau interferometer is shown in Figure 2.3. Here, the usual first grating, denoted by G_1 , induces a periodic phase-shift onto the wave-front and the second grating, G_2 , serves as analyzer grating. The last grating, G_2 , is ideally placed at a fractional Talbot distance and makes detection of the very fine interference pattern with standard X-ray detectors feasible. Regions around odd fractional Talbot distances have a high visibility of the interference pattern, which is explained in further detail in 2.2.6 and can also be seen on the left side in Figure 2.2, e.g. speaking of $d = 1/4 d_T$, where the Talbot-carpet has a region of highest contrast. In general there is a huge lack between the optimum requirements and the existing properties of source and gratings. Nevertheless, the requirements of the source can be overcome by introducing a third grating, G_0 , right behind the source. At this installation the third grating G_0 , which is an absorption grating, works as a mask for the spacious source, normally used at clinical applications or at laboratories, with a source size unable to provide sufficient spatial-coherence. This grating slices the source in evenly spaced individually coherent line-sources which interfere with each-other. In such a setting, it is important that the following condition is fulfilled:

$$p_0 = p_2 \times \frac{l}{d}. \quad (2.14)$$

Then the individual line-sources interfere constructively and can contribute to the imaging process. Hereby, p_0 and p_2 are the respective grating period, l is the distance between G_0 and G_1 and d the distance between G_1 and G_2 . Using this alignment the total source size S is only responsible for the final resolution of the image given by Sd/l and spatial resolution is decoupled from spatial-coherence, allowing the use of X-rays with very small coherence length in both directions [25].

2.2.4 Grating Types

In general there are two different grating types, absorption and phase gratings. As one can imagine, the main property of absorption gratings is their high ability to strongly absorb X-rays. For that reason, the material they are made of has to have high electron density, and thus a high atomic number Z e.g. lead or gold. The better choice for the production is gold, at one hand, because the absorption performance compared to lead is twice as good. At the other hand the electroplating mechanisms are better understood. Overcoming the softness of gold, absorption gratings are formed using a support layer generally made of silicon, because the handling of Si wavers and their subsequent treatment is well known. There are several ways to produce an absorption grating, one is the Lithography and Galvanization (LIGA) process [27]. During this process, a supporting structure is produced from a photo-resist using x-ray lithography and deep reactive ion etching. The trenches are then filled with gold by electroplating. In the main part of figure 2.4 such an absorption grating with a gold height of $50\ \mu\text{m}$

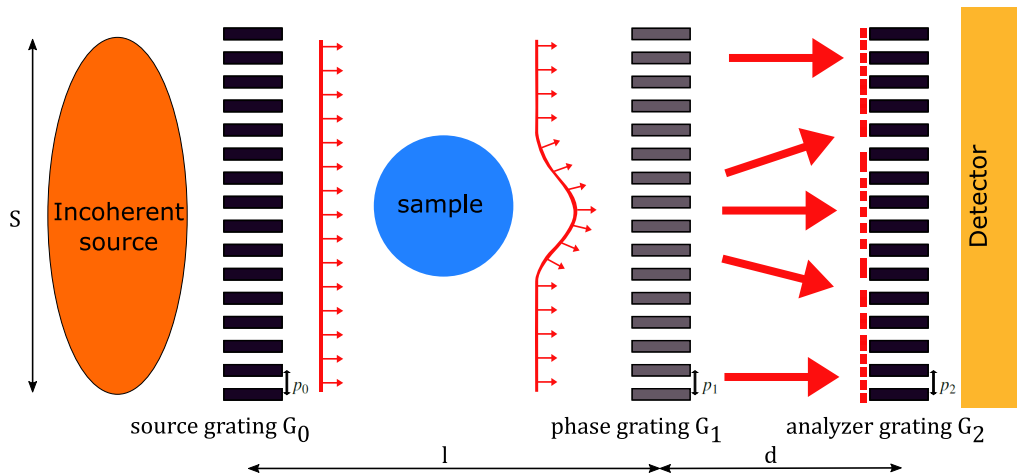


Figure 2.3: Sketch of a Talbot-Lau interferometer. Underlying principle: The source grating G_0 induces individual coherent, but not mutual coherent, line-sources. Refraction caused by intrinsic sample properties, induces distortions of the wave-front. These very tiny changes of the interference pattern created by the phase grating G_1 , are then recorded by a standard X-ray detector, by dint of G_2 .

and a grating period of $2.4\text{ }\mu\text{m}$ is shown. In general, a higher gold filling is preferred as it corresponds to a better X-ray absorption. However, forming such high gratings with a period of only a few micrometers is very difficult. Nowadays, grating heights up to $200\text{ }\mu\text{m}$ are possible over large areas [27]. Phase gratings usually consist of low Z materials in order to avoid absorption when introducing the desired phase-shift. Due to the fact that high absorption is not desired, the height of phase gratings furthermore is way lower than that of absorption gratings. The inset of figure 2.4 shows such a phase grating made of silicon with a height of $22\text{ }\mu\text{m}$ and a period of $4\text{ }\mu\text{m}$, but there are also various combinations of materials forming such gratings e.g. a silicon grating electroplated with nickel, which is usually used at the setup, used during the work presented in this thesis. For further reading about production mechanisms and the different grating types see: [14, 21]

2.2.5 Coherence requirements

As mentioned in section 2.2.3 the coherence requirements of the source can be relaxed by inserting a third grating (G_0) right behind the source. In this section an overview about the relevant equations and parameters are introduced, in order to get a feeling about the required dimensions. For further reading see [22, 39]. There are two important parameters in order to describe the coherence properties of X-rays. On one hand, the longitudinal coherence length is related to the bandwidth of the used source spec-

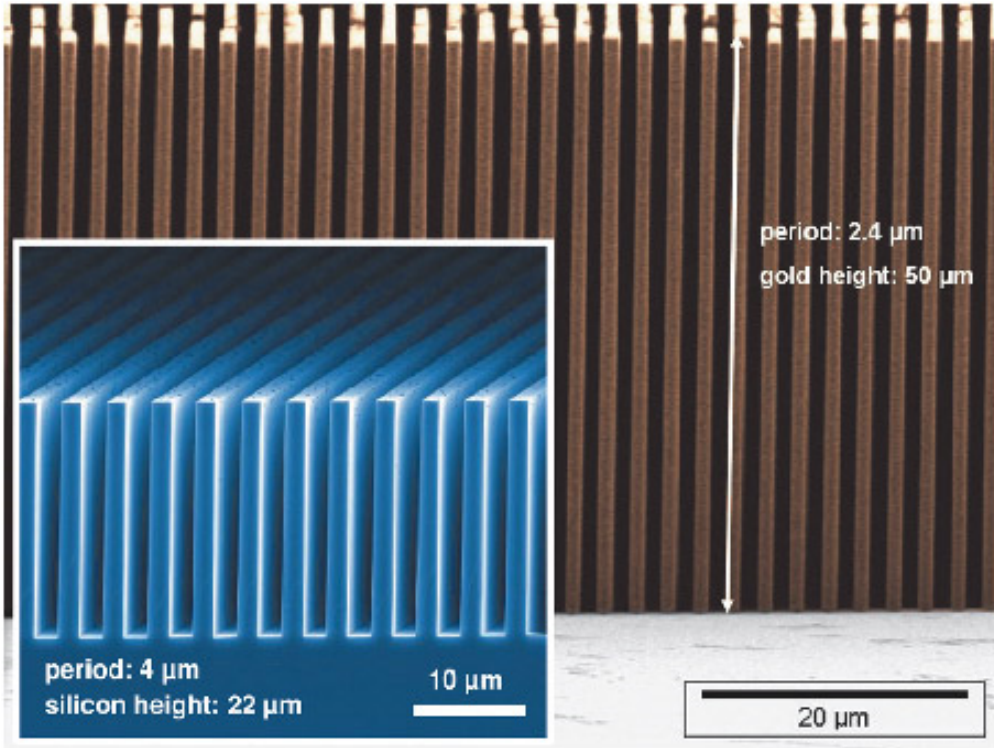


Figure 2.4: Different types of deep micro-structured gratings feasible for X-ray grating interferometry. Dependent on the properties of the respective grating phase and/or amplitude modulation is possible. In the main picture a Gold absorption grating is depicted manufactured at KIT. At the inset a pure Silicon phase grating made at the PSI is shown. source: <http://www.esrf.eu/UsersAndScience/Publications/Highlights/2010/imaging/img02>

trum. Concerning the longitudinal coherence an approximate expression for the required monochromaticity yielding to good fringe contrast in the interference pattern is [40]:

$$\frac{\lambda_0}{\Delta\lambda} \gtrsim n. \quad (2.15)$$

Here λ_0 denotes the design wavelength of the setup, $\Delta\lambda$ the width of the luting of the design wavelength and n the order of the Talbot distance from equation 2.12. This expression implies the possibility, to apply a polychromatic source for grating interferometry, without loosing significant contrast quality between the particular fringes. For that reason, this section focusses on the spatial coherence requirements, because their influence onto the resulting signal is much higher. As mentioned in section 2.2.3 for the

case of just considering plane-waves the final resolution of an image is given by Sd/l . A sketch of these variables is shown in Fig: 2.3 where S is the finite source size, l the distance between G_0 and G_1 and d the distance between G_1 and G_2 , respectively. There are several common definitions for the transversal coherence length ζ_s existing alongside to each other so here ζ_s is defined as [40]:

$$\zeta_s = \frac{\lambda l}{S}, \quad (2.16)$$

where λ is the wavelength corresponding to the design energy of the interferometer. Typical values for an extended source size are about an square millimetre and an integrating distance of about one metre are ζ_s is $\approx 10^{-8}$ m and for more advanced micro-focus tubes with much less power or synchrotrons ζ_s is $\approx 10^{-6}$ m [25]. A comparison between typical and micro-focus X-ray tubes is given in chapter 3. In the following section a compendium of the phase-retrieval mechanism is shown with respect to the coherence requirements mentioned in this section.

2.2.6 Visibility and Phase stepping routine

Visibility The phase grating modulates the phase of the incoming wave-front, so that fringe pattern arise at the position of the analyser grating, which is placed at a fractional Talbot distance. Just concerning first order diffraction [39] this pattern has nearly a sinusoidal shaped intensity profile. The distance d is adjusted to the fractional Talbot-distances with the highest contrast (see Figure 2.2), where the minima of the intensity pattern drop down to zero ¹. Using completely coherent radiation, the intensity profile can be expressed by [39]:

$$I(x) = I_0(1 + \sin(\frac{2\pi x}{p_2})), \quad (2.17)$$

thereby x denotes the coordinate transversal to the grating lines, I_0 the intensity before G_1 and p_2 the period of the fringes. The interferometer should be also designed in that way, that this period coincides with the analyser grating period. For an expanded source with size S with only partial coherent radiation, the observed intensity pattern changes to a convolution of a point-source with the projected source profile, with width w . If a Gaussian- shaped source is assumed for simplicity, the convolution results again in a Gaussian with the width:

$$w = S \times \frac{d}{l}, \quad (2.18)$$

hereby S and w correspond to the full width at half maximum (FWHM) of the initial and the projected source profile, respectively. For the idealized case of a point-source the visibility V , which is equivalent to the *Michelson contrast* [19], is unity, but for real sources speaking of expanded ones like e.g. in Figure 2.3 the visibility drops below unity.

¹This case is just valid assuming a perfect setup, with an infinitesimal source size, monochromatic radiation, perfect gratings with no defects and a perfect detector.

The visibility is defined as:

$$V = \frac{I_{max} - I_{min}}{I_{max} + I_{min}}, \quad (2.19)$$

where I_{max} and I_{min} denote the maximum and minimum intensity values of the fringe pattern from equation 2.17. Introducing I_{max} and I_{min} equation 2.17 results in:

$$I(x) = \frac{I_{max} + I_{min}}{2} + \frac{I_{max} - I_{min}}{2} \sin\left(\frac{2\pi x}{p_2}\right). \quad (2.20)$$

An analytical investigation of the convolution of a Gaussian with a sine, yields to an equation for the decrease of the visibility, corresponding to the projected source size w [39]:

$$V = e^{-(1.887w/p_2)^2}, \quad (2.21)$$

whereas the decrease of V has a Gaussian shape. From this equation it is possible to directly derive an inequality for the projected source size, dependent on the minimum required visibility V_0 and the periodicity p_2 of both the analyser grating G_2 and the intensity pattern, to:

$$w \leq 0.53p_2\sqrt{\ln(V_0)}. \quad (2.22)$$

As one can see in Figure 2.5 the resulting visibility is extremely dependent on the Talbot-distance d_T . As mentioned in section 2.2.2 the highest visibility, independent of dealing with monochromatic or polychromatic radiation, occurs always near the fractional Talbot-distances. For the monochromatic case it matches exact the fraction's, in the polychromatic case the maxima of the visibility are slightly shifted towards bigger distances, due to the superposition of the different Talbot-distances for each energy of the spectrum. Due to the dependence of the projected source size w on the distance between G_1 and G_2 , a fractional Talbot-distance with maximum visibility, e.g. $d = p^2/2\lambda$, can be substituted in the equation for the projected source size 2.18. With this the equation for w as a function of the Talbot-distance and -order derives to:

$$w = S \times \frac{np_2^2}{2\lambda l} = \frac{np_2^2}{2\zeta_s}, \quad (2.23)$$

where for the last step the coherence length ζ_s is substituted. With this relation the equation for the visibility, 2.21, can be rewritten as a function of the spatial coherence length, resulting in [39]:

$$V = e^{-(0.94np_2/\zeta_s)^2}, \text{ and thus again } \Rightarrow \zeta_s \geq \frac{0.94np_2}{\sqrt{\ln(V_0)}}. \quad (2.24)$$

In order to get a feeling for the behaviour of this formulas for real experiments a few numerical examples are mentioned. As one can note on the left side of Figure 2.2 the first order Talbot-distance occurs at 2,42 m, which is yet a big distance in a standard lab environment, because the dimensions of the installations have to fit into a quite small hutch due to space restrictions. For that reason higher Talbot orders $n > 1$ can

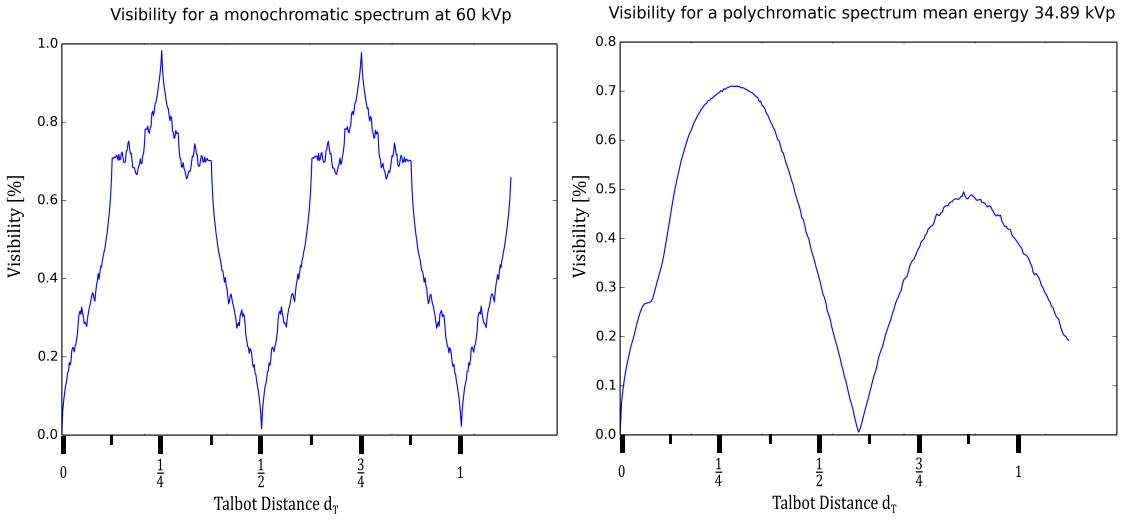


Figure 2.5: Simulated visibility as a function of the Talbot-distance d_T , corresponding to the shown Talbot-carpets in Fig. 2.2. On the left side the visibility for a monochromatic source is shown. In accordance to theory the maximum is reached at odd fractional Talbot-distances. On the right side the visibility is smeared out and no sharp peaks occur, due to the fact of the loss of the monochromaticity of the beam. Nevertheless is the loss of visibility within a small distance a bigger disadvantage for conventional X-ray sources.

be usually neglected because of space restrictions. The grating-period of the analyser grating used in general at the setup, mentioned at the beginning of this chapter, is $10\text{ }\mu\text{m}$ and assuming a required minimum visibility of $V_0 = 0.2$, the required projected source size results in $w \leq 6.7\text{ }\mu\text{m}$, according to equation 2.22. In other words the transversal coherence length defined in equation 2.24 becomes $\zeta_s \geq 7.41\text{ }\mu\text{m}$. These values are for a low required visibility quite small, yet and mostly far out of range for conventional sources, but nevertheless as mentioned above is this technique applicable inducing a source grating.

Phase stepping routine: In the next short paragraph the phase stepping-routine is explained, where the defined relations above, especially equation 2.17 and 2.19 play an important role. The reader more interested in detail see: [4, 5, 15, 22, 24]. What happens in this procedure can be explained in a few simple words: "Move one of the three gratings perpendicular to the beam direction and vertical to the grating lines, while holding the other two at fixed position, and record how the intensity pattern varies over different grating positions for each individual pixel". Again just one direction is taken into account, because in general depending on the orientation of the grating lines phase information is just acquired, if the stepping moves along the axis perpendicular to the

grating lines.² Otherwise no information is recovered as one can imagine, because the pattern will not change due to the fact, that there is no relative change between the distinct grating lines. For a more precise explanation Equation 2.17 is rewritten in a slightly different way, such that the intensity of every point x_d of the intensity pattern is expressed by:

$$I(x_d, y = 0) = a_0 + a_1 \sin(\Phi_d + \varphi), \quad \text{with } \Phi_d = \frac{2\pi}{p_2} x_d, \quad (2.25)$$

with the offset a_0 , the amplitude a_1 and the corresponding transverse shift φ of the intensity pattern [4]. This equation contains the first two terms of a Fourier series and obviously solving this equation three different positions have to be measured, because for three unknown at least three different equations are needed. So the stepping has to exceed at least three steps getting feasible information and the stepping range should cover one full period of the analyser grating G_2 . Usually an odd number of stepping points is used, because a even number of sampling-steps causes no additional benefit [4]. In order to get a good approximation of the shape of the stepping-curve, the sampling rate over one period is extended to 7 steps for in this work, but there is basically no upper limit. It is at least a trade-off between better results and measurement-time. At each of this steps an intensity image is taken, meaning that the interference pattern is sampled in each detector pixel during the particular steps. Afterwards the variation of the intensity in each pixel is then translated into a stepping-curve of the oscillating intensity describable with the equation above. To retrieve just the phase-shift if the X-rays induced by the sample, also a reference stepping without any sample at the same stepping positions is required. With these two curves at hand three different imaging signals can be extracted at once from each pixel of the dataset as illustrated in Figure 2.6 (a-c). Here the superscripts o and r denote the object and reference frame, respectively:

- As depicted in Figure 2.6 a), the transmission of the object, which in this thesis is referred to as AMP signal is:

$$a_0 = \frac{a_0^o}{a_0^r}. \quad (2.26)$$

This signal is equivalent to conventional X-ray attenuation imaging and relies also on the same physical principles.

- Figure 2.6 b), shows the relative transverse shift of the interference pattern due to the angular refraction of the X-ray beam passing through the object. With equation 2.7 for the refracted angle and a given distance d between G_1 and G_2 and the period p_2 of the intensity distribution, the transverse shift is dependent on the differential phase shift of the wave-front as:

$$\varphi = \frac{d\lambda}{p_2} \frac{\partial \Phi(x)}{\partial x}. \quad (2.27)$$

²Only the parallel orientation of the grating lines to each other and their orientation perpendicular to the beam is important. Therefore, it makes no difference for the 'phase-stepping' putting the whole interferometer in horizontal, vertical or under any other angle into the beam.

And the transverse shift of the stepping curve is given by:

$$\varphi = \varphi^o - \varphi^r \quad (2.28)$$

There is likewise an abbreviation for this imaging signal known as Differential Phase Contrast (DPC)

- Analogue to equation 2.19 the visibility of the stepping curve can be defined as $V = a_1/a_0$, thus the relative visibility of the interference pattern becomes [24]:

$$V = \frac{V^o}{V^r}. \quad (2.29)$$

The visibility in the object frame is reduced by the effect of small-angle scattering of the X-rays caused by sub-micron structures in the object, shown in Figure 2.6 c). In the following the relative visibility signal is called X-ray Dark-field Imaging (DCI).

These three properties are referred to as AMP, DPC and DCI projections throughout the remainder of this work. According to standard radiographic imaging the outcome of the different signals is a line integral over the respective quantity along the beam direction across the object, which yields two-dimensional projection images.

2.2.7 Magnification in curved wave geometry

In this small section a transition from the assumption of perfect plane waves in the latter sections, to a more real case of curved wave-fronts is described. By assuming a point like source the difference between the distance of source to object and source to detector, further denoted by SO^3 and SD , respectively, induces a magnification factor of:

$$M = \frac{SD}{SO}. \quad (2.30)$$

The geometrical considerations for this relation are shown in Figure 2.7 for the case of a grating with a period p . The image of the grating on the detector is magnified by a factor M . This magnification factor obviously also has to be taken into account, when installing the grating interferometer. Staying at the treatment of the grating as an object, the interference fringes induced by G_1 also undergo the magnification and so the period changes from p_1 to Mg_1 [4]. A way to avoid this, is producing periodic gratings which compensate this effect or one has to adjust the gratings for the exact position. Otherwise a mismatch of the exact distance between G_1 and G_2 results in Moire fringes at the detector declining the signal. For example a Moire fringe per 100 grating lines occurs for a magnification differing just one percent from 1, and with a grating period $p_1 = 5 \mu\text{m}$ it ends up with 2 Moire fringes per millimetre. Nevertheless, this factor also

³This nomenclature is chosen to be as general as possible. For the following considerations the phase grating G_1 is referred as object

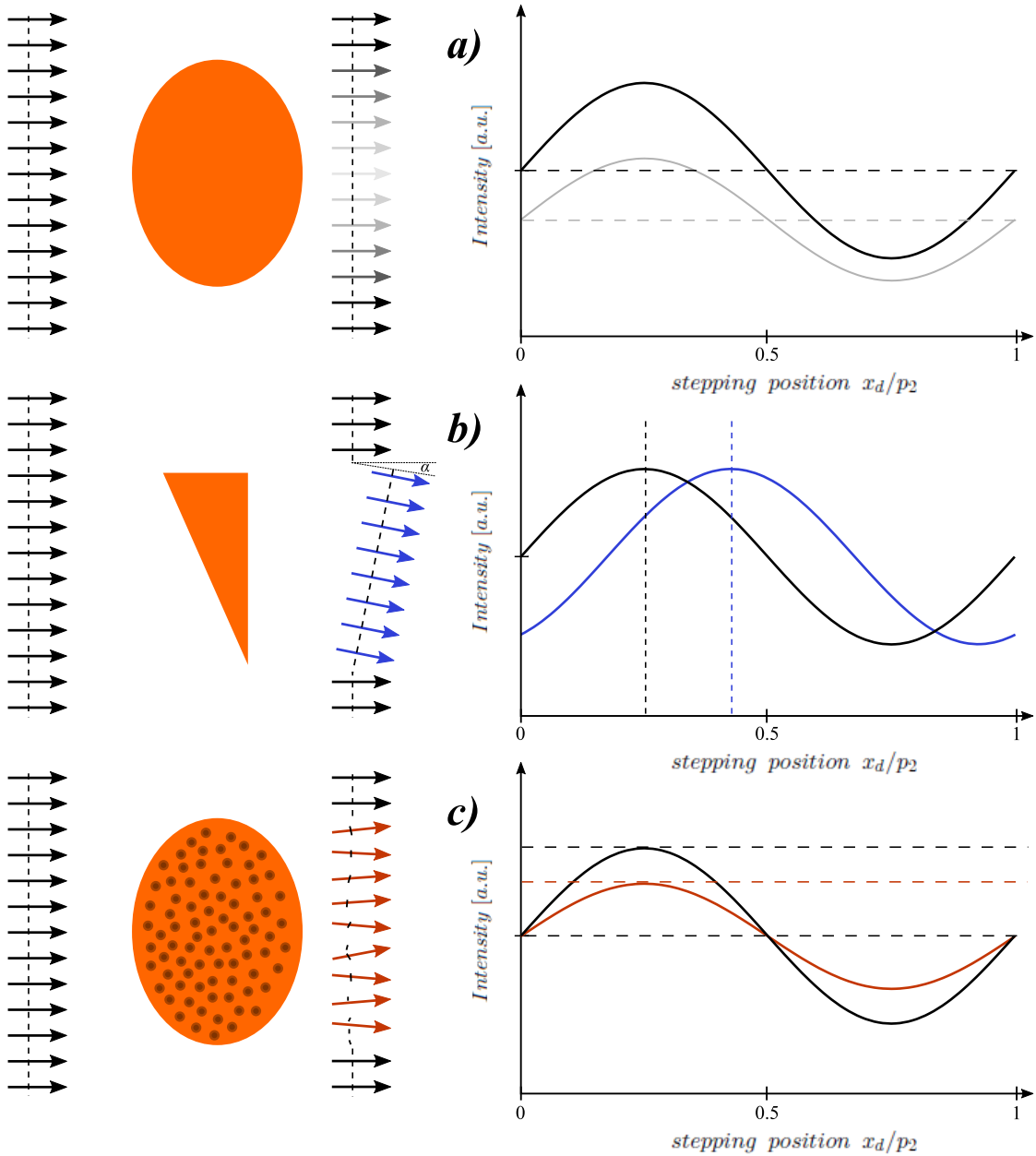


Figure 2.6: Resulting data output generated by the stepping procedure. The black solid line in the plots on the right side indicate the reference stepping curve, the coloured the curves including an object in the beam. a) the dashed lines indicate the respective mean intensity of the curve, so the decrease is proportional to the attenuation induced by the object. b) The transversal shift of the stepping curve is induced by a slightly deflection of the beam while passing through the object due to a differential phase shift of the incoming wave-front. c) due to small angle-scattering on sub-pixel features of the object the amplitude of the resulting stepping-curve is reduced.

changes the Talbot distance, thus also the fractional Talbot-distances between the two gratings. These distances given by equation 2.13 also have to be rescaled in the manner that [4]:

$$d_{T_{frac}} = M \frac{np^2}{8\lambda}. \quad (2.31)$$

So the consequence of this effect is, that the geometry of the setup has to be considered before the production of gratings, which means that the same grating might not be usable for two different installations e.g. at one hand for a short setup in a lab and at the other hand at a synchrotron beam-line with a long geometry. In the next part another effect, arising from curved wave fronts and thus magnification, is discussed with respect to a measurement technique for the spot size of the source.

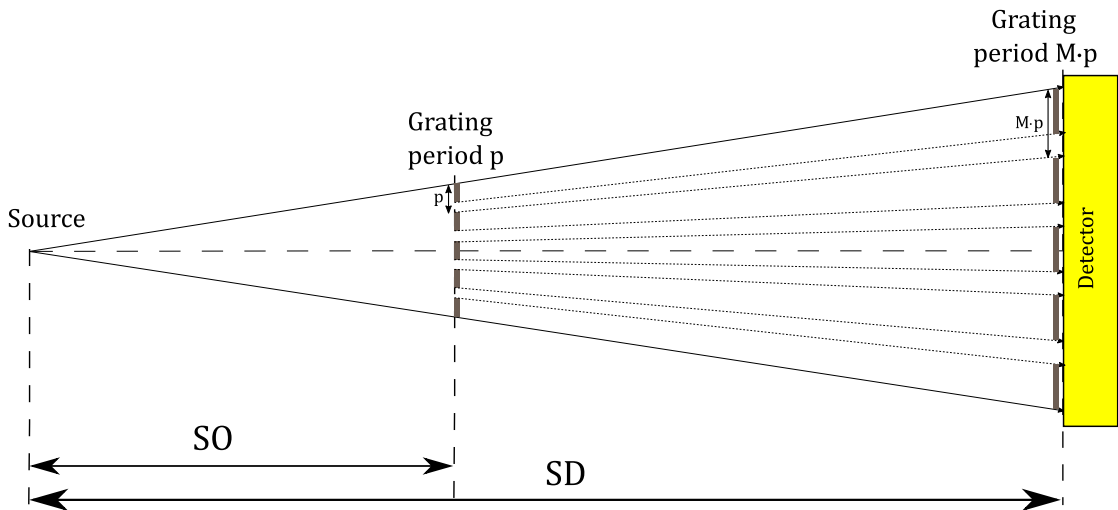


Figure 2.7: Geometric magnification in curved wave setups for a point like source. Depending on the position where the grating is placed in between source and detector the magnification factor varies form $\lim_{SO \rightarrow 0} M \rightarrow \infty$ right behind the source, to $\lim_{SO \rightarrow SD} M \rightarrow 1$ right in front of the detector.

2.2.8 Induced uncertainty by an expanded edge thickness at different magnifications

In the former section the changes for the setup properties were induced, arising by the transition from a idealized system to a more ‘realistic’ system, but there are some more changes, which have to be accounted for a real system. The approximation of a source as point source is a method to simplify the description of a system, but in reality this special case is non existent. Every source has an expanded focal-spot, which leads to complexity characterizing such a system. One example is the measurement of the extent

of the source spot, using a so called knife edge. Therefore the knife edge, speaking of a very sharp edge of a small metal cuboid, which has been polished to be as smooth as possible, is put right in the centre of the beam. The exact procedure is described in chapter 5. In the following the mismatch of this technique is considered. Thereby the focus lies one the elongation of the edge in beam direction and the influence of the distance between source and the edge. The relevant geometrical parameters for this are shown in Figure 2.8. Here $S/2$ denotes the half of the expanded source size and M_α and M_β the magnified image of the edge. These two quantities differ from each other, as a function of the thickness Δd of the cuboid and the angles α and β . Both angles are dependent on the position of the cuboid and the spot-size of the source, and they correlate in the same way like M_α and M_β . For this case the tangent of α and β is given by:

$$\left. \begin{aligned} \tan(\alpha) &= \frac{S}{2d} = \frac{M_\alpha}{l-d} \\ \tan(\beta) &= \frac{S}{2(d+\Delta d)} = \frac{M_\beta}{l-d-\Delta d} \end{aligned} \right\} \quad \frac{S}{2d} + \frac{S}{2(d+\Delta d)} = \frac{M_\alpha}{l-d} + \frac{M_\beta}{l-d-\Delta d}, \quad (2.32)$$

whereby the addition of both gives a relation between the spot size of the source and the magnified edge image resulting from the position between source and detector and the thickness of the edge. For the influence of the thickness Δd of the edge, only the equation for $\tan(\beta)$ is of interest, because just for this half of the relation the extent of the cuboid comes into play, assuming that the whole X-rays are absorbed by the cuboid.

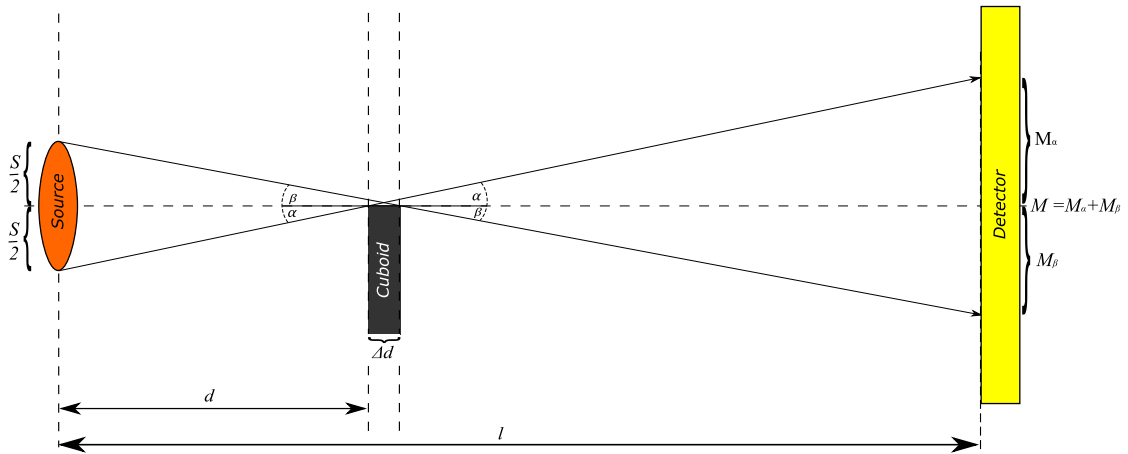


Figure 2.8: Sketch of the edge in the centre of the beam for the measurement of the source size. Due to the finite size of the edge in beam direction the upper half of the source produces a slightly smaller image of the edge on the detector-screen. This effect leads im reverse to a mismatch during the measurement of the size of the source.

Getting a feeling for the contribution of the thickness Δd , the right side of the relation from equation 2.32 for $\tan(\beta)$ is rewritten with the first two terms of the corresponding Taylor expansion around d and $x = (l - d)$, respectively, whereby the small variation is the thickness Δd . Thus $\tan(\beta)$ becomes:

$$\tan(\beta) \approx \frac{S}{2d} - \frac{S}{2d^2} \underbrace{(d - d_0)}_{\hat{=} \Delta d} \approx \frac{M_\beta}{x} - \frac{M_\beta}{x^2} \underbrace{(x - x_0)}_{\hat{=} \Delta d} \quad (2.33)$$

Replacing the term for $\tan(\beta)$ with the determined expansion on both sides of equation 2.32 yields:

$$\frac{S}{d} - \frac{S}{2d^2} \Delta d = \overbrace{\frac{M_\alpha + M_\beta}{x}}^M - \frac{M_\beta}{x^2} \Delta d, \quad (2.34)$$

As the focus lies on the induced error by the expanded thickness of the edge only the first order terms are of interest. Obviously, the thickness of the edge has to be considered only in cases of big magnifications, thus of positions very close to the source is spoken. The distances between edge and source range from about 0.09 to 0.39 m and the length of the whole setup from source to detector is $l = 1.952$ m. To get a feeling of the amount of the variations induced by an edge with a thickness of $\Delta d = 0.005$ m the values for the factors $\delta d/d^2$ and for $\Delta d/(l - d)^2$ at five different positions are determined. To have an upper and lower boundary, one position is chosen right behind the source at a distance of $d_{min} = 0.01$ m and the second 'far' away at a distance of $d_{max} = 0.5$ m. In between, the variations at the three positions for the edge measurement, $d_1 = 0.09$, $d_2 = 0.24$ and $d_3 = 0.39$ m, are determined. The results are shown in Table 2.1. As the focus lies on the induced error onto the recorded image, the second row is of high interest, because this row shows the error in the image at the detector plane. The first row is only determined for completeness and to show, that this two factors are correlated in a antithetic manner. The outcome of this approximation is, that the induced error

[1/m]	d_{min}	d_1	d_2	d_3	d_{max}
$\frac{\Delta d}{d^2}$	50	0.62	0.09	0.03	0.02
$\frac{\Delta d}{(l-d)^2}$	1.33×10^{-3}	1.44×10^{-3}	1.71×10^{-3}	2.05×10^{-3}	2.37×10^{-3}

Table 2.1: Results for the mismatch due to a finite edge thickness Δd and different magnifications. The important values are placed in the second column. These values show the influence of the thickness projected on the detector screen. Due to the fact, that these values are always of the order $\leq 10^{-3}$ the effect on the precision of the measurement can be ignored, since effects of misalignments of the edge deliver a much higher contribution [23].

yielded by the edge thickness can be neglected, because the error is always of the order of 10^{-3} regardless of the chosen distance. A more important thing is to ensure a perfect perpendicular alignment of the edge with respect to the beam direction, because slight variations induce a much bigger error onto the edge image on the detector screen [23].

2.3 Spatial system response

In this section a short introduction to linear system theory is presented, focussing on the characterization of imaging systems. For a detailed insight the reader is referred to [7, 9, 30, 37, 38]. Here, only the basic quantities for the real and radially symmetric response functions are treated, representing the experimental setup, which has to be characterized.

2.3.1 Real- and frequency-space response functions

Linear system theory is a common approach describing the properties of imaging systems. The applicability of the superposition principle on an imaging system implies it's linearity, meaning the response to a linear combination of input signals, is the same linear combination of the particular responses, called output signals. Assuming that the response of the linear system is also shift invariant, i.e. the system is linear and shift invariant (LSI), the output can be calculated by a convolution:

$$I(x, y) = S(x, y) \otimes O(x, y) = \int_{-\infty}^{\infty} \int_{-\infty}^{\infty} S(x - x', y - y') O(x', y') dx' dy', \quad (2.35)$$

$I(x, y)$ is the measured image, $S(x, y)$ is the point spread function PSF, $O(x, y)$ describes the object, and \otimes designates the two-dimensional convolution operator. Because of dealing with intensities, all functions in real space are real functions. The PSF is here defined to be normalized to unity, i.e.:

$$\int_{-\infty}^{\infty} \int_{-\infty}^{\infty} S(x, y) dx dy = 1. \quad (2.36)$$

For a full characterization of the spatial response of a system, the measurement of the PSF or the appropriate Modulation transfer function (MTF) is essential. The big advantage knowing these properties, is that they can be used correcting blur and other artefacts via deconvolution techniques. As the PSF is the response of the system to a delta-peak shaped input signal, the PSF has to be derived indirectly from objects with well known structure like edges or slits, because point sources do not exist in reality. The related MTF can be expressed using the convolution theorem, stating that the convolution of two functions in real space is just a multiplication in Fourier space. Hence equation 2.35 becomes:

$$\mathcal{F}(I(x, y)) = \mathcal{F}(S(x, y)) \cdot \mathcal{F}(O(x, y)) \Rightarrow \tilde{I}(u, v) = \tilde{S}(u, v) \cdot \tilde{O}(u, v), \quad (2.37)$$

using convolution and Fourier transform. Here the letters with tilde indicate the respective Fourier transformed function. The so called Optical transfer function (OTF) is the Fourier transform of the Point-spread-function $\tilde{S}(u, v)$ and is in general a complex function, but can be split in phase and amplitude such as:

$$\tilde{S}(u, v) = M(u, v)e^{i\Psi(u, v)}, \quad (2.38)$$

with the Phase transfer function (PTF) $\Psi(u, v)$ and the so called Modulation transfer function of the system, related in a manner that:

$$M(u, v) = \frac{|\tilde{S}(u, v)|}{\tilde{S}(0, 0)} = |\tilde{S}(u, v)|, \quad (2.39)$$

is the absolute value of the the OTF. Due to the normalization of the PSF in equation 2.36 the second identity holds, because $\tilde{S}(0, 0) = 1$. This quantity correlates also with the reduction of contrast of an sinusoidal signal comparable to part 2.2.6. In general the PSF is assumed to be radial symmetric, thus a one-dimensional description in polar coordinates is possible. Using this approach also the OTF is radial symmetric and thus real, which reduces equation 2.38 to $\tilde{S}(w) = M(w)$ (whereby this is the polar coordinate representation which is still two-dimensional!). As a consequence the system response can also be fully described by the MTF for this assumptions [9]. Now in the following sections the required mathematical expressions for the evaluation of the PSF from easy structured images⁴ is presented in a short manner.

2.3.2 Edge- and Line- spread function (ESF/LSF)

The Spatial system response (SSR) on an edge-shaped input signal is generally defined as the Edge spread function (ESF). On the other hand is the Line-spread-function (LSF) obviously the response on a line shaped signal. These functions are both two-dimensional functions, but with a constant behaviour along the direction parallel to the edge or rather line. According to this both can be expressed by a one-dimensional representation. In the further it is shown that the LSF is the first derivative of the ESF as well as the projection of the PSF. Considering that both objects are parallel to the y-axis, both functions are independent of y. Thus the Line-spread-function is defined as (using equation 2.35) [9]:

$$LSF(x) = \int_{-\infty}^{\infty} \int_{-\infty}^{\infty} S(x - x', y - y') \delta(x') dx' dy' = \int_{-\infty}^{\infty} S(x, y') dy', \quad (2.40)$$

with the Point-spread-function $S(x, y)$ defined in section 2.3.1 and the Dirac-delta function $\delta(x)$ describing the line object $O_l(x, y)$ parallel to the y-axis, which is unity integrated from $-\infty$ to ∞ . Thus the projection of the Point-spread-function in y direction is equal to the LSF (x). In contrast the edge object $O_e(x, y)$ with the same constraints

⁴Easy structured images means in this case, images that contain just one simple feature, as the projection of an edge or a slit.

can be written as:

$$O_e(x, y) = O_e(x) = \begin{cases} 0 & \text{for } x \leq 0 \\ 1 & \text{else.} \end{cases} \quad (2.41)$$

Thus the ESF is given by [9]:

$$\begin{aligned} ESF(x) &= \int_{-\infty}^{\infty} \int_{-\infty}^{\infty} S(x - x', y - y') O_e(x') dx' dy' \\ &= \int_{-\infty}^{\infty} O_e(x') \int_{-\infty}^{\infty} S(x - x', y - y') \delta(x') dy' dx' = O_e(x) * LSF(x), \end{aligned} \quad (2.42)$$

here $*$ denotes the one-dimensional convolution and $O_e(x)$ denotes the function for the edge shaped object defined above. So the derivative of the ESF appears to be:

$$\frac{d}{dx} ESF(x) = \frac{d}{dx} \{O_e(x) * LSF(x)\} = \delta(x) * LSF(x) = LSF(x). \quad (2.43)$$

This equation holds because again convolution theory states, that the derivative of a convolution of two functions can be rewritten as the convolution of the derivative of one of the two functions with the other function. In addition the derivative of the edge function results in the delta function, thus the derivative of the ESF yields the LSF.

Furthermore it is possible to generalize the above defined relation, in order that the orientation of the edges or lines can be arbitrary only with one constraint, they have to pass through the coordinate origin. With that at hand it is possible to determine the two-dimensional PSF $S(x, y)$, using tomographic reconstruction techniques for edge projections with different angles. By assuming a radial symmetric Point-spread-function the Edge spread function (ESF) is independent of the projection angle and one edge is sufficient describing the full PSF. For further reading see [9].

2.3.3 PSF of a complex system

The former section describes the evaluation for the Point-spread-function (PSF) using edge or line objects. The determination of the PSF of a whole system is a very challenging problem, because each part e.g. source or detector of an imaging system has his own two-dimensional PSF. The PSF of a simple imaging system, consisting just of source and detector, is given by convolution of the respective PSFs to:

$$PSF_{System} = PSF_{Source} \otimes PSF_{Detector} = \mathcal{F}^{-1}[\mathcal{F}(PSF_{Source}) \cdot \mathcal{F}(PSF_{Detector})]. \quad (2.44)$$

In general one has to deal with a curved wave setup as explained in 2.2.7, thus due to geometrical reasons one has to account the magnification in the latter equation, because the PSF of the source is spread out over the detector screen by this magnification factor. For convenience an one-dimensional system is assumed for the further steps. Normally for X-ray sources a Gaussian shaped PSF is assumed, whereby the width of the Gaussian

has to be multiplied by a factor $(M - 1)$. Thus equation 2.44 is rewritten with Gaussian functions for the respective parts such that:

$$A_{System} e^{-\frac{1}{2}(\frac{x-b}{\sigma_{System}})^2} = \mathcal{F}^{-1}[\mathcal{F}(A_{Source} e^{-\frac{1}{2}(\frac{x-b}{\sigma_s \cdot (M-1)})^2}) \cdot \mathcal{F}(A_{Detector} e^{-\frac{1}{2}(\frac{x-b}{\sigma_d})^2})], \quad (2.45)$$

with the amplitudes A_{System} , A_{Source} and $A_{Detector}$ and the width σ_{System} , σ_s and σ_d for the different parts, respectively. The solution of this equation is straight forward, because the Fourier transform of a Gaussian is again a Gaussian, but with reciprocal width σ and the different amplitudes cancel out, because of the normalization of the PSF in equation 2.36. With this equation at hand it is possible to determine the PSF of the source, by knowing the PSF of the detector, and thus the spot-size of the source which is in general defined as the FWHM of this function. For convenience, the PSF is in the further thesis synonym to its corresponding FWHM. For that reason some assumptions are made reaching this aim in a more easy way. Firstly the offset b is set to zero, so the peak is centred around the origin. Then both sides are multiplied by the natural logarithmic function to get rid of the exponential, so this yields to:

$$-\frac{1}{2} \left(\frac{x}{\sigma_{System}} \right)^2 = -\frac{1}{2} \left(\frac{x}{\sigma_s \cdot (M-1)} \right)^2 - \frac{1}{2} \left(\frac{x}{\sigma_d} \right)^2. \quad (2.46)$$

After canceling the pre-factors and dividing by x the equation simplifies to:

$$\left(\frac{1}{\sigma_{System}} \right)^2 = \left(\frac{1}{\sigma_{source} \cdot (M-1)} \right)^2 + \left(\frac{1}{\sigma_{detector}} \right)^2. \quad (2.47)$$

Inverting of the hole equation and taking the square-root the final equation for the system's spread width is given by:

$$\sigma_{System} = \sqrt{\sigma_{source}^2 \cdot (M-1)^2 + \sigma_{detector}^2}. \quad (2.48)$$

With this equation at hand it is now possible to determine the properties of a system at the spatial- and if needed at the frequency-domain.

3 The Setup

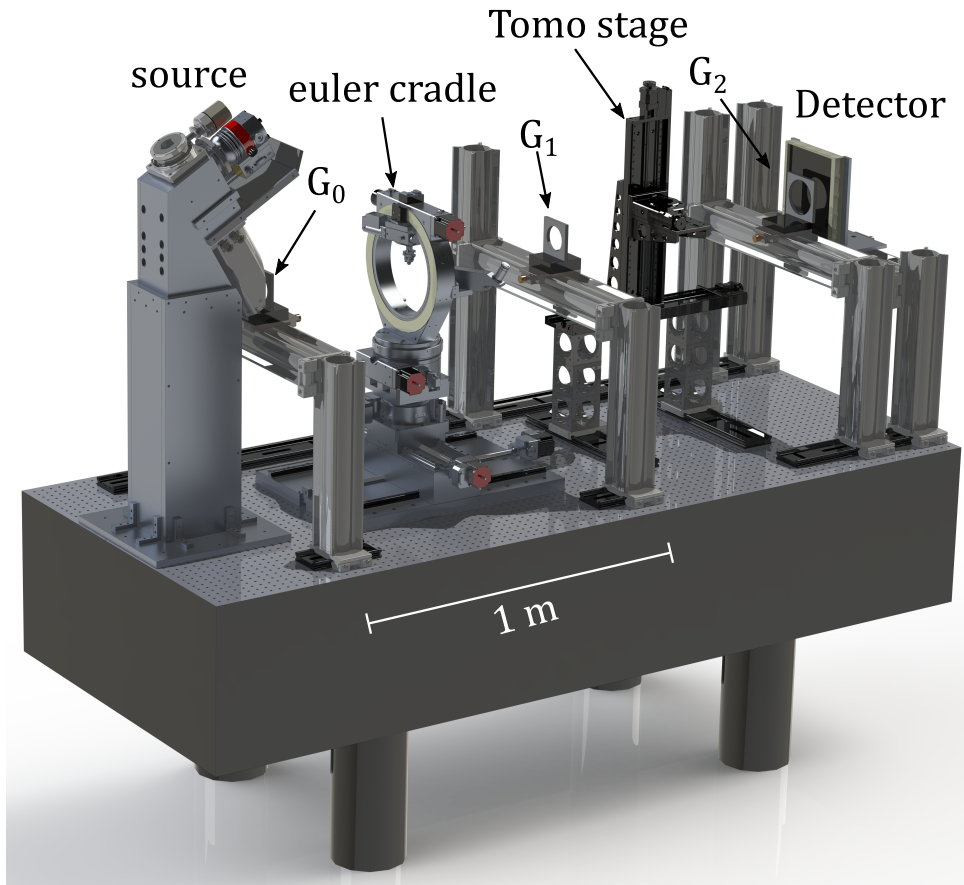


Figure 3.1: Rendering of the setup characterized in this thesis. The optical table has a size of $2.4 \text{ m} \times 1 \text{ m}$. A micro-focus tube, seen on the left, is used as source. A Varian Paxscan 2520DX X-ray detector is mounted on the other side of the table. These kind of detectors are commonly used for clinical applications. Three gratings, G_0 , G_1 , G_2 , that form a Talbot-Lau interferometer are positioned between source and detector. Samples can be mounted on two stages, either between G_0 and G_1 , or between G_1 and G_2 . Courtesy by Friedrich Prade.

In this chapter a short introduction about the individual parts of the setup and their properties is given. The setup was built up by Friedrich Prade and Florian Schaff of the biomedical physics group E17 in the TUM Physics department. The whole setup consists of three main parts: source, interferometer and detector. A general overview is depicted in Figure 3.1. A micro-focus source is placed on the left and the X-ray detector on the right side of an optical table. A Talbot-Lau interferometer consisting of three gratings is installed in between the source and the detector. The analyser grating G_2 is placed right in front of the Detector, the phase grating G_1 can be seen in the middle of the table, and right in front of the source the so called source grating G_0 is mounted. All gratings are preferably aligned perpendicular to the beam direction and with the same orientation of the grating-lines to each other. Between the gratings two different sample stages are placed, which allow for fully motorized sample positioning. In the next three sections the different parts are highlighted in a more detailed way, starting with the production of X-rays at the source, followed by the interferometer and lastly the creation of the images at the detector.

3.1 The source

The most indispensable part is of course the production of the required radiation itself. At this setup a so called ‘micro-focus’ X-ray tube designed and crafted by ‘X-RAY WorX GmbH’ is used. A micro-focus X-ray tube provides some big improvements compared to commercial X-ray sources used for clinical applications, especially with regards to achievable resolutions. The structure is in general to that of a conventional x-ray tube, but with additional parts, including an electron optic to focus the electrons generated by the cathode. For a complete overview of the properties and drawings of micro-focus tubes provided by this company see [41, 42, 43, 44].

3.1.1 Dimensions and structure

The dimension and structure of the source differs just in the additional parts from conventional sources. It consists of a heated cathode filament generating an electron beam. These electrons are then accelerated by an electric potential applied between cathode and anode. At the other end of the tube the electrons hit a tungsten reflection target, which produces the X-ray radiation. In-between these two main parts an additional part, a so called electron optic is placed. It consists of several coils which influences the trajectory of the electron beam. Four coils are responsible for the deflection of the whole beam in vertical and horizontal direction. The other coils are used for focussing the electron beam. It is in general spread over a large area, before being focussed to a very tiny area. This improves the resolution of the whole setup. A drawing of the source and the electron optic in detail is shown in Figure 3.2. Due to absorption of electrons by air the tube has to be evacuated. For that reason a vacuum pump is mounted in addition on top of the source, providing a vacuum in the order of 1.5×10^{-6} , because

in contrast to usual tubes, this micro-focus X-ray tube is a so called ‘open tube’. As in conventional sources just about 1% of the delivered power, produces X-ray radiation [13]. The remaining part heats the anode material. Thus especially for the case of a focussing source a cooling of the target is needed, to avoid the target material melting down.

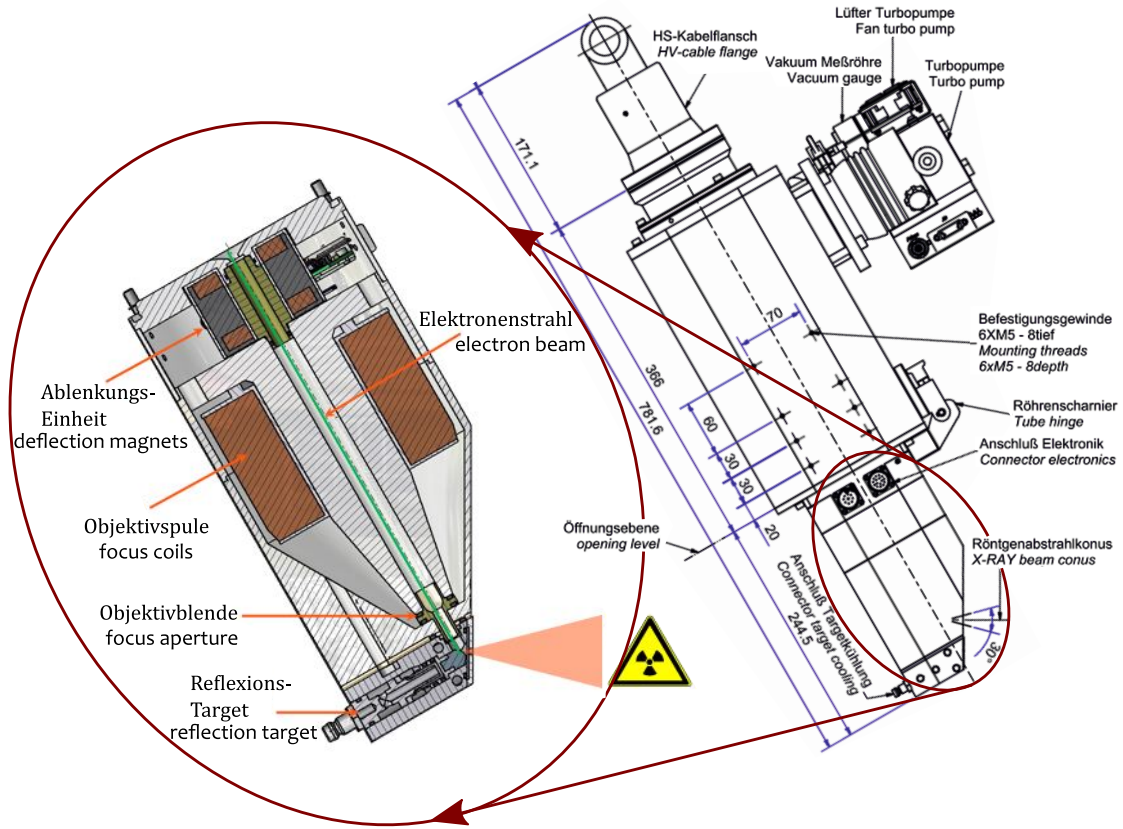


Figure 3.2: The source and its components. The length in the scheme are given in millimetre. The part highlighted in the red circle shows the focussing electron-optic, which improves the final resolution by scaling the spot size down to the micron range. The upper part of the electron optic consists of deflection coils for the vertical and horizontal direction. Subsequent to this the focussing coils are placed, which collimate the electron beam, denoted by the thin green line, to reach a small impact point at the target.

source: ©X-RAY WorX GmbH 2015 <http://www.x-ray-worx.com>

3.1.2 Properties of the source

This tube is able to work over a broad tunable range from 20 kV up to 160 kV, but due to the design energy of the Talbot-Lau interferometer it is in general operated at 60 kV. Depending on the acceleration voltage and electron current the power-output ranges from 1 W up to 300 W. The construction of the tube offers a long lifetime, because the wearing parts, filament and target, can be changed easily changed, thanks to its ‘open’ architecture (see Figure 3.2 right behind the opening level the filament holder is mounted). With the X-COM software [43] also developed and distributed by X-RAY WorX several adjustments are possible. One example for an additional feature is the possibility to manually adjust the beam in vertical and horizontal direction thanks to the linkage of the deflection magnets. This feature combined with the small focus spot allows for the transition from a mechanical stepping procedure to an electromagnetic one, in the context of Talbot interferometry. One possible advantage of this could be e.g. prevention of grating vibrations during the stepping process [10].

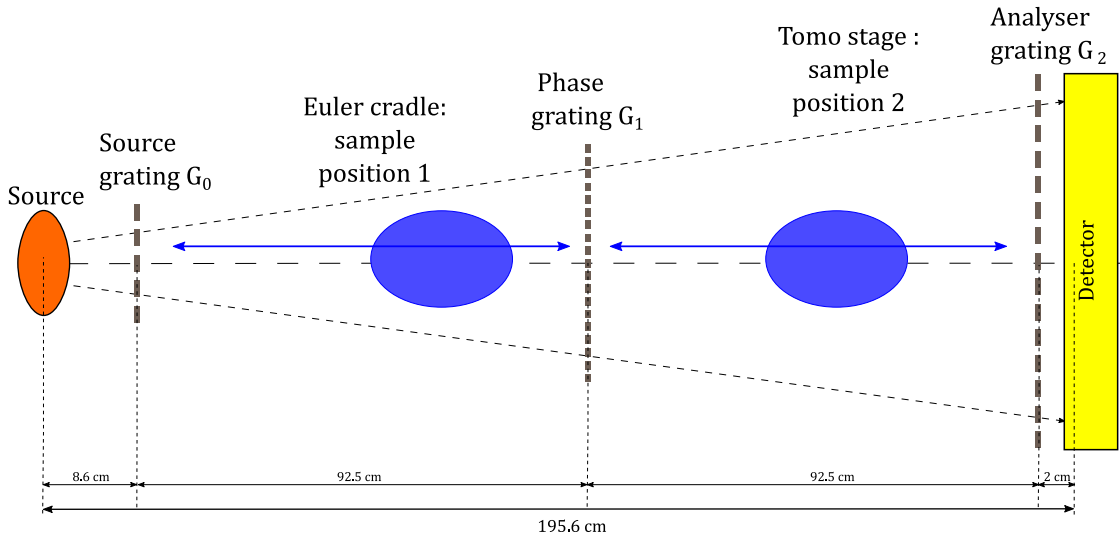


Figure 3.3: Drawing of the relative distances in-between the setup and different sample positions. This drawing shows a symmetric setting of the gratings, thus the magnification factor is 2 and the analyser grating has twice the periodicity of the $\pi/2$ phase grating. The gratings are also arranged to operate at the first fractional Talbot distance. The blue extended arrows indicate the possible positions for the sample between the gratings.

3.2 Sample handling between the gratings

As depicted in Figure 3.3, the Talbot-Lau interferometer itself occupies the main part of the setup length, starting about 8 cm behind the source, with the source grating G_0 . It is a gold absorption grating with a period of $10\ \mu\text{m}$ and a height of $150\ \mu\text{m}$. At the other side just 2 cm in front of the flat-panel detector the analyser grating G_2 with the same periodicity of $10\ \mu\text{m}$ as G_0 and a grating height of $160 - 170\ \mu\text{m}$ gold, thus also an absorption grating, is placed. Due to the high absorbency and the easy handling these two gratings are made of gold as described in 2.2.4. Accounting the magnification factor of two for a symmetric setup, the phase grating G_1 with a periodicity of $5\ \mu\text{m}$ and a nickel height of $8\ \mu\text{m}$ has to be put right in the middle between the other gratings. This leads to a distance to each grating of 92.5 cm. The gratings are not set arbitrarily to these distances, but they are put there on purpose, accounting for the first fractional Talbot distance at a design energy of 45 keV. In between the gratings two different kinds of sample holders are placed with different properties. The first one between G_0 and G_1 is an Eulerian cradle. The main advantage of this stage is that the sample can be rotated around its own axis and furthermore rotated around the beam axis as well. The second stage is a usual tomography stage which is put between G_1 and G_2 . Depending on the sample, it is put on one of these two stages. For example, if a bigger magnification is needed resolving small details within a sample the Euler cradle is recommended. On the other hand, if one is interested in the induced phase shift one has to assure to get close to the phase grating, because the sensitivity increases closer to G_1 . For this case both stages are feasible, because it makes no difference if the sample is placed in front or behind the phase grating [46].

3.3 Detector properties

The detector used for imaging is a PaxScan 2520 DX digital flat-panel detector generally used for dental and industrial cases. The detector is developed and sold by Varian medical systems and is based on amorphous silicon technology with Caesium Iodine (CsI) as conversion material on top [33]. The main advantages of this material are radiation hardness $> 1\text{Mrad}$, a broad input energy range from about $40 - 160\text{ kVp}$, good low dose performance, immunity for single photon events within the substrate and proven 3-D soft tissue capability. The total pixel area is $19.5 \times 24.4\text{ cm}$. With a pixel size of $127\ \mu\text{m}^2$ this amounts to 1536×1920 pixels. The limiting resolution is stated to be 3.94 lp/mm or in other words $253.81\ \mu\text{m}$ in vertical and horizontal direction [33]. A picture of the detector is shown in Figure 3.4. For reasons of protection a 2.5 mm thick carbon fibre plate combined with aluminium is placed in front of the active detector area. Right behind this plate the active crystal layer with $\approx 9\text{ mm}$ thickness is placed.

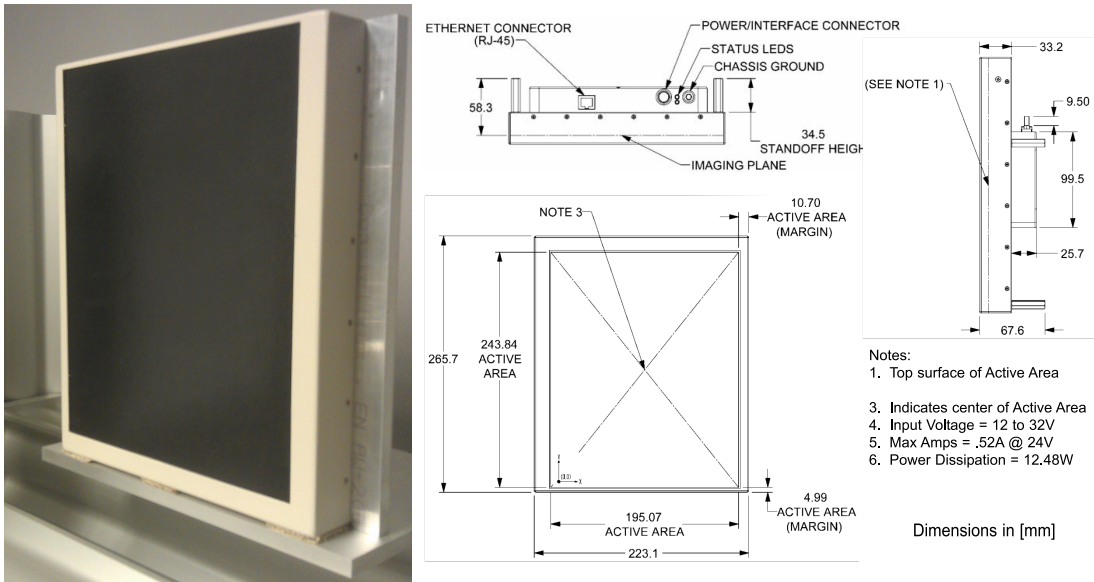


Figure 3.4: Image and properties of the PaxScan detector 2520 DX. Left hand: image of the PaxScan detector screen with the black carbon-fibre shielding in front of the active detector area. Right hand: Structure and dimensions of the detector from different perspectives. source: [33]

4 Time- and power-stability of the X-ray tube

The following chapter contains the characterization of the time- and power stability properties of the source used at this setup. For example a fluctuation in the radiation-output during a measurement can destroy the whole outcome, because a simple flat-field correction can not be used to correct for changes of the illumination during the measurement. Before the determination of the time- and power-stability the behaviour of the detector upon different exposure-times is characterized. Usually the dependency is assumed to be linear for integrating detectors. Knowing this dependency, it is possible to compare images with different exposure-time, but the same X-ray energy and input-power. For example one image is taken with 5 seconds exposure-time and the other with 10 seconds, one can compare them by simple multiplication or division of the intensity in one image with the difference time-factor of the two images, for this case also by a factor of 2. The dependency of the detector used for this thesis is shown in Figure 4.1.

On the left side the dependency of the intensity fluctuation during the exposure time is shown in a plot with linear scaled axes. For better insight onto the variations the same data are plotted as well on the right side on double logarithmic scaled axes. The behaviour on the left side as well as on the right side is almost perfectly linear, which is very positive for the further characterization. Furthermore, these plots show a first advice onto the stability of the source-output, because fluctuations within the source intensity, would destroy the linear behaviour.

4.1 Time-stability

First of all the time performance of the source is examined in a more detailed way, to have a first impression how stable the performance of the source is. This property is of big importance e.g for tomographic measurements, because such measurements are very time extensive. The main problem of a variation of the source intensity for this case is, that due to this artefacts are induced in the tomographic reconstruction. If the intensity e.g. drops down during the measurement the first projections have better statistics and are brighter, than the projections at the end. Therefore usually flat-field images are taken in between the respective projection blocks. A flat-field image is a picture without any sample, so just the pure source photon intensity-distribution is recorded. The projection images are afterwards corrected by division with these flat-

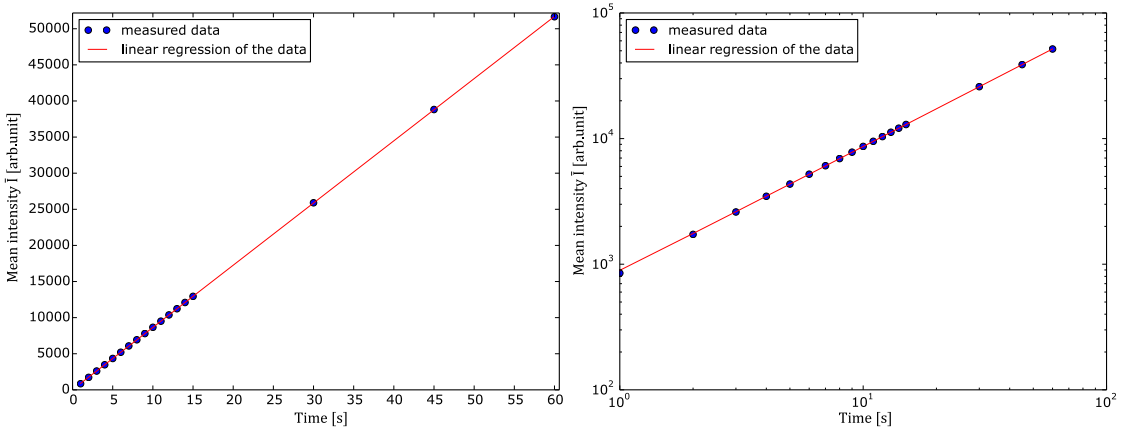


Figure 4.1: Dependency of the detector response for a steady source output intensity for different exposure times. The left plot shows the measured data points and the corresponding linear regression on linearly scaled axes. The right plot illustrates the same data and their regression, but on a double logarithmic scale. The big benefit of this plot is, that variations within the recorded intensity have much more influence on the logarithmic scale than on a linear one.

fields, to reduce the influence of possible intensity variations during the measurement. As one can imagine, the frequency taking such flat-fields is again a trade off between time effort and precision. So for the case that the time behaviour of the source is well-known one can e.g. adjust the frequency of the flat-fields, but regardless of the respective measurement technique the more stable the source the better. For the determination of the time-stability of the source, a phase tomography data-set recorded by Friedrich Prade is taken. The complete measurement time was around two days and within these two days every 20 minutes a block of stepped flat-fields is taken to correct the projection images. With the stepping routine described in 2.2.6 one can retrieve the corresponding visibility. The mean intensity is calculated by averaging of the parameter a_0 within a region of the images without any gratings, because there is no induced intensity variation by the stepping procedure. The values for these two parameters are depicted in Figure 4.2. The left side shows the mean intensity averaged over three sections of the images without gratings, and the right side shows the relative visibility of the flat-fields. The variation of the intensity varies with respect to the start value around $\approx 1\%$ which is on this time scale very low and by disregarding the spike at about 2.5 hours the variation is even lower at $\approx 0.7\%$. The relative change of the visibility during the measurement time of $\approx 4.5\%$ is a bit higher with respect to the start value of 21, 35 % but still acceptably low. A possible reason, for the higher fluctuation of the visibility compared to the mean intensity, is that the intensity is influenced by many causes, e.g. drift of the gratings thermal changes etc..

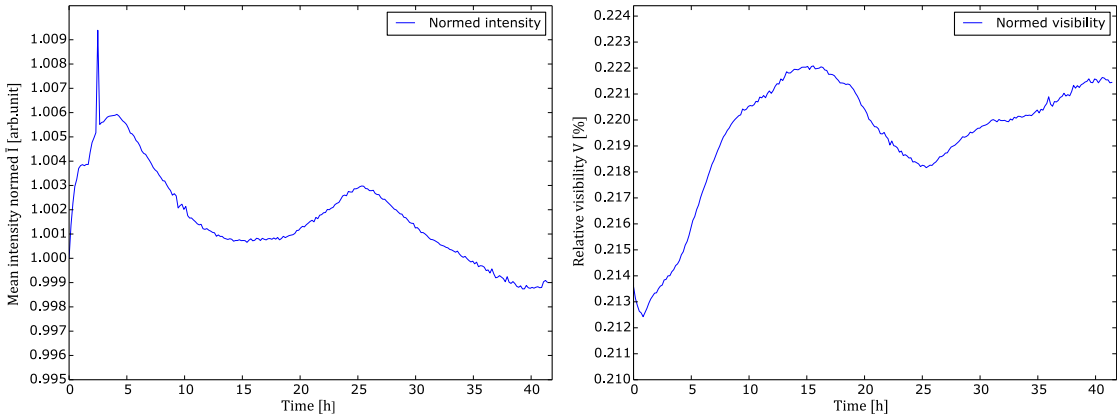


Figure 4.2: Time stability of the source for a two day measurement. The left side shows the fluctuation of the mean intensity during the measurement, the right side shows the corresponding visibility. The data points are extracted from the flat-fields taken between two projection blocks. The variation over the time is in both cases very small. The mean intensity varies by $\approx 1\%$ which is very low and also the variation of the visibility is only $\approx 4.5\%$ compared to the start value.

4.2 Power-stability

Alongside the time-stability of the source, also the power-stability is an important property, which is worth to be characterized. In this case the energy and the exposure-time is fixed to a distinct value. For this measurement the energy of the electrons was set to 60 keV and the exposure-time was for the first measurement set to 10 seconds. This measurement was repeated about eight month later, to double check the deviation from the linear behaviour between 25 – 40 W (see Figure 4.3). For the second measurement the exposure-time was set to 5 seconds. With the linear behaviour discovered in the previous section, the second data are multiplied by a factor of two for a better comparison. Tuning the power of the source by a fixed energy results in a change of the emission current of the filament. This results in more or less emitted electrons, which are able to produce X-rays. The behaviour of the function $P[W] = U \cdot I$ with a fixed U and the constant electron charge e , should result in a linear function, but the main interest of this measurement lies on the resulting intensity of the X-rays instead of directly measuring the applied current. Therefore, the plot in Figure 4.3 shows the intensity averaged over the centre of the recorded image versus the power. In each measurement, the mean intensity is measured once with the usual gratings inside the beam and once again without them. Hence, also the pure attenuation due to absorption of the grating materials is explored. As one can see the two curves with gratings lie over the whole power range always close together, whereupon the two without gratings differ more and more during the measurement. One possible explanation for this is, due to the confined lifetime of

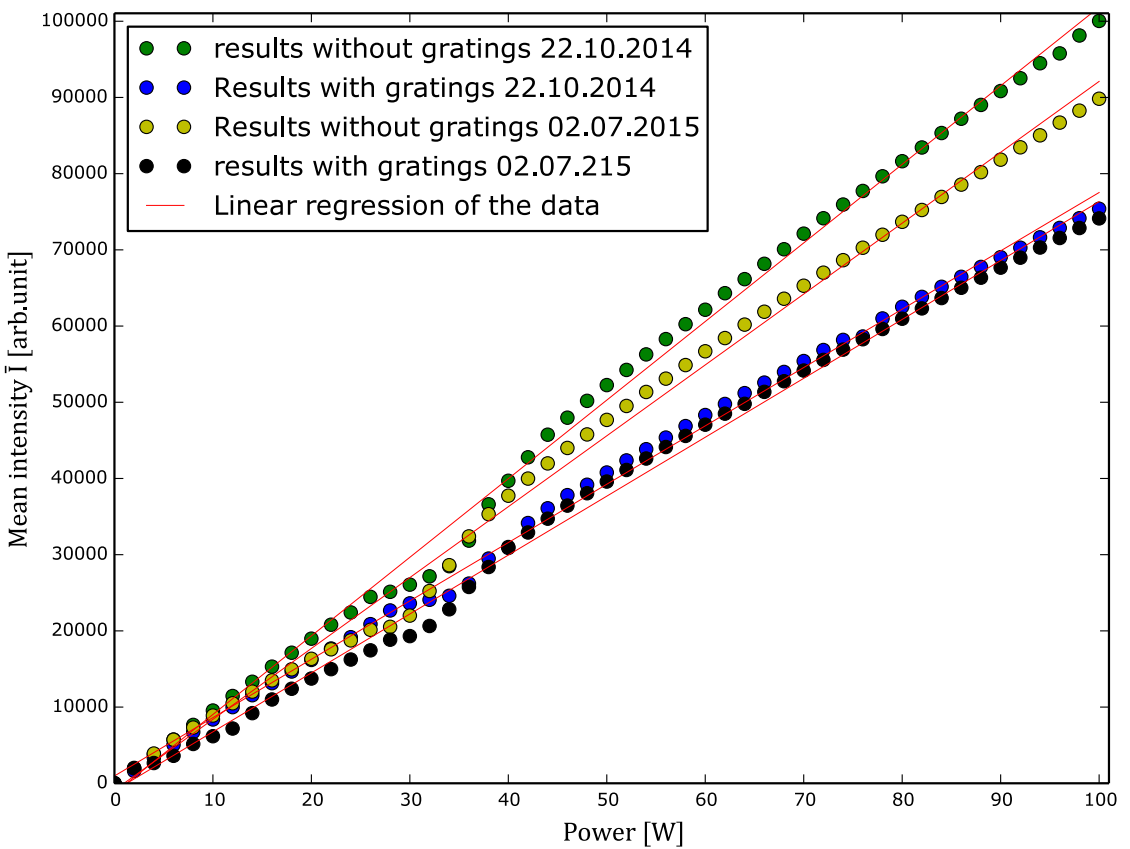


Figure 4.3: Behaviour of the power-stability of the source for a fixed energy at 60 kV. The plot shows four different data sets for two different dates. The two sets marked with blue and black dots show the source behaviour with gratings in the beam, the two with yellow and green dots without anything inside the beam.

the filament one measurement took place at the end of such a period, so there were less X-ray photons produced. Another explanation is a small change in the source spectrum, because the loss of intensity is just distinguishable in the case without gratings. This means that the spectrum for the latter measurement was possibly shifted to slightly lower photon energies, because low energy photons contribute less to the intensity than high energy photons. This is also in accordance to the curves with gratings, because photons with lower energy are almost completely absorbed in the grating material and have thus for both measurements no contribution to the intensity within the image. As one can see, the drop at 25–40 W is no measurement error, but rather an intrinsic source property. The explanation lies within the electron optic of the source. As mentioned in section 3.1.1 and shown in Figure 3.2 this optic focusses the electron beam down to a very small area. But this is just possible for a distinct power range, because otherwise

the target would be severely damaged by the deposition of too much heat on a too small area. Hence, the focus coils have to open up the beam. Unfortunately this is not happening smoothly but rather at a distinct power, for this case at 25 Watt. After this the impact area on the target increases rapidly until a distinct point.

Conclusion: In summary one can say, that the performance of the source is for both cases in time- as well in power-stability in a good position. Of course the variation in time and power is influenced by several internal and external factors, but these results give a good estimation improving the future measurements. Maybe they can even explain some artefacts in the recorded images or one can improve the image quality with this and also shorten the expenditure of time. For example in the flat-field case it is senseless to take a flat-field after one or two projections if the source is stable for a longer time period.

5 Characterization of the spatial system response

In this chapter, the general response of the system in the spatial as well as in the frequency domain is characterized, whereat special attention is paid to the determination of the spot-size of the source in different directions. It is important to know this property of an imaging system, because with this knowledge the images can be corrected afterwards e.g. for blurring due to the extent of the source size. In favour, two different techniques are presented in this chapter to obtain this property. The approach in the first part of the chapter completely relies on the spatial domain, whereupon in contrast the second technique makes a detour across the frequency domain, but of course with the Fourier transform the transition between these two spaces is very convenient. There are several methods to determine the spot size of the source e.g. with thin slits, rods or pin-holes. For a detailed overview about the different methods and corresponding norms see: [3, see: Bavendiek et. al 2012] or EN,ASTM,IEC.

5.1 Knife edge measurements

In this section the acquisition of the data and the resulting outcome for the measurements with a knife-edge is presented. At the end of the chapter a comparison between this technique and the second approach using a resolution-target, presented in 5.2, is given.

5.1.1 Data acquisition

This section focusses only on the spatial domain, because the main interest lies on the determination of the source size in different directions. The most common way to determine this property is to use a sharp edge, which is projected onto the detector screen. This projected edge-profile is also known as the ESF described in section 2.3.2. An image of such a sharp edge and their corresponding projection is shown in Figure 5.1. a) shows the projection image of the edge, which was taken at a photon energy of 60 keV, a power of 80 W and with a magnification of 24.45. The edge is on purpose tilted around an angle of about 3° with respect to the detector pixel, to achieve a sub-pixel resolution in the later data-processing algorithm. As one can clearly see, the edge is smeared out over several pixels, due to the geometrical unsharpness induced by the limited spot size. b) shows the edge which has a polished side to smooth the surface and hence improve the sharpness of the edge.

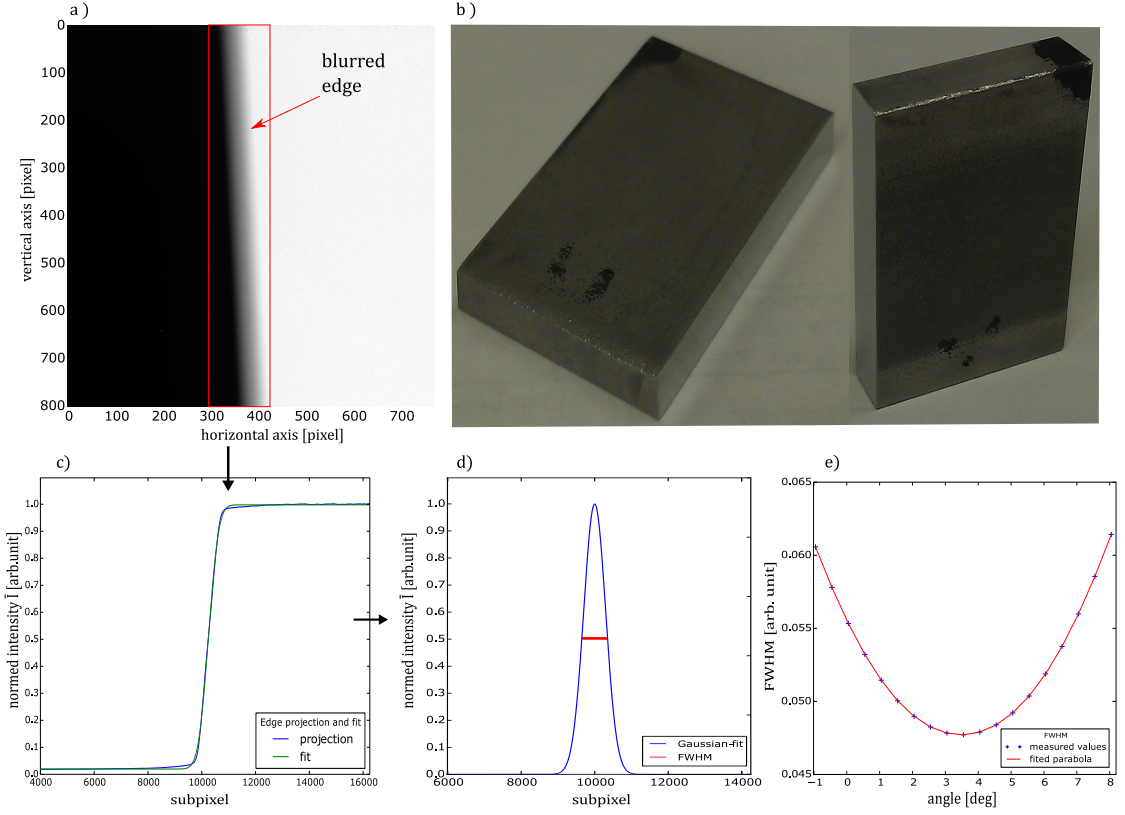


Figure 5.1: a) Image of a projected edge acquired by the Paxscan detector. The edge is slightly tilted ($\approx 3^\circ$) to provide afterwards a sub-pixel resolution at the data-processing. b) Two pictures of the cuboid with the edge profile on two opposite sides. The two thin sides of the cuboid are polished, to get a smoother surface and thus a sharper edge. c) Projection of the blurred edge projected onto the plane perpendicular to the edge direction and fit of the ESF with an error-function. d) Gaussian-fit with the acquired parameters of the error-fit. e) Illustration of the variation of the FWHM for different angles between beam-axis and the edge. The vertex of the parabola indicates the best angle aligning the edge perpendicular with respect to the beam direction.

To reinforce the contrast in the projection image, the cuboid containing the edge has a thickness of 5 mm and is made of stainless steel, because of its good absorption properties up to high photon-energies and the possibility to easily polish the surface. Usually the thickness of such edges is thinner, because the thinner the edge the less the influence of a misalignment of the edge onto the measurement. But as shown in section 2.2.8 the influence of the edge-thickness is negligible over a broad range, given that the edge is positioned perpendicular to the beam.

Edge alignment: To fulfil this condition the edge is positioned on the Euler-cradle and first aligned by hand to be perpendicular to the beam and parallel to the detector pixel. After that the centre of the beam on the detector screen is determined. This is helpful for the subsequent measurement, because the placement of the edge right in the centre of the beam yields a edge image, which stays at the same position at the detector plane, regardless of the distance to the source. At any other position, the edge will be shifted across the detector plane while changing the distance between source and edge, due to the cone-beam geometry of the source. To adjust the edge as perpendicular to the beam as possible, the edge is positioned in the centre of the beam at a distance of ≈ 70 cm. After that, the edge is rotated in small steps in both directions around its own vertical-axis, to misalign the edge on purpose. At each of these steps an image is taken, whereupon each different angle between edge and beam-axis results in a more or less broadened edge image. At angles close to 90 degrees between beam-axis and edge, the projection of the edge is less broadened than at angles far away from 90 degree. This means, there is a minimum of the broadening of the edge.

Afterwards, each projection is corrected with a flat-field. Subsequently, the projected images comparable to Figure 5.1 a), are projected onto the plane perpendicular to the edge, to improve the statistic and reduce the image noise. This procedure is comparable with a line-plot over each pixel row and a subsequent averaging over all pixel rows. This projection of the edge shows the intensity variation between the different pixels. Such a projection of the edge-profile or the corresponding ESF is shown in Figure 5.1 c). The shape of the profile reminds of a blurred step function, at which the shape can be roughly split in three parts. One part which has none intensity, because inside the cuboid the X-rays are almost completely absorbed. Another part with high intensity in each pixel, because no absorbing material is inside the beam. These two parts lead to two horizontal lines, because the neighbouring pixel have the same intensity values. Finally the third part right in between the other two parts, which is the projection of the edge itself. There, the shape of the curve is an increasing or decreasing line, with a slope correlated to the geometrical unsharpness and the misalignment of the edge. On this shape an error-function is fitted to get parameters for the comparison of the different ESFs.

Since the steepest ESF corresponds to the angle which is closest to a angle of 90° between beam-axis and edge, the slope of the fit-functions is plotted against the different angles. This results in a parabola, whereby the vertex of the parabola indicates the best perpendicular position of the edge, see Figure 5.1 d). If the edge was well aligned in the

first place the value of the best angle should be near the start value. This procedure is at first done in rough steps the start angle and afterwards with finer steps around the best value of the first measurement.

Measurement procedure: After these steps, the edge is properly aligned to start with the measurement of the system response. Therefore the edge is measured at three different distances with respect to the source. Usually one distance is sufficient for the determination of the PSF of the system and the corresponding spot size, but with three different distances the exploration of the influence of the magnification as well as the influence of the detector onto the measurement results is possible. The different distances are chosen to be close to the source plane to reduce the influence of the detector PSF and also to get a sufficient magnification of the ESF of the edge. The high magnification is necessary, because otherwise the determination neither of the ESF nor of the PSF is possible, since the pixels and the PSF of the flat-panel detector are to big. The different distances and the cuboid dimensions for the measurement are exhibited in Figure 5.2. As illustrated by the small coordinate system right in front of the detector-screen, the beam-axis is in the further set equivalent to the z-, the horizontal-axis to the x- and the vertical-axis to the y-axis, respectively.

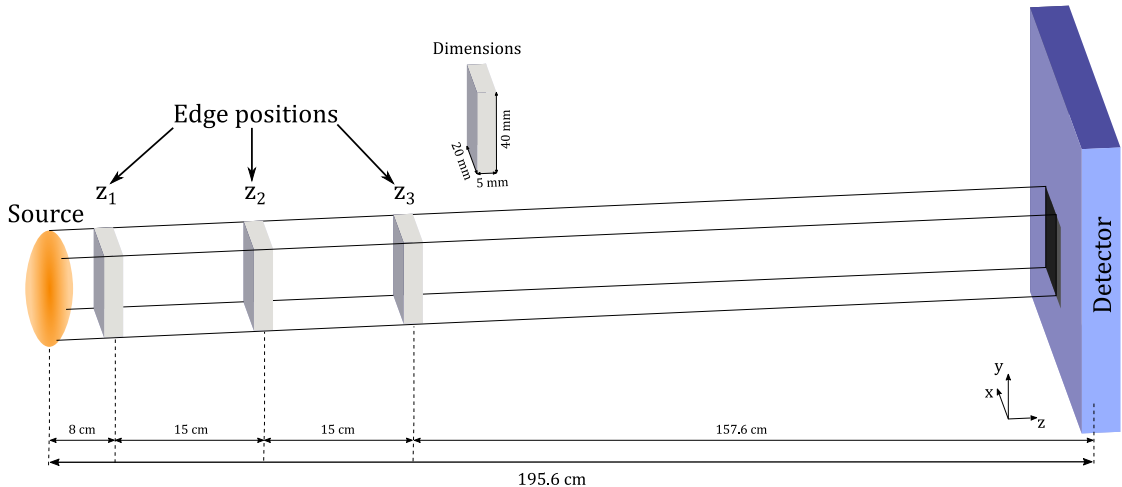


Figure 5.2: Illustration of the different edge positions during the measurement. Due to magnification the projection of the edge is spread over the detector plain perpendicular to the edge direction. The edge is placed on the Euler cradle, which is for reasons of clearness not shown here. To get an easier insight of the different arrangements a small coordinate system is placed right in front of the detector screen, thereby x- and y-axis are equivalent to the horizontal and vertical direction and the z-axis is congruent to the beam-axis of the X-ray source.

The edge is at first slightly tilted around $\approx 3^\circ$ round the z-axes (cf. Figure 5.1 a)), to provide a better resolution for the projection of the edge-profile. Due to the slight tilt, also any effects having the edge in between two neighboured pixel-lines can be avoided, as it can happen in the case of a perfectly horizontal or vertical aligned edge. At each of the particular z-positions a flat-field is taken. After the flat-field the edge is placed at each z-position in three different directions into the beam, one vertical, the second horizontal and the third at the bisecting line of the first two positions with respect to the beam-axis. With this approach it is possible to determine the shape of the spot-size and also the rotation of the source-shape in the x-y-plane at once. This measurement is done for three different energies at 40, 60 and 80 kV and at each of these energies repeated for different power-steps, to cover the whole possible power range of the respective energy. This implies e.g. for a photon energy of 60 kVp a range of 160 W, leading to over 50 measurements, whereby every measurement contains 9 projection images and three flat-fields (one for each z-position). With this images at hand, the determination of the PSF of the system is possible, but for the determination of the source size an additional measurement is needed.

To evaluate the source size, also the PSF of the Detector has to be determined. As mentioned in section 2.3.3 the results of the described measurement above are the convolution of the respective source and detector PSFs. The approach is very similar to the upper case, but much less time extensive. To determine the PSF of the detector, the same edge is placed right in front of the detector plane. With this it is made sure that the influence of the source is negligible, because the PSF of the source scales with a factor of $M - 1$ and for the position of the edge right in front of the detector the magnification is in good approximation unity. The edge is placed again in vertical as well as in horizontal direction, but due to the lack of a feasible sample holder a measurement diagonally to the pixel was not possible. But this problem can be easily solved during the processing by quadratic addition of the vertical and horizontal value to get a measure for the diagonal PSF as explained in the next section. This measurement is also repeated for the different energies, because the PSF of the detector can not necessarily be expected to be constant for different energies.

5.1.2 Data processing

For reasons of simplicity, this section just considers the processing of a data-set of one energy, in this case the one for 60 kV, because the treatment of the data-sets is the same for every energy, disregarding some changes in the projection angle or some computing parameters. To get the information out of the projected edge-profiles, the images are at first corrected with the corresponding flat-field. After that a rectangular section of about 250×250 pixel, which only contains the blurred edge, is cut out of the images to reduce computing time. This section is then projected perpendicular to the edge direction (cf. Figure 5.3), to get a ESF with a good statistic. To assure that the projection is accurately done to the plane perpendicular to the edge, the same procedure as in section

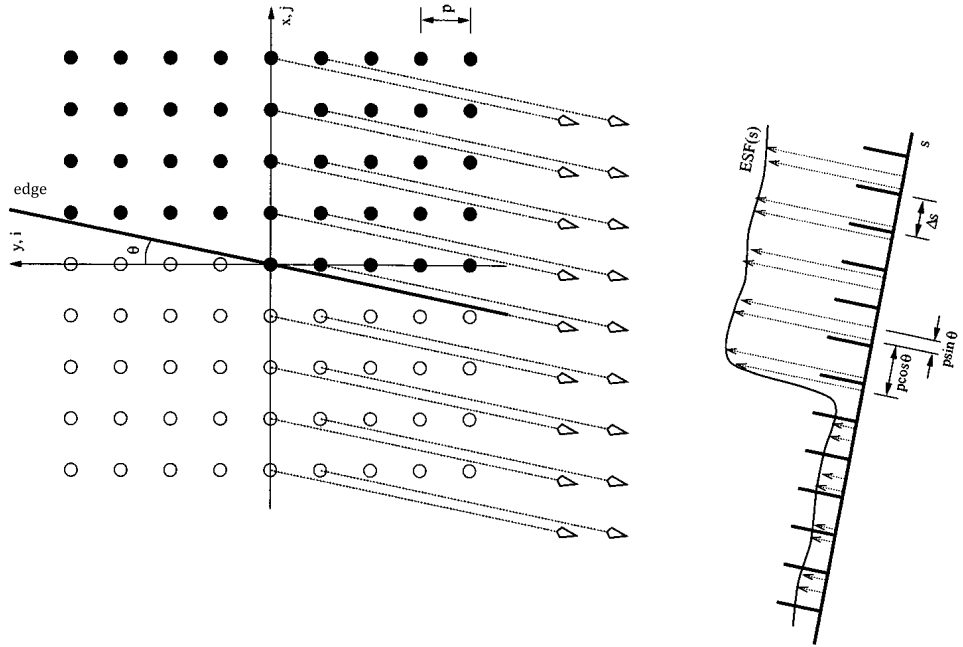


Figure 5.3: Illustration of the projection of a tilted edge onto a plane perpendicular to the edge direction. Each pixel is projected under the same angle onto the projection plane. With this technique the two dimensional edge image is reduced to a one-dimensional trace known as the ESF. Due to the tilt of the edge, every imaginable way covering a detector pixel, ranging from 0 % (no coverage) up to 100 % (full coverage), is achieved, and thus provides a sub-pixel resolution in the projection plane. adapted from [30].

5.1.1 (edge alignment) is followed, with the difference that here the projector projects the edge on purpose under a wrong projection angle, and thus onto a plane not perfectly perpendicular to the edge. Afterwards The FWHM is again minimized to find the right projection angle. For this determination one image of the whole data set with a vertical oriented edge is sufficient, because the angles for the other projection directions are correlated to each other due to the Euler cradle and can be adjusted by simply adding 90° for the horizontal case or 45° for the diagonal case, to the projector angle. For this data-set an image of a nearly vertical edge at the second measurement position (z_2) with a power of 80 Watt is chosen. With the projection angle found by this analysis, the whole data-set is projected afterwards. As mentioned above, the edge is slightly tilted from the usual coordinate axes. Using this treatment it is possible to get a sub-pixel resolution in the projected image, because the projector can split in this case each pixel by a certain number of sub-pixels and thus enhance resolution of the ESF. The splitting of one pixel in several sub-pixel is just accurately possible with a tilted edge, because every possible shadowing setting of a detector pixel occurs. In contrast to that, for an

edge aligned exactly vertical to the pixel rows only three possible shadowing settings occur, either the edge covers the whole pixel, the edge do not cover the pixel, or the edge is somewhere in the middle of the pixel.

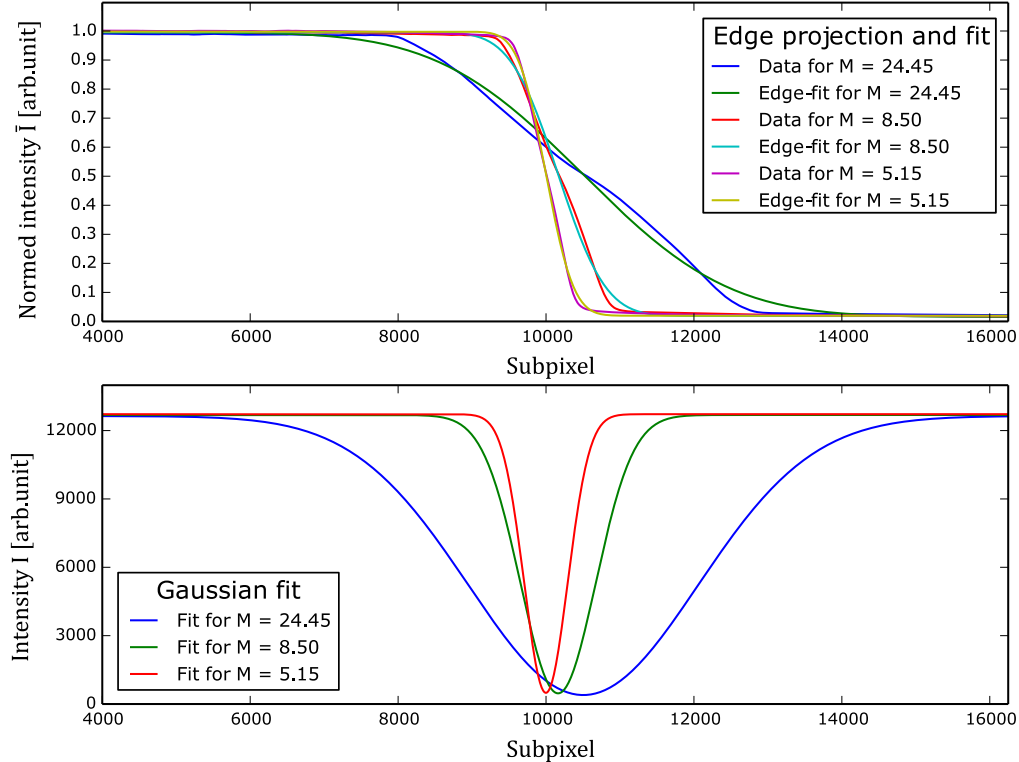


Figure 5.4: Illustration of The projected edge-profile with the associated fitted error-function, and the resulting Gaussian fits at an energy of 60 kVp and a power of 80 W. Top: Plot of three projected edges and their corresponding error-function fit for three different magnifications, respectively. To simplify the fitting, the data are normed. Bottom: Plot of the Gaussian functions fitted with the acquired fit parameter of the error-functions above, but rescaled to the determined values. The FWHM of these fits is needed to determine the spot-size of the source.

To facilitate the further steps the ESF is normed between zero and one. On this normed ESF a error-function is fitted. As shown in section 2.3.2, the LSF is the first derivative of the ESF and in this case the first derivative of an error-function results in a Gaussian-function. For that reason the parameter of the error-functions can be taken to fit the PSF of the system. To get a better imagination what happens at the particular processing steps Figure 5.4 shows some results for the error-function fit and the Gaussian fit. The plots show the results for the case of a vertical edge at an energy of 60 kVp and a

power of 80 W, for the different edge distances. The top plot shows the ESF with the corresponding fit of the error-function, and the plot below the related Gaussian fits. As one can clearly see, the influence of the magnification onto the width is tremendous, but after correction with the respective factor the tree curves should have the same width. As suggested in the latter section for the determination of the source size also the PSF of the detector is needed. The extraction of the PSF out of the raw images is the same as for the other measurements and is for that reason not explained in further detail. Only for the detector PSF in the diagonal direction and their corresponding FWHM an additional step is needed. As the adjustment of the edge diagonal to the pixel was not possible, the PSF for this direction is approximated using simple mathematical and geometrical considerations. Thereby it is assumed, that the vertical and horizontal PSF are the prime-axes of the two-dimensional detector PSF. The diagonal detector PSF is determined by quadratic multiplication of the vertical and horizontal detector PSF. With this at hand the spot-size of the source can be determined for the three directions. Therefore the equation 2.48 of section 2.3.3 is rearranged to:

$$\sigma_{source} = \frac{\sqrt{\sigma_{system}^2 - \sigma_{detector}^2}}{M - 1}, \quad (5.1)$$

and afterwards multiplied by $2\sqrt{2\ln 2}$, which finally yields the FWHM of the PSF of the source spot in one direction and for one distinct power:

$$FWHM_{source} = \frac{\sqrt{FWHM_{system}^2 - FWHM_{detector}^2}}{M - 1}, \quad (5.2)$$

whereby M denotes the different magnification factors for the different distances of the source. With this equation the determination of the spot-size in the three different directions is possible. In the next section the results for the different measurements are discussed in further detail.

5.1.3 Results and discussion

In this section the results of the various measurements at different positions are presented and discussed. The motivation of these measurements was the determination of the spot-size of the source, and thus the entire resolution of the setup. At first the measurement of the detector PSF is presented. As mentioned above, the PSF of the detector is needed to determine the PSF of the source from the convolved PSF of the system.

Detector PSF: According to the data sheet of the Varian PaxScan detector the detectors PSF is specified to $\approx 254 \mu\text{m}$. During the measurements presented above the PSF of the detector was determined twice for three different energies, 40, 60 and 80 kVp, in vertical and horizontal direction, to specify the behaviour for different energies. Furthermore the power was also varied at 60 kVp, to compare this behaviour as well to the

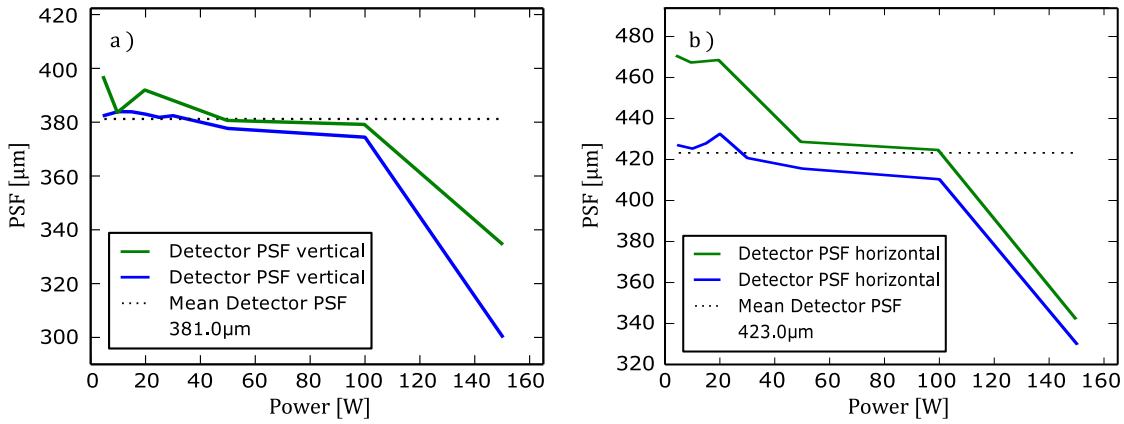


Figure 5.5: Dependency of the detector PSF for the vertical and horizontal direction. For better statistics the measurement was done twice, the first one at 09.04.2015 indicated by the green line and once again at 13.10.2015 indicated by the blue line. a) Vertical PSF of the detector for different power of the source. b) Horizontal PSF of the detector for the same power steps of the source. For reasons of clarity, only the mean PSF of the blue line is shown in both plots. Both plots show the same dependency. The PSF is in both cases up to 100 W nearly horizontal, except the green line in b). A main feature is the difference of $\approx 40 \mu\text{m}$ between the values of the horizontal and vertical PSF, which is possibly induced by the different source size in the horizontal and vertical direction. The measured values differ strongly from the denoted PSF of $\approx 254 \mu\text{m}$ by [33], except the values at 150 W.

reference value of the data sheet. The results for the measurement at 60 kVp are shown in Figure 5.5. Here, a) shows the PSFs for the vertical direction and b) the PSFs for the horizontal direction. The two different measurement are indicated by the 'blue' and 'green' colour, whereupon the "green" line shows the first measurement and the "blue" line the repetition of the same measurement about half a year later. As one can see, the behaviour for the different powers is in both plots up to a power of 100 W almost a horizontal line. The only exception is the green line in b), which also has fluctuations before 100 W. After that value the PSF drops down for all measurements. A possible explanation for this is the saturation of the detector above this value. Nevertheless, the mean detector PSF averaged over the data points of the blue lines before 100 W is in the vertical as well as in the horizontal case very close to the corresponding values. The detector PSF of the other energies was only measured at distinct power, for 40 kVp at 50 and 60 W, and at 80 kVp for both measurements at 100 W. The results of the respective measurements are presented in Table 5.1, whereby for the measurement at 60 kVp the averaged value is shown to have a better comparison between the different energies. The values for the diagonal PSF were calculated by quadratic addition of the values

direction		40 kVp	60 kVp	80 kVp
vertical PSF [μm]	October	348.6	381.3	279.2
	April	349.5	386.5	281.9
horizontal PSF [μm]	October	354.4	423.2	367.1
	April	361.7	451.8	396.4
diagonal PSF [μm]	October	351.5	402.8	326.1
	April	355.6	420.4	343.9

Table 5.1: Results of the measurements of the detector PSF for different energies and directions. There is merely a marginal difference between the values of the first and the second measurement denoted by "April" and "Ocotober" accordingly to the green and blue line in Figure 5.5, which confirms the correctness of the measurement. The difference between the vertical and horizontal direction increases constantly from 40 to 80 kVp. The values for the diagonal direction were calculated by quadratic addition of the vertical and horizontal PSF values.

of the vertical and horizontal PSFs comparable to the calculation of the diagonal of a rectangle. One main result of theses measurements is, that the horizontal PSF is always bigger compared to the vertical PSF. One possible explanation for this is the behaviour of the source, because as illustrated in the further section, the horizontal source size is always bigger than the vertical source size. This has maybe influenced the edge-profile on the detector screen and induced this difference. This explanation is also in good agreement with the presented values, because the difference of the PSFs of the different directions increases with the energy and the power, just as the source size. In the next part these results are used to determine the spot-size of the source from the measured PSF of the entire system.

Spot-size of the source: As mentioned above, the spot-size of the source is defined in this thesis as the FWHM of the PSF of the source. The FWHM can be determined with equation 5.2. For convenience, the results of the spot-size measurements are exemplary discussed on the data set for an energy of 60 kVp, because the treatment of the results for 40 and 80 kVp can be explained analogical. The results for the sizes of the source in different directions are shown in Figure 5.6, whereby a), b) and c) illustrate the vertical, horizontal and diagonal spot-size of the source, respectively. The different distances between source and edge are colour-coded in the respective plots. To discover the size of the source in the source-plane, the curves are corrected with the respective magnification factor of the different distances. Under perfect conditions, the different lines should completely coincide, but due to variations during the measurements the lines are slightly separated from each other.

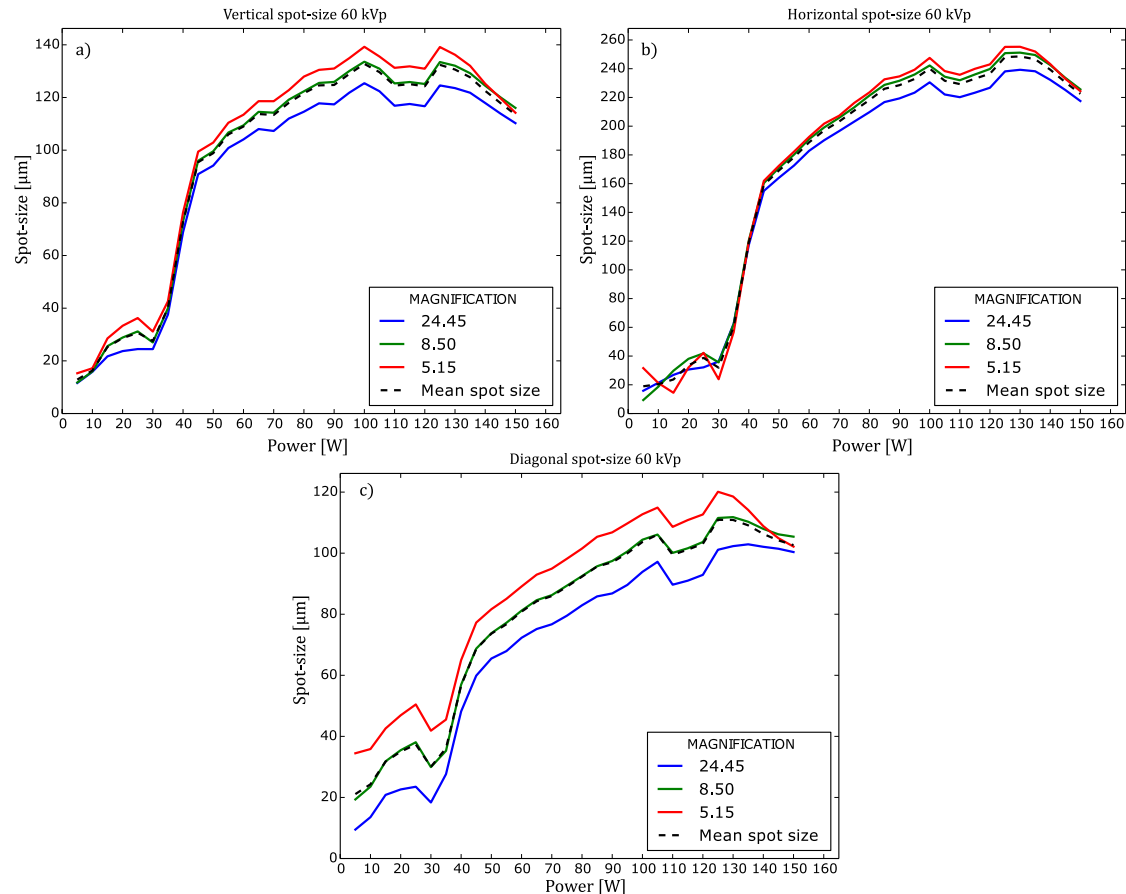


Figure 5.6: Results for the determination of the source size for different edge-directions and magnifications. a) Results for the vertical spot-size of the source. b) Results for the horizontal spot-size. c) Results for the diagonal spot-size. The different colours in the plots indicate the different magnification factors, whereby the dashed line indicates the mean value of these three different magnification. A conspicuous feature is the congruence of the mean values with the curve of the second position of the edge, here denoted as green line.

Nevertheless, the mean spot-size of the different directions fits merely perfect the result for the edge at the position z_2 see Figure 5.2. The shape of the plots is nearly for all cases the same, regardless of the edge direction, and can be separated in two parts.

The first part ranges from 0 W up to about 30 W and the second from 30 W up to the end of the measurement. However, the results below 30 W are subject to large errors, because the spot-size of the source is in this region very narrow, as further explained in section 5.2. Due to this fact, the resolution of the spot in this region is not possible with a pixel size of the detector of $127 \mu\text{m}$, because even with a magnification of 24.45, e.g. a spot-size of $5 \mu\text{m}$ lies within one pixel and is therefore not resolvable, regardless of a sub-pixel resolution in the algorithm or not.

Additionally, the intrinsic PSF of the detector itself hinders the exact determination of the spot-size, because even for bigger spot-sizes the projection of the edge is blurred due to the PSF of the detector, which leads to problems properly deconvolving the particular parts of the systems PSF. The only statement which can be delivered from this is, that the spot-size of the source is nearly constant, within the region below the defocussing point of the electron-optic at 25 W. For that reason, this region is further investigated in section 5.2. The second part can be split in two sub-regions with nearly linear behaviour, the first starts at 30 W and ends at 50 W, the second starts subsequent at 50 W up to the end of the power range. This shape is induced by the defocussing of the electron-optic avoiding a damage of the target. As mentioned earlier, the electron-optic abruptly diminishes the focussing of the electron beam at 25 W. After that the spot-size rises enormous during the next few power steps, until the optic has reach the next defined focussing point. This region can be compared to the part of a square-root function for values below unity, where the function has a very steep slope. After this the focussing of the optic decreases more constant, which yields a much slower increase of the source diameter and thus a slower increase of the spot-size itself. Nevertheless, there are two results striking the eye at first glance. The first one, the horizontal spot-size is always much bigger than the vertical spot-size (compare Figure 5.6 a) and b)). The second one, each plot shows the same intrusion at the same power values from 100 to 125 W. To explore this feature in more detail, a second measurement was done with the same parameters. The results of this measurement are shown in Figure 5.7. For better comparison, only the mean values of both measurements are shown in the plots for the different directions of the spot-size. The second measurement is denoted by the blue line. Obviously, the shape of the curve did not change, but the intrusion between 100 and 125 W disappeared and the values are bigger for all measured directions. The explanation for these variations between these two measurements are intrinsic properties of the source itself. One reason for example is the slight rotation of the source target after a certain amount of time. This is necessary, because during the operation of the source, the electrons impact always at the same position of the target. Hence, very small amounts of target material are dissipated at this position, which destroys sooner or later the small size of the spot. This process is of course very slow, comparable to the dissipation of material by a river.

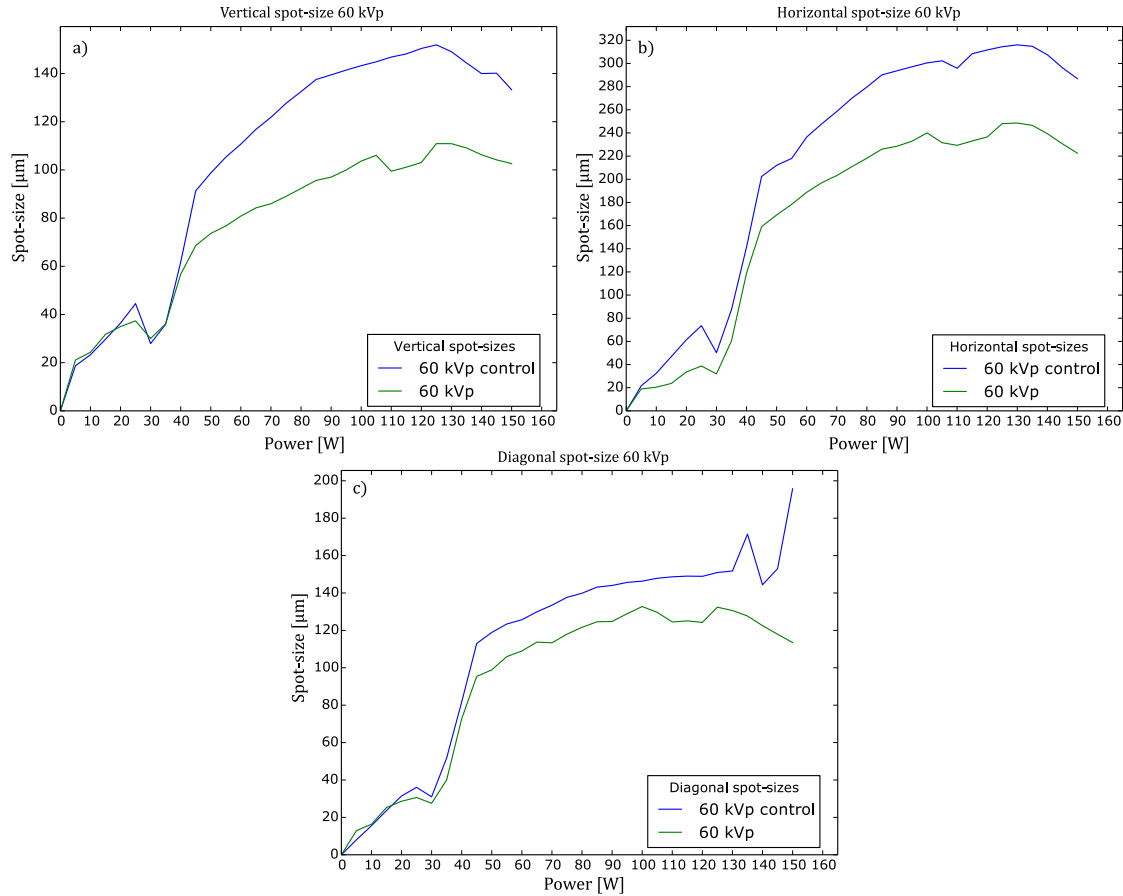


Figure 5.7: Comparison of the two measurements of the spot-size of the source at an energy of 60 kVp. The green line denotes the first measurement of the spot-size, the blue line indicates the revision measurement and is hence called 'control' measurement. a)-c) show again the spot-sizes for the different directions in the same order as in Figure 5.6. The intrusion between 100 and 125 W disappeared in the 'control' measurement and the values increased in every direction, but the general shape of the curves did not change. The changes between the two measurements are induced by the source, e.g. the filament changed of the target was rotated between the two measurements.

Therefore it is possible, that one measurement took place right before and one after the rotation of the target. Additional, the target material is not perfectly homogeneous over the whole surface and thus the interaction of the electrons within the targets surface can differ.

At the second glance, the decrease of the curves for high powers strikes the eye. This behaviour can be observed again for every measurement presented in the Figures 5.6 and 5.7, besides for the case of the 'control' measurement for the diagonal spot-size. Anyway the behaviour of this curve can not be explained properly. In contrast to this, a possible reason for the decrease of the other curves for high powers is again the saturation of the detector at high intensities, as explained for the detector PSF, which diminishes the spread of the edge over the detector screen. In general, the spot-size of the source is always in the micro-metre range, but true micro-focus properties are only reached below the defocussing point at 25 W of the electron-optic. So for a measurement which requires high resolution a power below 25 W should be chosen, because in this region a very good resolution far below $100\text{ }\mu\text{m}$ can be assured. To get a clue of the spot-size of the source for different energies, the same measurement was performed at 40 and 80 kVp. The results of theses measurements are depicted in Figure 5.8, whereby the plots a)-c) show the spot-sizes at an energy of 40 kVp and the plots d)-f) the spot-sizes at an energy of 80 kVp for the different directions, respectively. The general behaviour of the different curves is similar to the curves at 60 kVp, except for the horizontal and diagonal direction at 80 kVp. The spot-sizes decrease for this cases after a power of about 80 W and stay nearly a the same size above ≈ 120 W. This behaviour can not be completely explained, but the reason could be again the saturation of the detector, because the saturation starts at an earlier point for higher energies.

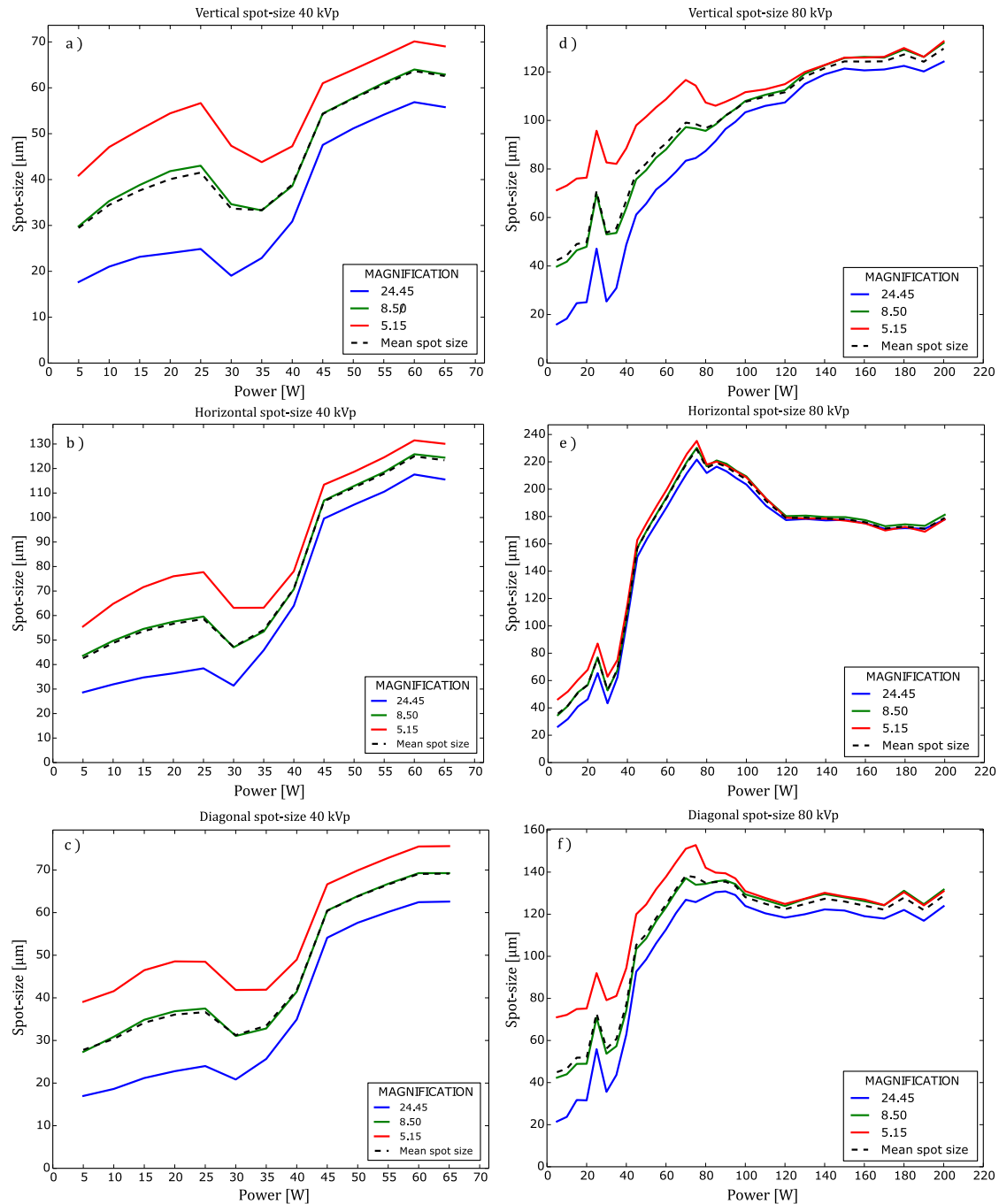


Figure 5.8: Results of the spot-size measurements for an energy of 40 and 80 kVp. a) -c) : Results for the spot-sizes in the different directions at 40 kVp. d)-f): Results for the spot-sizes in the different directions at 80 kVp.

Conclusion: In this section, the results for the various measurements of the spot-size of the source in different directions and energies, presented in the previous section, are summarized. First of all it can be stated that the general behaviour of the curves for the spot-sizes in different directions do not change much regardless of the different energies or directions. The vertical size of the spot is always much smaller than the horizontal size. This information is for example very useful, if one has to decide in which direction the gratings should be orientated because the aim is often to enhance the final resolution of the image, which is directly proportional to the size of the spot. Thus it is even reasonable using a grating interferometer to take care putting the grating lines perpendicular to the direction with the smaller spot-size, because this also enhances the resolution of the fringe-pattern. Secondly the source loses its micro-focus properties after a applied power of 25 W to prevent damage of the target. Another important result is the fact, that the size of the source strongly depends on the state of the different parts e.g. filament and target, of the source and can therefore vary for each measurement as illustrated in Figure 5.7. For that reasons a measurement of the current source size is recommended before the main measurement, if a proper deconvolution of the results of the measurement is needed. Due to problems with the too big detector pixels it was not possible to determine the spot-size quantitatively below about 25 W. Therefore as mentioned above, another approach with the aid of a resolution target is made in section 5.2.

5.1.4 Shape of the source-spot

In a next step the shape of the source spot is approximated with the results of the spot-sizes in different directions. As a first approach, an ellipse-fit is used to describe the source shape, because due to geometrical considerations of the source and thus the geometry of the electron-beam and the resulting X-ray beam produced by the e-beam hitting upon the reflection-target this shape is predicted as one can see in Figure 5.9. Usually, the determination of two directions perpendicular to each other is sufficient to determine an ellipse, because an ellipse can be determined by its two half axes. Nevertheless, an ellipse has also another degree of freedom, the rotation around the centre. Therefore, a third measurement direction is needed. Since a priori no knowledge about the shape or the rotation of the source spot was available, the measurements accounted all degrees of freedom for the assumed ellipsoidal shape of the spot. If the rotation of the ellipse around the centre is not accounted, the determination is much easier, because the two prime-axes of the ellipse have not to be determined, but are given by the half of the perpendicularly determined spot-sizes. The half of these two values can be used as so called 'big-' and 'small-' prime-axis of the ellipse.

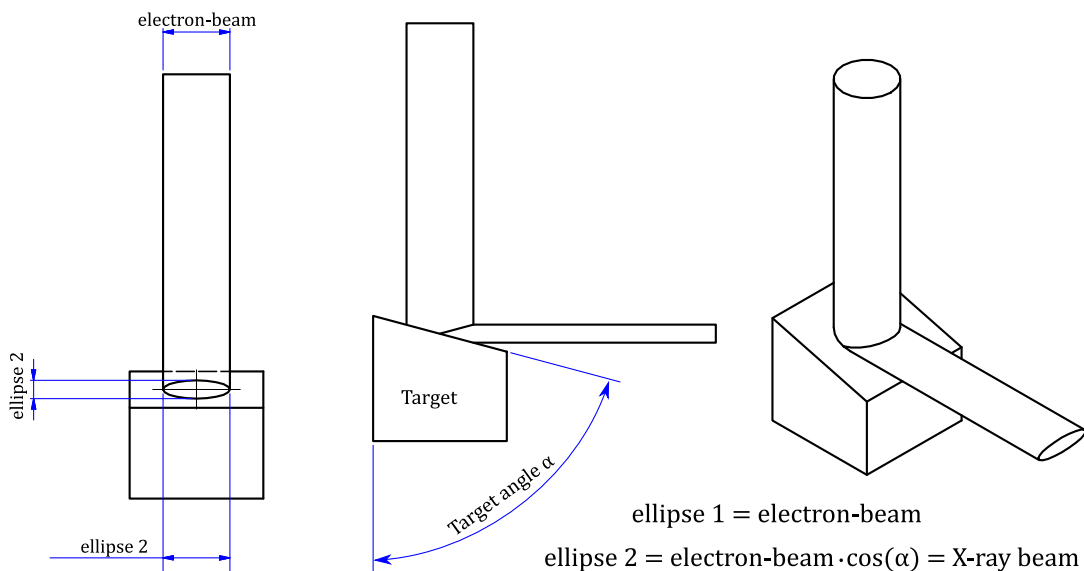


Figure 5.9: Drawing of the geometry of the electron-beam and the resulting geometry of the X-ray beam, generated by the electrons hitting upon the reflection target. The graphic shows the geometry under different angles of view. The shape of the electron beam is squeezed in vertical direction dependent on the tilt-angle of the reflection-target and thus yields an ellipse shaped X-ray beam.
adapted from: X-RAY WorkX GmbH

With this one can easily calculate the ellipse with the help of the parametric representation for the x and y direction [32]:

$$\begin{pmatrix} x(t) \\ y(t) \end{pmatrix} = \begin{pmatrix} x_0 \\ y_0 \end{pmatrix} + \begin{pmatrix} \cos(t) \cos(\phi) - \sin(t) \sin(\phi) \\ \cos(t) \sin(\phi) + \sin(t) \cos(\phi) \end{pmatrix} \cdot \begin{pmatrix} a \\ b \end{pmatrix}. \quad (5.3)$$

Here, t ranges from 0 to 2π and is the parameter to calculate the different ellipse points. a and b are the two prime-axes, x_0 and y_0 are the origin of the ellipse and ϕ is the ellipses rotation angle, which is for this simple case set to zero.

To calculate all degrees of freedom of the ellipse, the procedure is more complicated. Therefore, the measured values of the different spot-sizes have to be at first transformed into the x-y coordinate system, to be able to determine the correct prime-axes of the ellipse and their rotation angle ϕ with respect to the x-axis of the coordinate system. The transformation is again only shown for the measurements at 60 kVp as representative for all other measurements. The measured values of the spot-sizes are given in polar coordinates, at which in this representation the values for the radii are just the determined spot-sizes and the respective angles are given by the tilt of the edge.

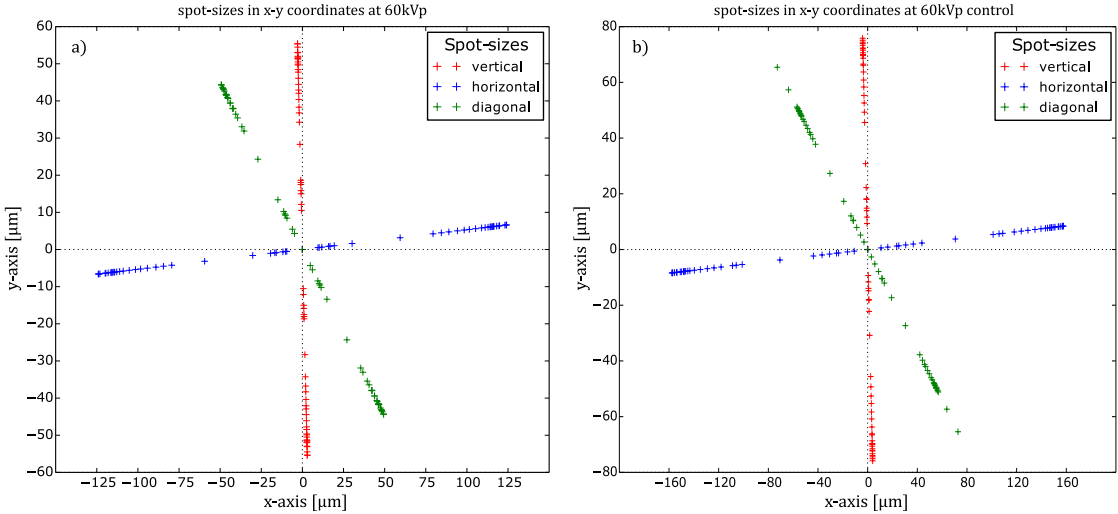


Figure 5.10: Representation of the measured spot-sizes for the different directions in in x-y coordinates. a) and b) look very similar in this representation. The reason for this is the change of the coordinate system from polar to Cartesian coordinates which doubles the data-points of each power and additionally makes the separation of the data-point of the particular powers almost impossible.

Hence they can be easily transformed into a Cartesian coordinate system. The transformed values for the different spot-sizes at a photon energy of 60 kVp are depicted in Figure 5.10. Each spot-size yields two points with contrary x-y values, because the measured size is the diameter and thus twice the radius. This provides with three different directions 6 data-points for each power. a) illustrates the transformed values for the first measurement at 60 kVp and b) the values for the second measurement. a) and b) look very similar in this representation due to the doubling of data-points caused by the transformation, why the separation of the values of the different powers is really hard.

The approximation of an ellipse onto these data is a linear minimization problem and can be solved for each respective power using a Lagrangian-multiplicator. The exact explanation of this technique can be found in [11]. After calculation of the prime-axes and the rotation angle for each power, the x and y coordinates for the particular ellipse points are determined with equation 5.3. With this, the shape of the source spot at each power step can be fitted. As the determination of the spot-size for low powers up to

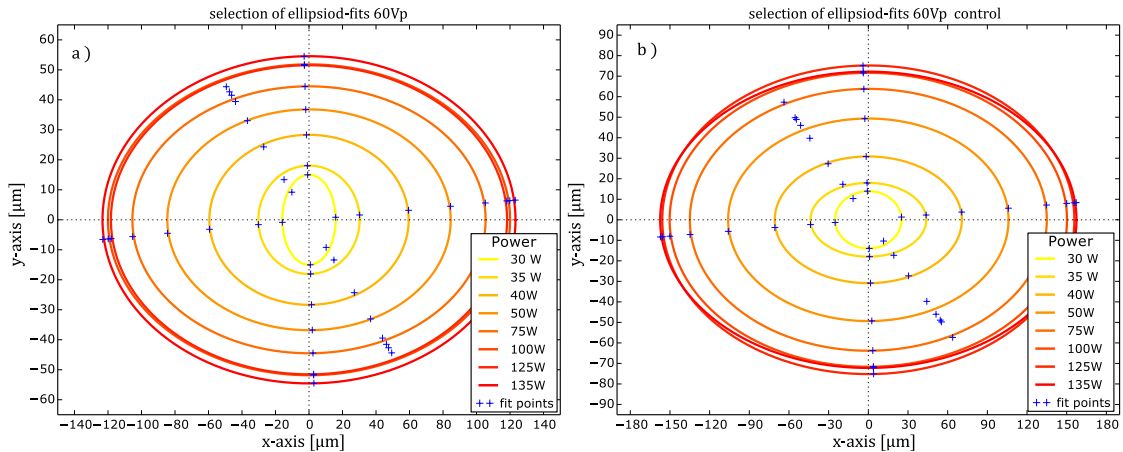


Figure 5.11: Selection of the ellipse-fits for the measurement at 60 kVp. a) shows the fits for the first measurement. b) the fits for the control measurement. The blue marker in both plots indicate the measured values of the different spot-sizes in the different directions. Both plots show the ellipse-fits for the same power-steps. The surface area of the ellipses in a) compared to b) is always smaller for the different powers and the change of the source-shape at high powers is much less in a) than in b).

25 W did not work well, these fits are not provided here. One additional problem which appeared, was the truncation of the fit-algorithm due to the values of the diagonal spot-size. Sometimes the diagonal values were too small compared to the corresponding values for the horizontal and vertical direction, which makes it impossible to fit a proper ellipse on this data subset, because to minimize the distance between the ellipse and the data

points, the curvature has to be inwardly, which obviously destroys the ellipse. Therefore, the whole data set was fitted with the simple approach of equation 5.3, disregarding the rotational degree of freedom which in addition induces big errors to the fit algorithm due to the lack sufficient fitting-points. A selection of the fitted ellipses and their originally measured spot-sizes for the different directions are illustrated in Figure 5.11. Here, a) and b) show the results for the two measurements at an energy of 60 kVp. a) and b) show the ellipses for the same power-steps. Thereby, the ellipses for the power-steps below 30 W are neglected, because as mentioned above they have no significance about the spot-size. As the spot-size increases very strongly after 30 W and slows down after 50 W, all ellipses in between this region are shown to illustrate the increase of the area of the source. For the residual power range particular ellipses are selected in bigger intervals. Both plots show a homogeneous growth of the spot-size in the different directions, whereupon the ellipses in both plots have almost the same shape, but different values. These plots remarkably indicate the change of the area of the source-spot, but the shape stays very similar between different measurements.

5.2 Resolution-target measurement

In this section another approach for the determination of the spot-size of the source is presented. Thereby, the focus especially lies on the determination of the spot size for small powers, which is not possible when using edge measurements. In this section, a resolution-target is used for the determination of the source size. Such a target is usually used to determine the resolution of various imaging systems. The principle of such a target is quite simple: Patterns of lines of a high absorbing material with different distinct thickness and distances are arranged on a substrate of low absorbing material. Thereby, the thickness of two neighbouring lines and the distance between them increases in the same manner. The determination of the PSF with this method is a bit more complicated, because the PSF can not be determined directly, rather the MTF, which has to be Fourier transformed to obtain the PSF.

5.2.1 Data acquisition

In contrast to the last section, the system response in this approach is firstly determined in the frequency domain, because with a resolution-target one is primarily able to determine the contrast between the lines an the spaces and thus the MTF of the system. Such a target provides various types of resolution patterns. The resolution-pattern used for the measurement are parallel arranged lines in a long row with distinct distances and corresponding line-thickness, which can be seen in the outer region of the image. This pattern provides the possibility to measure the resolution starting form 32 down to $4\mu\text{m}$. To avoid the influence of the detector PSF, the target is put very close behind the source, about 1 cm. This leads to a magnification of about 195. As a side effect of this high magnification, different images of the target for one power have to be taken,

because only a small part of the whole target is illuminated per image. Due to difficulties of the target alignment of the diagonal direction for the different images, this approach focusses on the vertical and horizontal direction.

The measurement procedure is analogue to the one described in the previous section, but has slight differences. One difference is, the lines of the target are aligned vertically and horizontally to the detector pixels without any tilt. Nevertheless, a small tilt can not be avoided, but the angle is very small $\approx 0.005^\circ$, which is approximated by the ratio of the shift of pixels in x-direction of the straight border line of the resolution pattern over all pixels in y-direction. For that reason it can be assumed that the tilt of the resolution pattern has no influence on the later data processing. As for the edge measurement, a flat-field is taken for each power and for each target-direction. After the flat-field image, the target is at first moved along the vertical-axis. Thereby, nine pictures are taken to cover the whole resolution target. Afterwards, this procedure is repeated for the horizontally orientated target.

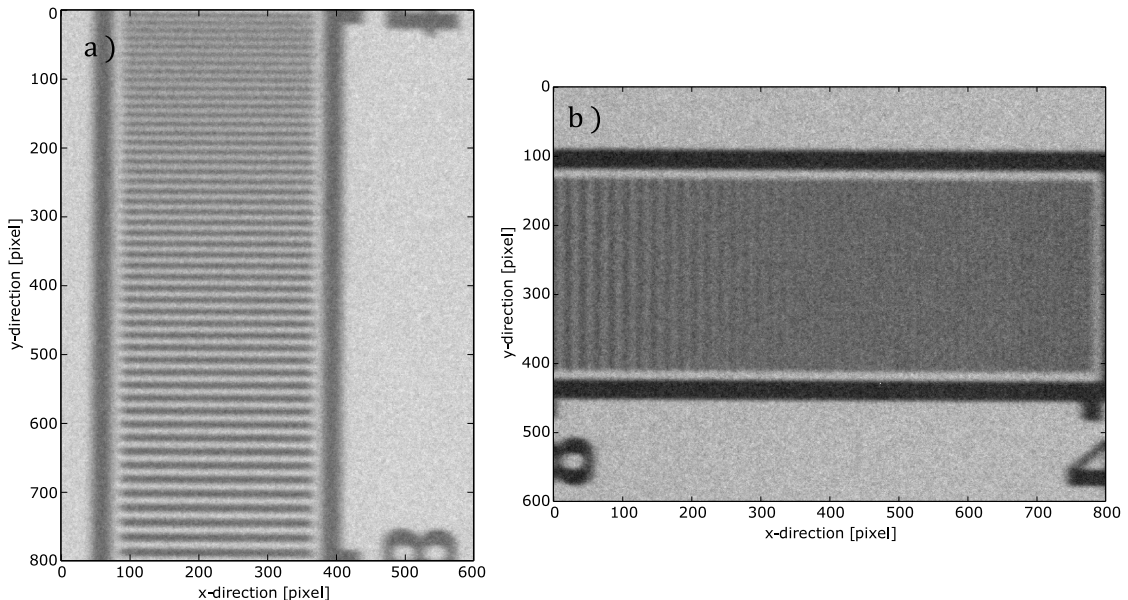


Figure 5.12: First images of the image-series for the vertical and horizontal direction at an energy of 60 kVp and 3 W. Both images are flat-field corrected and show the region between 4 and 8 μm . a) clipping of the beginning of the resolution-target in vertical direction. b) section of the beginning of the resolution target in horizontal direction. Comparison of a) and b) yields that the resolution in a) is much better than in b), because the 4 μm lines in a) can be separated from each other in contrast to b).

This measurement procedure is again repeated for the same energies as in the previous section. At each of these energies, the power is once again varied in small power-steps starting at 3 up to 40 W to have the possibility to compare the measured spot-sizes with the corresponding values, obtained in the previous section. In contrast to the knife-edge measurement the position of the target between source and detector is not varied. To get a feeling how the particular images look like, Figure 5.12 a) shows the first image of the series for the vertical direction and b) the first image of the series for the horizontal direction, at an energy of 60 kVp and a power of 3 W.

5.2.2 Data processing

As mentioned before, at least nine pictures are needed to cover the whole resolution target for one power, due to the large magnification. Therefore, the particular images have to be stitched together to obtain at once an image of the whole target. For that reason, each image is at first corrected with the respective flat-field. Afterwards, the overlap between the particular images is determined, whereat the overlap is always the same between the different pictures, because the images were taken at equidistant steps, which simplifies the whole process. Due to this, the overlap has to be determined just once for the vertical and once for the horizontal direction. Subsequent, the overlapping pixels of two neighboured images are cut off and averaged, whereby this procedure is repeated for the remaining images. Then, the particular images and the related overlap between them are stitched together to a complete image of the resolution target one in vertical and the other in the horizontal direction. This procedure is then repeated for all power steps. Some results of the stitching algorithm are depicted in Figure 5.13. a), c) and e) show the vertical resolution-target for a power of 3, 25 and 30 W, respectively. b), d) and f) show the same target for the horizontal direction for the same power-steps rotated around 90 degree to simplify the comparison between the particular images. Before the line-pattern can be projected onto the plane perpendicular to the lines, in the same manner as presented in the previous section, the obtained images are cropped so that they only contain the significant target lines and nothing additional. This results in alternating high and low values, whereupon high values arise at the pixels without any absorbing material and low values at the pixels covered by the target lines. Therefore, the negative logarithm of these values is taken to invert the values and thus obtain later the contrast in the right way.

To get a clue how the projection of the resolution-targets look like the projected values are shown in Figure 5.14 for two different energies and both directions. In this Figure a) and b) show the projected values for the vertical and horizontal direction at a power of 3 W and c) and d) the same resolution-target at a power of 30 W and an energy of 60 kVp, respectively. Thereby, the thickness of the target-lines and the particular spaces in between shrink from the left to the right, from 32 down to 4 μm , which leads to a decrease of the amplitude between the individual values especially in the region close to the end of the resolution range.

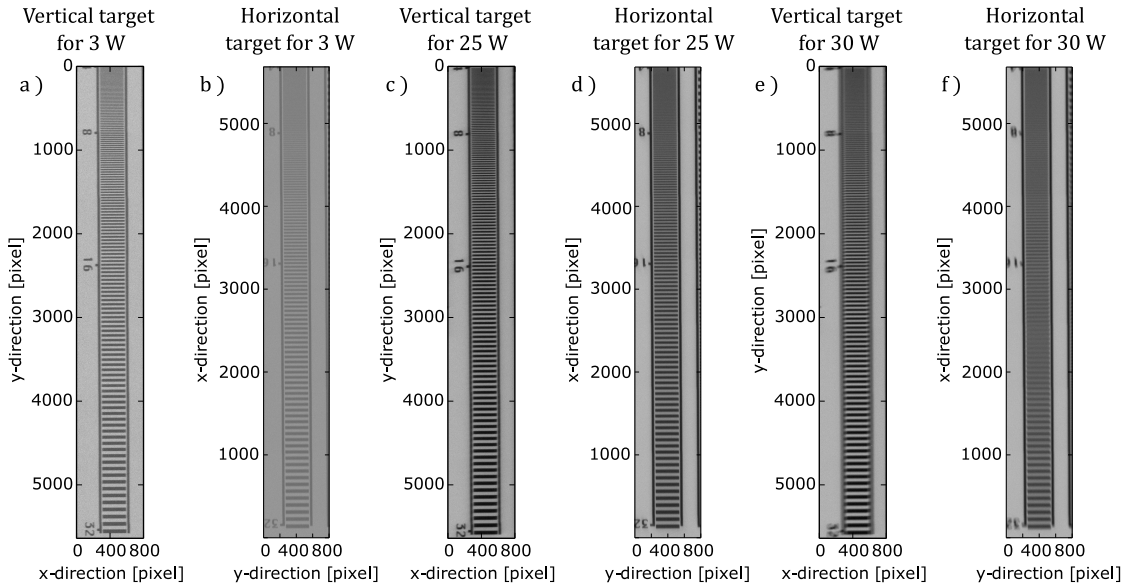


Figure 5.13: Images of the resolution-targets for different power at an energy of 60 kVp. From the left to the right the power of the source increases. a),c),e) show the resolution target in vertical direction for different power. b),d),f) show the resolution-target in horizontal direction for different power. The resolution of the vertical direction compared to the horizontal direction is better for every power. This confirms the results from section 5.1.

In general the following rule applies: The earlier the amplitude decreases the worse is the resolution. To evaluate the contrast with these projected data another intermediate step is necessary. At this approach, the contrast between the lines and spaces is determined with the same formula as used for definition of the visibility in equation 2.19. Hence, all local maxima and minima, meaning the maximum and minimum intensity-values of the particular lines and spaces, have to be extracted from these curves to obtain the so called Michelson-contrast. A main problem arises during the extraction-algorithm, due to the fact that the lines getting thinner and thinner and likewise the distance between the particular lines shrink. This fact makes it difficult to distinguish the individual maxima and minima and for higher power it gets impossible to obtain reasonable data. Therefore, the contrast between the different lines of the resolution-pattern was only determined up to a power of 30 W. As mentioned earlier, at higher power also the spot increases to much and hence each measurement in one particular direction is strongly influenced by the spot-size perpendicular to this direction. After the determination of the contrast of all lines of the resolution-pattern, the obtained values are normed to the maximum contrast, which arises at the largest line-thickness, meaning in this case 32 μm or expressed with spatial frequency at 31 lp/mm.

This scaling is necessary, because the MTF which is equivalent to the determined Michelson-contrast is in general stated in percent. As the MTF is a property in the frequency domain, the spatial resolution denoted at the target is converted to the equivalent spatial frequencies.

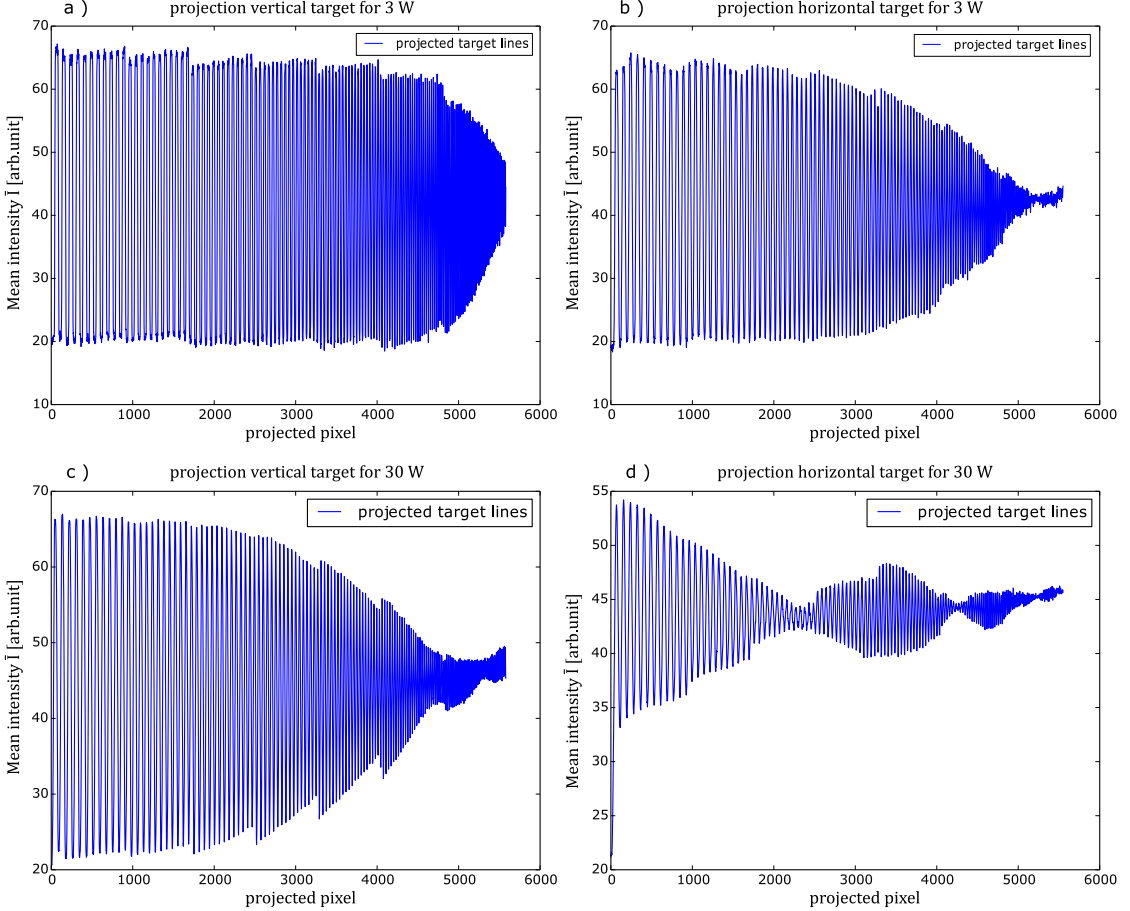


Figure 5.14: Illustration of the projected resolution-pattern at an energy of 60 kVp. a) and b): Projection of the vertical and horizontal resolution-pattern at 3 W. c) and d): Projection of the same pattern for the vertical and horizontal direction for 30 W. The sharp jumps between the particular local minima are artefacts of the stitching algorithm. As a rule of thumb holds: The earlier the amplitude decreases between the particular values the worse the resolution.

Usually the next step would be the Fourier transformation of the obtained MTFs, which leads to the PSF of the source in the different directions and thus the spot-size, which can be compared with the obtained spot-sizes in the previous section. Unfortunately, an easy Fourier transform was not possible, because the most obtained MTFs did not drop down to zero before the maximum spatial frequency, which can be resolved with the resolution-target. Therefore, it is not trivial to find a feasible fit-function. Even with a good initial guess of the fit-function, there are big errors induced during this step, which destroys the significance of the obtained values. To get a good transform a fit of the particular MTFs is needed. Nevertheless, there are several results and statements, which can be retrieved from the obtained curves of the MTFs for the different directions and powers.

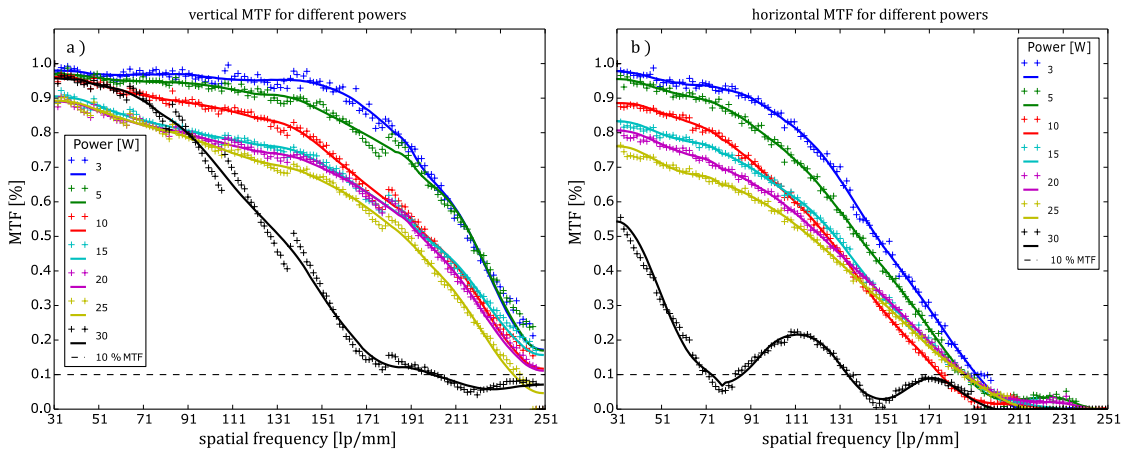


Figure 5.15: Resulting MTF's of the resolution-target measurement at an energy of 60 kVp and different power. a) determined contrast values and associated smoothed MTF curves for the vertical target. b) determined contrast values and associated smoothed MTF curves for the horizontal target. The resolution drops down for increasing power, but in the vertical case the MTFs never drop down below 10 % which is usually set to be the resolution-limit, besides for 25 and 30 W, which is induced by the influence of the horizontal spot-size.

5.2.3 Results and discussion

In this section the outcome of the previous measurements is discussed. The results of the determination of the MTF in the previous part are illustrated in Figure 5.15. Here, a) shows the obtained MTFs for the vertical direction and different power at an energy of 60 kVp and b) the MTFs for the horizontal direction. Both plots show the obtained values at each spatial frequency and the corresponding smoothed curve. The dashed line at 10 % indicates in both plots the resolution limit. If the values of the MTF drop down

below this value the resolution of higher spatial frequencies is not possible any more. The observed behaviour of the curves is in good agreement with the previous results. The MTFs of the horizontal direction drop down much faster than the MTFs of the vertical direction, which means that the resolution in horizontal direction is much worse than in vertical direction and thus implies, that the spot-size in horizontal direction is again much bigger than the spot-size of the vertical direction. As one can see in a), the resolution limit in vertical direction is never reached for a source power smaller than 25 W, which denotes that the spot-size in this direction is smaller than $4\text{ }\mu\text{m}$, because also the finest lines of the resolution-target can be distinguished.

This is in good agreement with the first sighting of the observations made in Figure 5.12 a), at which the 4 micron lines can still be visually distinguished, and also with the predicted source size of $2\text{ }\mu\text{m}$ by the data-sheet of the source cf. [42]. To get a feeling about the limited resolution of the different curves, the intersection points of the MTFs with the 10 % limit are depicted in Table 5.2, whereupon the different values are expressed in units of Spatial frequency (Sf) for the frequency-domain and also converted in μm for the spatial domain, which is referred to as PSF of the source. For the MTFs

Power [W]		3	5	10	15	20	25	30
vertical resolution	Sf [lp/mm]	> 250	> 250	> 250	> 250	> 250	235	200
	spot-size [μm]	< 4	< 4	< 4	< 4	< 4	4.3	5
horizontal resolution	Sf [lp/mm]	192	187	175	187	189	187	73
	spot-size [μm]	5.2	5.3	5.7	5.3	5.3	5.3	13.6

Table 5.2: Resolution limits of the different MTFs obtained from the resolution-targets in vertical and horizontal direction and at different power. The assumed spot-sizes are registered below, whereupon these values are not the FWHM of the Fourier transform of the MTFs but the converted spatial frequencies to have an approximative value.

which do not intersect with the resolution limit the best resolution of 250 lp/mm for the frequency-domain, or $4\text{ }\mu\text{m}$ for the spatial-domain is assumed, respectively. Hence, for a proper determination of the resolution limit which is directly proportional to the size of the source, another resolution-target with smaller features is required, because with this target it only can be stated that the spot-size has to be, at least in vertical direction, smaller than $4\text{ }\mu\text{m}$. In order to quantitatively determine the spot-size with this method, the different MTFs usually have to be Fourier transformed to obtain the related PSF and thus get quantitative values in analogue to the previous section. This transformation was left out due to several reasons. One reason is, the resolution-target only covers a small part of spatial-frequencies. Therefore, the transformation is affected by big errors, which would anyway destroy the validity of the obtained values. Thereby, one

source of error is the lack of measurement points at higher spatial frequencies at which their values would drop down zero, which hinders a proper fit of the data and thus a good transformation. Another problem is after the transformation the gap ranging from the origin up to $4\mu\text{m}$, because the transformed function only covers the range between $4\mu\text{m}$ up to $32\mu\text{m}$. Hence, an additional fit onto the retrieved part of the PSF has to be done which again induces some error. In addition to this problems, the obtained data of the vertical measurements are influenced by the horizontal extent of the source spot. As mentioned above, the horizontal spot-size lutes the enclosure-lines perpendicularly to the line-pattern into the line-pattern itself, and thus falsifies the contrast values above a power of 25 W. This can also be confirmed by sighting of the stitched images in Figure 5.13. The comparison among themselves yields three main results. First of all, the resolution in vertical direction is again always better than in the corresponding horizontal direction, which means that the spot-size in vertical directions is smaller than in horizontal direction, as discovered with the previous technique. The second, the resolution reduces drastically from the measurement at 30 W compared to the measurement at 25 W, which also confirms the discovered behaviour in the previous section. Last but not least, the large increase of the horizontal spot-size unfortunately leads to a blurring of the lines perpendicular to the resolution-pattern into the line-pattern, which step by step destroys the accuracy of the measurement above 25 W for increasing power (compare Figure 5.13 e)).

5.3 Summary

In this section the results of the knife-edge measurements and the results of the resolution-target measurements are combined to give statements about the source size over the complete covered power range, as each different measurement provided complementary information within a part of the power range. In summary, the measurements and the investigation of the obtained results yielded the possibility to separate the source size with respect to the power in three different parts:

1. Region up to 30 W: The behaviour of the spot-size in this region is almost linear with a very small slope, whereupon the size in vertical direction seems to stagnate at a value below $4\mu\text{m}$ up to a power of 20 W as one can see in Table 5.2. As mentioned, the increase at 30 W is induced by the much faster increase of the horizontal spot-size. Nevertheless, the horizontal spot-size also stays at almost the same value of $\approx 5.3\mu\text{m}$ and increases abruptly at 30 W. Of course these values are rather of qualitative than of quantitative nature, but in correspondence with 'X-RAY WorkX' theses results are also in good agreement with the predictions of the source's data-sheet [42] with a resolution of $2\mu\text{m}$.

2. Region between 30 and 50 W: In this region the size of the source undergoes a steep increase, which is induced by changes of particular source components. As mentioned, the reason is the prevention of melting down the target, due to the increasing intensity of the electrons impacting on the target and the corresponding increase of heat deposition within the impact region. In this small range of 20 W the spot-size increases in the vertical direction around a factor of about 2.5 and in the horizontal direction around a factor of about 4, respectively, whereupon these factors hold for each particular measurement regardless of particular energy of the measurement cf. Figure 5.7.

3. region above 50 W: The third region finally, has again a more moderate increase of the spot-size in each direction. After the rapid change of the focussing of the electron-optic inside the source in region 2, the focussing is again stabilized and is able to slowly increase the spot-size in each direction, because due to the strong increase of the impact area in the first place, the damaging of the target is not any more an issue over a large power range.

In general, the shape of the source spot is in good approximation an ellipse of Figure 5.11, whereupon the semi-major axis lies in horizontal direction, as the spot-size in horizontal direction is always much bigger than vertical direction caused by the beam geometry cf. Figure 5.9. Thus the resolution will be much better in vertical direction than in horizontal direction. For a more precise investigation and confirmation of these values a resolution-target with smaller line-patterns, leading a drop down to 0% of the MTF, or a detector with smaller pixel size is required to be able to resolve the edge over the whole power range and hence be able to properly determine the FWHM of the source size.

6 Spectra measurements

In this chapter the spectrum of the X-ray source itself and the spectrum which remains after passing through the different gratings of the interferometer is characterized. In addition, the phase-stepping is measured energy resolved, which allows to quantify at which energy the visibility of the stepping is maximized.

6.1 Measurement procedure of the different spectra

In this section, the substantial procedure and the different parameter of the measurements are presented. First of all, measuring any spectrum an energy-resolved detector is needed. Here, the detector used for the measurements is an AMPTEC XR-100T-CdTe X-ray detector provided by 'GE global research'. The active-layer of this detector consists of Cadmium-Telluride (CdTe), which is excellently sensitive for the detection of X-ray photons with energies up to 100 keV. The active area of the detector is $5 \times 5 \text{ mm}^2$, has a thickness of 1 mm and is covered by a Beryllium window due to reasons of protection. To prevent the saturation of the detector, the active area is additionally covered by a lead pin-hole collimator with a diameter of 1 mm. As the focus of this chapter lies on the characterization of the spectra, the properties of the detector are not presented in further detail, hence the interested reader is referred to [2, 31].

As mentioned in section 3.1, the target of the source consists of tungsten, which is a metal with high density. To be able to calibrate the detector before the measurements, it is indispensable to know at least the energies of two characteristic emission peaks of the target material. The detector only consists of channels at which the different charges, produced by charge separation of the particular photons with distinct energy impacting on the active-layer are stored. Each of these channels stores a distinct amount of charge, which afterwards can be converted with aid of the characteristic peaks to eV units. The $k_{\alpha 2}$ and $k_{\beta 1}$ emission peaks of Tungsten used for the calibration appear at energies of 57.981 and 67.244 keV, respectively. The values were looked up at [35]. Additionally, in contrast to conventional X-ray sources at which the exit window of the tube consists of Beryllium to keep the vacuum and to provide nearly non-dissipative emission of the X-rays, the window of this source is made of Aluminium. Due to that, low energy photons are filtered out of the emitted X-ray beam, which changes the shape of the spectrum. This fact has to be kept in mind for the later discussion of the obtained spectra. For the measurements the detector is placed at the same position as the flat-panel detector. After the calibration, the 'raw' spectrum of the source is measured at first at different

peak energies of 60 and 80 kVp with a power of 10 W and a measurement time of 300 seconds, to get a clue of the behaviour of the spectrum within these two different energy ranges. Subsequent, the different interferometer gratings are put step by step between source and detector with the same parameter settings, to characterize the influence of the different gratings onto the spectrum, which is usually recorded by the flat-panel detector. To come as close as possible to the spectrum which is usually recorded, the gratings are aligned to each other in the same way as before a usual measurement. In addition to these measurements, the spectrum of each particular step of the phase-stepping process is measured. These spectra are processed afterwards in the same manner as described in section 2.2. This offers the possibility to quantify the energies of the spectrum which provide the best fringe-contrast and hence the best visibility for the set of these interferometer gratings. The measurement is performed at a peak-energy of 100 kVp a power of 100 W and an integration time of 60 seconds at each step.

To obtain the results in a more quantitative way an additional treatment is needed. The spectrum of the source is exposed on its way to the detector to several external influences, as interaction with air absorption at the Beryllium window of the detector etc. Therefore, the spectra have to be corrected with the linear attenuation coefficients μ and the thickness of the respective materials to obtain the 'true' spectrum. Secondary, the spectra are corrected with the linear absorption coefficients of CdTe and CsI, which is the active-layer material of the flat-panel detector, to show the spectrum 'seen' by the standard Paxscan flat-panel detector of the setup.

6.2 Results and discussion

In this section the outcome of the measurements described above is explained and discussed. First of all, it is important to know that Cadmium-Telluride has some special properties which are hardly treatable. Besides the almost perfect efficiency over a broad energy range, the material has a negative side-effect, which has to be kept in mind for the interpretation of the measured spectra. This side effect are so called *escape events*. These events appear, when X-ray photons with energies above the K edges of Cd and Te, 26.704 and 31.8 keV, respectively, undergo photoelectric interaction within the active-layer material. After the interaction the Cd and Te atoms are left at an excited state. While relaxing back into the ground state the atoms emit characteristic X-rays without any predominant direction. Hence it happens that some of these photons are emitted in reverse direction and thus are able to leave the detector material. If this is the case, an X-ray photon that deposits lets say an energy of 60 keV is only counted as a photon with an energy between 33 – 36 keV or 28 – 33 keV depending on the atom of interaction. Due to that there are much more events counted around the K edges of the detector material and additionally photons with energies just above the absorption edges are shifted to low energies, which distorts the whole spectrum. For a more detailed insight in the different effects see [28].

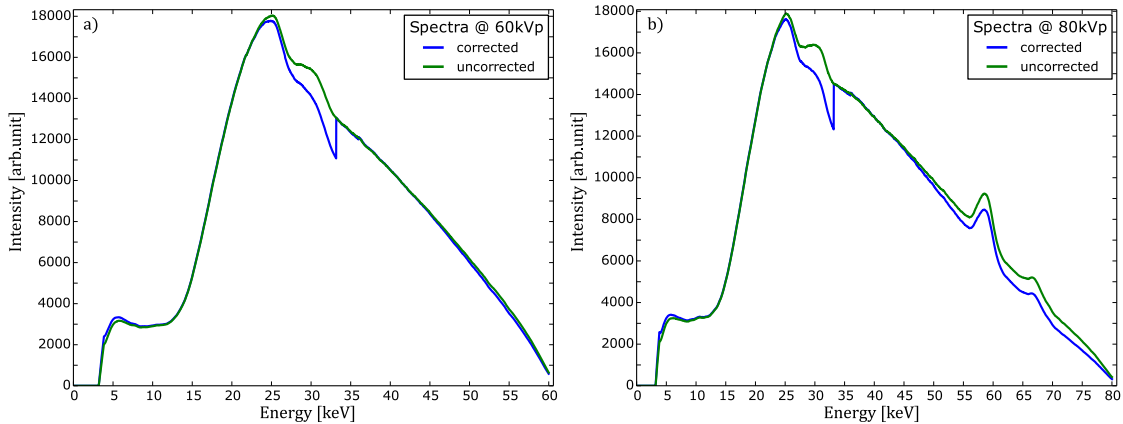


Figure 6.1: Comparison of the corrected and uncorrected source spectra for different peak energies. 'Corrected' in this case means conversion of the measured spectrum into the spectrum which is recorded by the flat-panel detector. a) Comparison of the measured and the corrected spectrum at an energy of 60 kVp, with no characteristic tungsten peaks. b) Measured and corrected source spectrum at an energy of 80 kVp with visible characteristic tungsten peaks at 58 and 67 kVp. The increase of the intensity with its maximum around 23 keV is induced by intrinsic properties of the CdTe detector material.

To overcome this there are some software tools provided by *AMPTEC Inc.*, but they are too expensive to buy them for a few corrections.

6.2.1 Source spectra at different photon- energies

To have an impression of how the source spectrum looks like for different acceleration voltages, spectra at 60 kVp and 80 kVp are compared. The results are shown in Figure 6.1. Here, the spectra measured by the CdTe detector are denoted in both plots in green and the corrected spectra with respect to the CsI of the flat-panel detector are denoted by the blue line. The absorption of X-rays due to interaction with air molecules was not accounted for, because the absorption by air is given in every measurement and thus treated as an 'intrinsic' property of the setup. In Figure 6.1, a) shows the spectrum at 60 kVp and b) at 80 kVp. The difference between the corrected and uncorrected spectrum is almost not visible in a), whereas in b) the difference gets bigger, as the efficiency of CsI compared to CdTe is similar, but its getting worse at higher photon energies. The only difference clearly visible in both plots is the intensity drop at 33 keV, which is caused by an absorption edge of CsI at this energy. Due to this, the values of μ_{CsI} drop down close to zero, which causes a big change in the correction factor based on the 'Lambert-Beer Law'. The Peaks with the highest intensity in both plots are caused by the escape

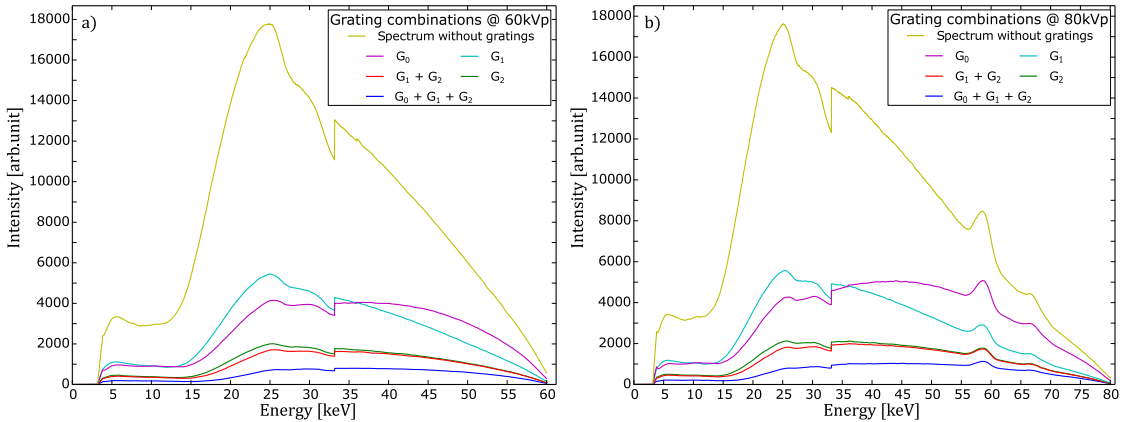


Figure 6.2: Illustration of the influence of different interferometer-gratings and their combinations onto the source spectrum at different maximum photon energies. a) Comparison of the reduction of intensity onto the source spectrum at 60 kVp, caused by the attenuation due to the different interferometer gratings. b) Comparison of the same spectra at an energy of 80 kVp. A striking feature is the strong intensity reduction at the spectra with the phase grating inside the beam. Possible explanation are 'escape events' an intrinsic property of the detector material.

events explained at the beginning of the section and can unfortunately not be removed with easy methods. In addition, there should be almost no intensity measured below ≈ 15 keV, because the Aluminium window of the source functions as a filter for low energy photons. In comparison the spectra for the different acceleration voltages look quite similar besides the fact, that in a) none of the characteristic tungsten peaks are visible in contrast to b) where the peaks appear.

6.2.2 Influence of the gratings onto the source-spectrum

After comparison of the 'raw' source spectrum with the CsI weighted spectrum, the influence of the different interferometer gratings and combinations of them is investigated. The changes of the spectra at different peak energies are illustrated in Figure 6.2. For a better comparison the respective corrected 'raw' spectrum of Figure 6.1 is added to the particular plots. a) shows the influence of the gratings at 60 kVp and b) at an energy of 80 kVp, respectively. The measurement time and power were kept at the same values as mentioned above. Both plots show a drastic reduction of intensity regardless of the respective grating put into the beam. One very interesting result strikes the eye comparing the spectra for G_0 and G_1 in both plots. Usually one expects a much better reduction at higher energies for the case of the source grating, as the G_0 is an gold absorption grating and the G_1 is a nickel phase grating with a height of only $8 \mu\text{m}$. A

possible explanation is maybe again the appearance of escape events. As the occurrence of these events has a highly statistical origin it can happen, that during one measurement more photons 'escaped' than in another measurement. This could explain the decrease of the spectrum with the G_1 at higher energies, because there is an increase of intensity around the energies of the escape peaks of 27 and 31 keV. In contrast, the source grating absorbs much more up to higher energies, that's why the region around the escape peaks is flattened, because much more photons with such energies are filtered out by the gold-grating. In addition it is also possible, that the distance from source to grating plays an important role, because the content of gold inside the beam is much less for G_0 than for the analyser grating G_2 . This explains the shift of the spectrum with G_2 over the whole energy range to lower intensities and the higher intensities at higher energies of the spectrum with G_1 compared to the spectrum with G_1 . The absorption strength of the nickel phase grating G_1 becomes very clear by comparison of the spectrum with solely G_1 and the spectrum with the combination of G_1 and G_2 . The result is, that the phase grating has only a small influence and also just at lower photon energies. This improves the assumption for phase measurement, that the phase grating is only affecting the phase of the intensity-pattern but not intensity itself, whereupon in contrast the loss of intensity compared to the 'raw' spectrum is proportionally strong. It is not surprising that the spectrum for the all three gratings inside the beam is strongly reduced, but this has also a positive effect, because the maximum of intensity is shifted to the design energy of the interferometer of about 45 keV.

6.2.3 Energy resolved phase-stepping and Energy-visibility map

In this part the results of the spectra measured at each particular step of the phase-stepping routine are presented. The big advantage of the measurement with a energy resolved detector for this technique, is the possibility to resolve the intensity variation during each phase step for each particular energy, whereupon in contrast with a conventional integrating detector only the averaged variation can be observed. The spectra at the different grating positions are depicted in Figure 6.3 a). In this graph, due to reasons of simplicity, the uncorrected spectra are presented, as is would make no difference with respect to the variations among each other, because the correction affects each spectrum in the same manner and thus would only rescales the whole graph. The graph shows the 8 steps over one G_1 -grating period of $5\text{ }\mu\text{m}$, which are usually used to retrieve the induced phase shift of an object onto the X-ray beam. Here, the focus lies on the difference between the particular steps, whereupon at the first glance only one energy region indicates big variations. This region lies between 30 and 55 keV which is no wonder, because the interferometers design energy for the first fractional Talbot distance is 45 keV, which thus is explained perfectly. To get a more quantitative insight at which energies big variations occur, the bunch of steps is processed with the same algorithm explained in section 2.2. As result the visibility at each energy can be obtained. The result is shown in Figure 6.3 b). The first thing which strikes the eye is the fact, that there are three regions with feasible visibility, which also means that in a) variations also at other

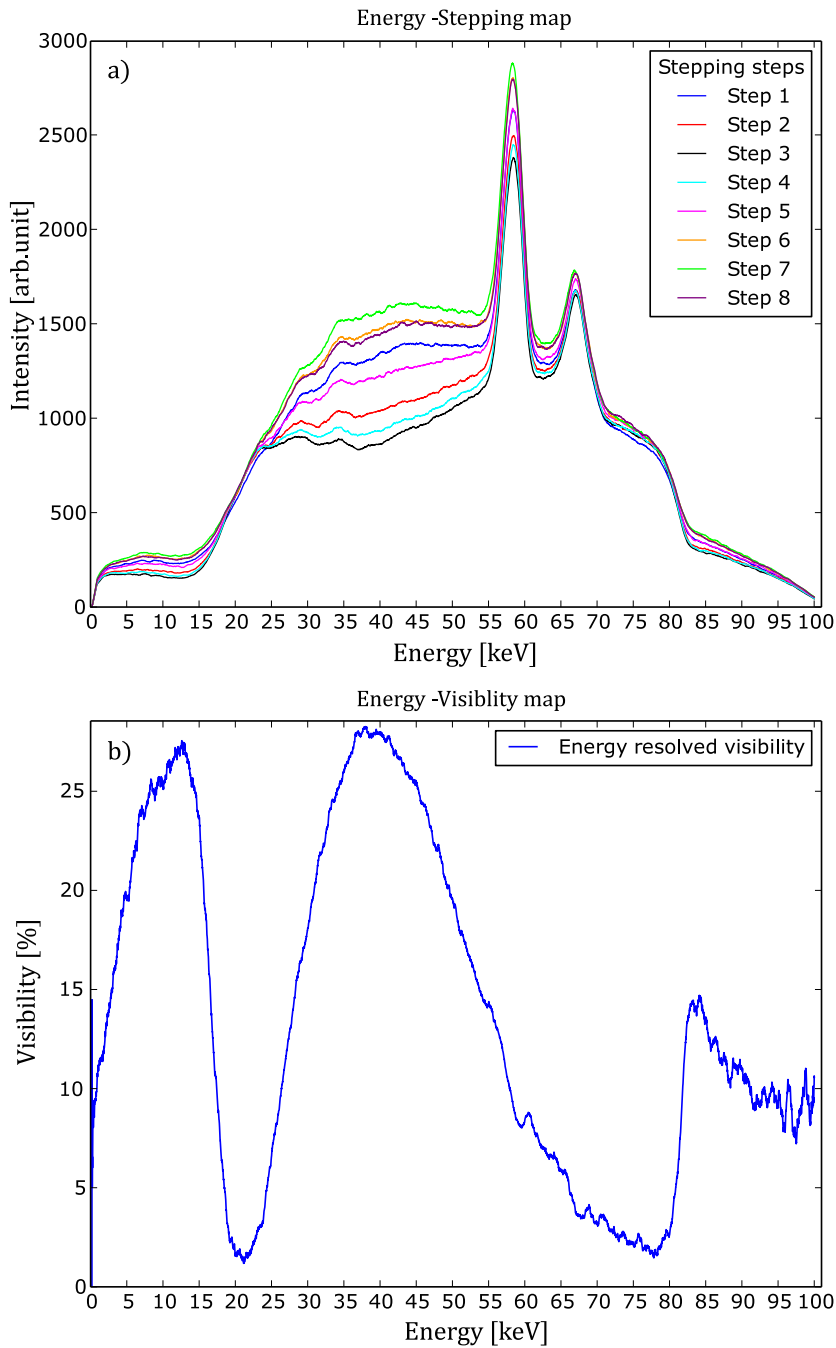


Figure 6.3: Illustration of the results of the phase-stepping procedure and related visibility. a) Energy resolved plot of the intensities during the phase-stepping. b) Resulting energy-visibility map obtained from the phase-stepping in a). The highest visibility occurs around 35 – 45 keV, which is the design energy of the interferometer. The increase of visibility above 80 keV is due to the gold absorption-edge, which enhances the photon-absorption of the analyser grating up to higher photon-energies.

energies occur. One of the two other region appears at low energies which is not that easy to explain, because at this region there should be almost no intensity due to the filtering of the sources Aluminium window. A possible explanation is the influence of 'low energy events' induced by the detectors material properties. Nevertheless, this region coincides with the region of the third fractional Talbot distance of the interferometer, so there should be some visibility. The third region with practical visibility arises after an energy of 80 keV. The increase after this energy has a very simple explanation. The visibility enhances after this energy, due to the absorption edge of gold, the absorption of gold is strongly increased, which also increases the variation between the particular spectra. The reason why the two additional regions are not visible in a) is quite simple. The visibility is determined by the relative variation between the particular curves at each energy, hence it is obvious that the two regions are not visible due to the scaling to see the whole spectrum. In contrast, the region between the two maxima has almost none visibility, because this region lies in between the fractional Talbot distances, which results in no intensity pattern.

6.3 Conclusion

First of all it is important, that the measurements and results presented above have a more qualitative than a quantitative nature, because the detector material dependent influences as 'escape events' or 'low energy events' of course induced errors in the source spectrum. Thereby the influence is especially tremendous for the results of the first two sections 6.2.1 and 6.2.2, because there the spectra itself are compared. In contrast the results of the energy-resolved stepping and the corresponding energy-visibility-map have a more quantitative issue, because here the 'escape' and 'low-energy events' can be assumed as intrinsic property of the spectra itself and hence only contribute onto the result due to statistical variations.

Nevertheless, in general the efficiency of the setups standard detector is almost the same up to energies of 80 keV, which is important to know for pure absorption measurements, because each material needs another X-ray energy for a proper image cf. Figure 6.1.

Additionally, the gratings have a strong influence on the intensity as well as they flatten the spectrum to almost the same intensity at the different energies, see Figure 6.2. Here, the mean energy of the spectrum at an maximum energy of 60 keV is almost 45 keV, which perfectly hits the design energy of the Interferometer.

The analysis of the energy resolved phase-stepping and the corresponding energy-visibility-map in Figure 6.3 is also in good accordance, as the maximum visibility occurs around an energy of ≈ 42 keV. The arise of the second maximum visibility around 13 keV is as mentioned possibly caused by combination of several effects and has to be investigated in more detail to give a statement, if the Talbot-effect is the main reason of this feature.

7 Application of the obtained results for new measurement structures

In this chapter, the results of the previous chapters are used to test an interferometer-setup without source grating and a phase-stepping procedure without mechanical stepping of any grating of the interferometer.

7.1 Comparison between interferometer-setups

In this section, the standard interferometer setup described in section 3.2 and the same interferometer without the source grating G_0 are compared with respect to the different signals, which can be retrieved by the phase-stepping routine. The reason to neglect the source grating is motivated by the outcome of chapter 5. As explained in section 2.2.3 the source grating is needed to provide sufficient spatial coherence due to the usually big spot sizes at conventional X-ray sources. But for this case, the measurement with the resolution-target yielded a sufficiently small spot size of $\approx 4 \mu\text{m}$ for the power-range below 25 W, which is about half the period of the source grating of $10 \mu\text{m}$. This in principle allows to measure without the source grating. Omitting the G_0 , the two remaining gratings have to be rearranged between source and detector to have at the right distances for the magnification factor of 2 for the interference pattern period to match the one of the analyser-grating G_2 . The distance between source and detector is fixed to the standard length of 195.6 cm. For the determination of the different signals a test-sample is put at six different positions between source and G_1 , with the same positions of the sample for both interferometer setups. The different inter-grating or source-grating distances and the relative sample positions of the two interferometer types are shown in Table 7.1. Both setups are arranged symmetrically between source and detector.

7.1.1 Measurement procedure

To obtain values for the properties of the particular setup which can be compared easily, the measurement procedure described in the following is repeated exactly the same way for both cases. As the focus lies on the response of the setups with respect to the DPC-signal and the DCI-signal, a test-sample which consists of a region inducing a phase-shift and region inducing a Dark-field signal is built. An absorption image of this sample is depicted in Figure 7.1 a). The test-sample consists of a tube filled with water in the lower part of the image, inducing a phase shift, and a container filled with silicon-oxide

Setup (length in m)	$G_0 \leftrightarrow G_1 /$	$G_1 \leftrightarrow G_2$	sample position $S \leftrightarrow z_i / G_0 \leftrightarrow z_i$					
	$S \leftrightarrow G_1$		z_1	z_2	z_3	z_4	z_5	z_6
Standard with G_0	0.93	0.93	0.17	0.27	0.37	0.47	0.57	0.67
Standard without G_0	0.98	0.97	0.26	0.36	0.46	0.56	0.66	0.76

Table 7.1: Composition of the different distances of the particular setups and the relative sample positions of the characterization measurement, to obtain the sensitivity of the particular setup onto different signals.

micro-spheres on top of the tube, inducing small angle scattering to provide a Dark-field signal. As the strength of the signals scales by the relative position to the phase-grating, the sample is moved during the measurement to 6 different positions between the G_0 and G_1 and source and G_1 , to be able to characterize the signals for different distances between sample and G_1 . At each of these positions, the sample is measured with the phase-stepping routine described in 2.2.6. In the process, the particular images are taken at an energy of 60 keV a power of 5 W and an integration time of 3 seconds for each step. The processing of the images at each position yields the three contrasts Signal of the Amplitude modulation (AMP), DPC, DCI and additionally a visibility image. To provide good reference values for the visibility, the centre of the image containing the visibility-values of each particular detector pixel, is averaged to get one mean value. The image of the dark-field signal is treated in the same way, with the exception that the averaged area differs. Here, the Region of interest (ROI) is chosen in a way that only pixels containing information of the test-sample providing a DCI-signal are accounted for in the averaged dark-field value, see Figure 7.1 c). The induced phase-shift is extracted from the DPC-image with a simple line-plot perpendicular to the horizontal-direction, which is averaged over a region of about 200 pixel-rows. the ROI is for this purpose lies at the border of the tube filled with water, which induces a phase-shift, see Figure 7.1 b). Such a line-plot for example is depicted in Figure 7.1 d), which is averaged over the blue ROI in a). The induced phase-shift reaches its maximum at the border of the plastic-tube and the water.

7.1.2 Results and Discussion

In this section the results of the measurements for the different interferometer-setups are compared. First of all, the visibility of the particular setups was almost constant during the different measurement positions, thus the mean visibility averaged over all six positions is presented. The mean visibility of the standard setup with G_0 is $V = 24.3\%$. The visibility of the setup without source-grating is $V = 18.3\%$, which is a bit less compared to the setup with G_0 , but is still sufficient for measurements. As mentioned above, the DPC- and the DCI-signal are dependent on the relative position to the phase-grating. The sensitivity of the phase-signal is assumed to be linearly increasing from

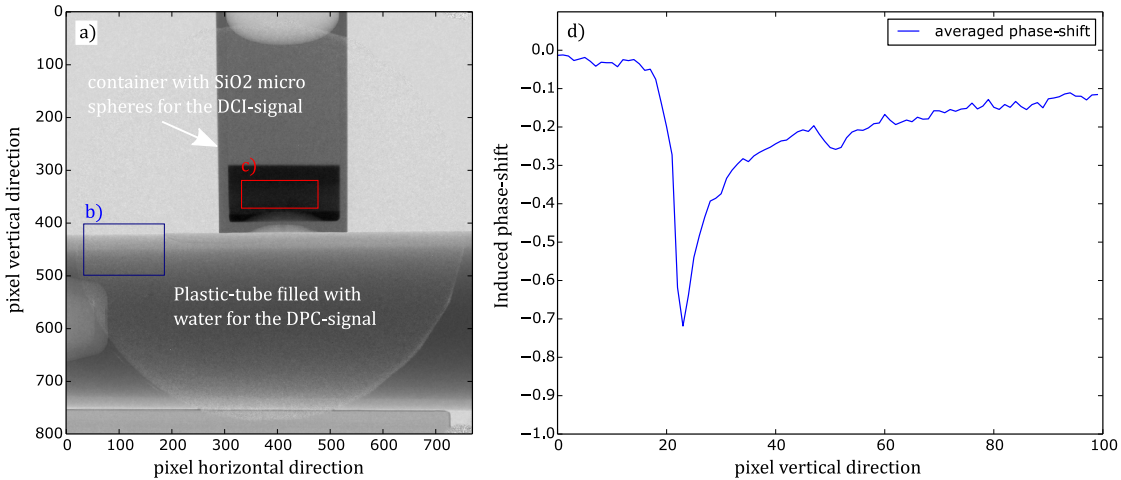


Figure 7.1: Illustration of the data-acquisition for the different signals. a) Absorption image of the different samples with different ROIs, measured at the standard setup without G_0 . b) ROI for the determination of the phase-shift induced by the water in the tube. c) ROI for the determination of the DCI-signal induced by the micro-spheres. d) Phase-shift averaged over the ROI of b), the projection-plane is perpendicular to the horizontal direction.

zero at the source or the G_0 up to a value of 1 at the phase-grating. Therefore, the determined maximal phase-shifts are scaled with the respective fraction of the distances between G_0 to sample and G_0 to G_1 or the distances between source to sample and source to G_1 depending on the respective setup. The particular distances are denoted in 7.1. In contrast the DCI-signal has to be scaled with the so called correlation length ξ , which is dependent on the mean wavelength λ , the period of the phase grating, the fraction of the inter-grating distances (generally close to one due to the symmetric arrangement) and the distance between sample and G_1 . The results for the particular measurements are depicted in Figure 7.2: a) shows the maximal phase-shift in values of π , at which the crosses indicate the measured phase-shifts at the relative sample position and the dashed line shows the linear regression of the values. The slope of the regression for the measured phase-shifts without G_0 is smaller than the slope of the regression for the setup with source-grating, but the difference is smaller than expected. b) shows the sensitivity of both setups of the DCI-signal which is induced by the sample at different positions. A value of 1 in this case means no dark-field signals can be obtained because no change in the visibility occurred, in contrast a value of 0 means all visibility was lost due to small angle scattering of the sample. The obtained values are plotted over the respective correlation length x_i , which lies in the micron range. The different curves have almost the same shape, whereupon the sensitivity of the setup with G_0 is only slightly better compared to the setup without a source grating. In absolute values the difference is only about 2%.

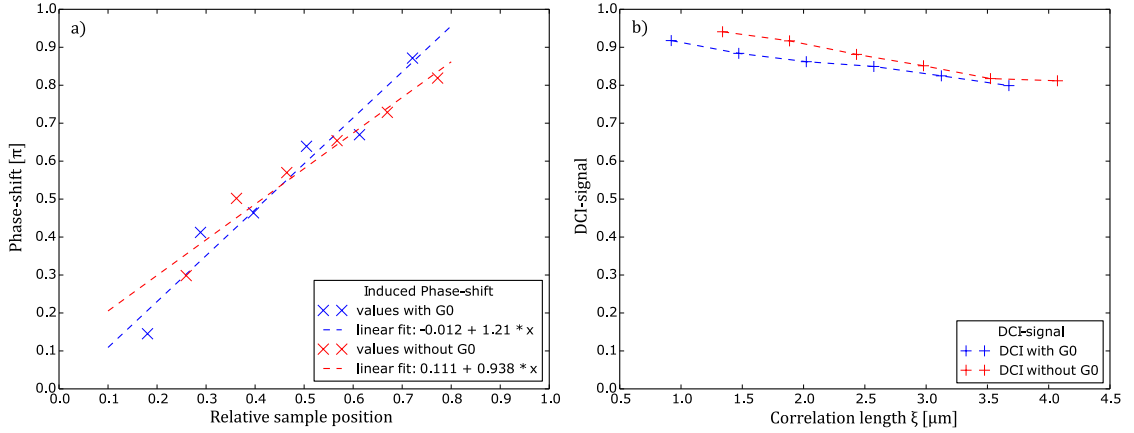


Figure 7.2: Comparison of the DPC- and the DCI-signal of the standard interferometer-setup with source-grating and without G_0 . a) Comparison of the strength of the phase-shift of the two setups, whereupon the values are weighted with the ratio between the distances of G_0 or source and sample, and the distance between G_0 and G_1 or source and G_1 . b) Comparison of the retrieved dark-field signal of the setups. Here the particular values are weighted by the correlation length ξ .

7.2 Electromagnetic phase-stepping

In this section, a proof of principle of an alternative phase-stepping procedure is presented, which has already been done in a similar way by [10]. This technique can be very advantageous, because with this method, the transition of a mechanical stepping of any grating of the interferometer to a completely electromagnetic stepping procedure can be achieved. The omission of a mechanical stepping has some big advantages, for example the induced vibrations during the stepping procedure can be minimized and the stepping can be done much faster as with some mechanical parts and the flux is twice as high for the same power. There are different possibilities to achieve such a stepping as shown in [10]. Here at this approach, the position of the electron-spot on the target is moved over the targets surface, which can be seen as equivalent to stepping the source grating G_0 . This slight change then induces the variation of the interference pattern behind the phase-grating G_1 . To obtain this change, the source-grating has to be removed, because otherwise the variation of the beam is cut out by the grating lines, which function as line-sources, as desired for the standard interferometer-setup. Hence, the remaining gratings have to be rearranged in the same manner as explained in the previous section. The movement of the electron-beam itself is possible thanks to the properties of the electron-optics of the source. With this optic it is possible to slightly change the current of the deflection magnets and thus moving the electron-beams impact point on the reflection target.

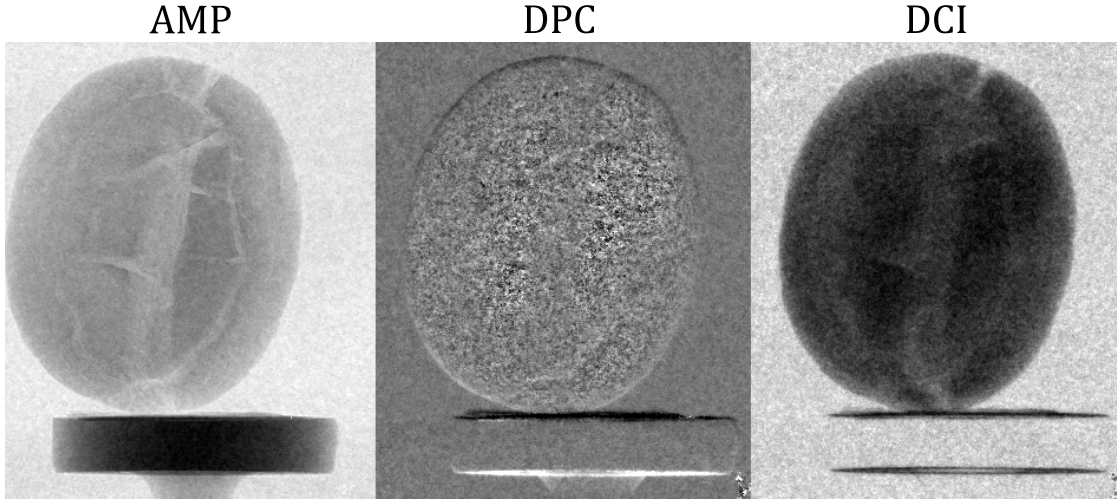


Figure 7.3: *Images of a coffee-bean measured with the electromagnetic phase-stepping approach. The different images show the different signals obtained by the processing of the phase-stepping images.*

Due to the geometry of source and reflection target and the shape of the resulting X-ray beam, see Figure 3.2 and 5.9, only the vertical direction is feasible for the stepping, as a sufficiently small spot size is needed to allow omitting the source-grating. The measurement procedure is quite similar to the standard phase-stepping, except the stepping itself. Usually the grating is stepped over a whole period of the respective grating in equidistant steps. Here, the electron-beam is moved in equidistant steps over the surface of the target over a range comparable to the period of the source-grating, in this case $10\text{ }\mu\text{m}$. For each step the current of the vertical deflection magnet was changed by 1 mA , whereupon 19 steps are needed to cover the full range of $10\text{ }\mu\text{m}$ with this current variation. At the first test a coffee-bean was measured at an energy of 60 kVp a power of 5 W and an integration time of 2 seconds for each stepping image.

The first images obtained with this approach are depicted in Figure 7.3. The three images show the three different signals obtained from the processing algorithm for a coffee bean sample. The first image shows the absorption signal of the bean. The second shows the induced phase-shift, whereupon in the middle of the bean there is almost no phase-signal, due to a lot of scattering events. The third image contains the dark-field signal. From this the reason of the destruction of the phase-signal becomes clear. Small leaves are inside the coffee-bean, which produce a very strong scattering signal and therefore destroy the phase information. This feature for example can not be distinguished in the usual absorption image. The corresponding images of the flat-field-stepping, which are also for this approach needed are shown in Figure 7.4. a) and b) show the flat-field Phase with the common Moire-fringes and the visibility of the whole image.

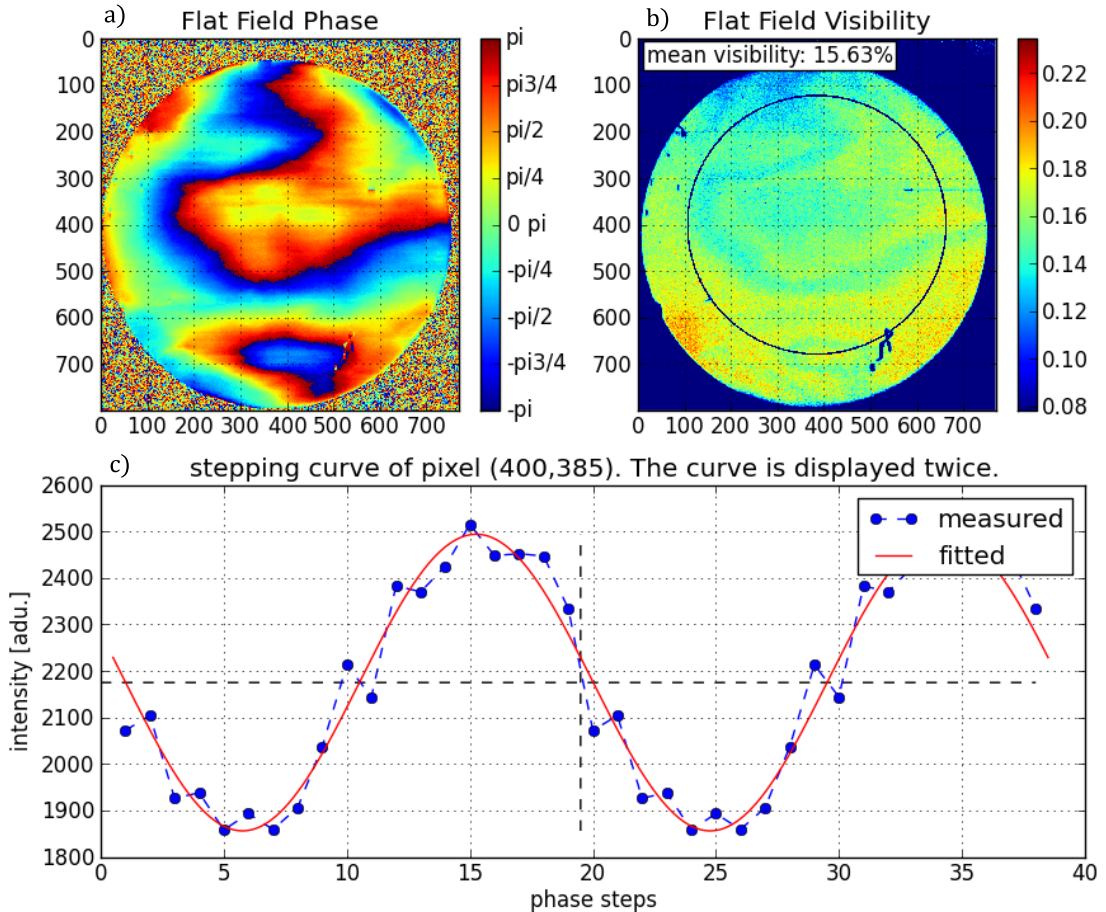


Figure 7.4: Illustration of the different signals and the stepping-curve of the stepping of the focal-spot. a) Image of the flat-field phase with Moire-fringes. b) Visibility of the flat-field phase-stepping. c) Stepping-curve of the electromagnetic stepping of the focal-spot over a range which roughly equals the period of the standard source-grating with a period of $10 \mu\text{m}$. The sinusoidal function fitted on the measured stepping values fits in good approximation the received stepping-curve.

The mean visibility is averaged over the area inside the black circle and is with a value of 15.63 % reasonably high for imaging. The more important part is shown in c). Here, the stepping curve for a central pixel is shown by the blue dots. The red line indicates a sinusoidal curve, which is the assumed behaviour of the stepping curve. The measured data and the assumed shape fit very good together, which impressively confirms the feasibility of the electromagnetic stepping procedure.

7.3 Conclusion

The presented applications in this chapter give a first hint of the further prospects, which are provided by such a small source size. The results in section 7.1 have shown, that the sensitivity of the setup without source-grating for every signal, but especial for the case of the DCI-signal, is in no way inferior compared to the sensitivity of the standard setup with G_0 . The approach in section 7.2 shows a proof of principle for an easy change from an mechanical to an pure electromagnetic phase-stepping procedure, of course thanks to the electron-optic of the source. Nevertheless, the first shot worked well, despite the fact that the visibility was about 10 % less compared to the visibility, which is achieved for a comparable standard setup including a G_0 .

8 Summary and Outlook

Here, the most important results and their implications for measurements at the characterized setup are summarized. The measurements presented in the different chapters yielded the following main results:

The time and power stability measurements showed a stable production of X-rays with an almost constant intensity over a long time scale. In addition, the increase of the intensity with varied power at a fixed electron energy showed a linear behaviour, except between a power of 25 W and 45 W, see Figure 4.3. This can possibly be explained by the change of the focussing of the electron beam at this power, in order to prevent damage to the tungsten target.

The characterization of the X-ray tubes focal spot resulted in an ellipse shaped spot size. The dependence of the spot size on the tube power can be separated into three regions: a low power region with a nearly constant small spot size up to 30 W, a region of rapid increase of the spot size up to 50 W, and again a region of nearly constant spot size for powers higher than 50 W. The vertical spot size is always much smaller than the spot-size in horizontal direction, which is mainly caused by the geometry of the source c.f. Figure 5.9. The PSF of the detector is assumed to be constant, thus the SSR of the whole system is only dependent on the behaviour of the source.

The main results of the measurement of the source spectrum and the influences of different setup parts can be concluded in two main statements. The X-ray spectrum of the source is strongly influenced especially by the two absorption gratings, whereupon the difference of the two resulting spectra can not be completely explained, yet cf. Figure 6.2. Secondly, the resulting energy-visibility-map of the second part of chapter 6 gives a very good overview over the visibilities dependency on the energy. The maximum of the obtained curve perfectly hits the design energy of the interferometer, which improves the results.

Finally, the small source size in the low power region allows for operating the grating interferometer without a source grating as presented in chapter 7. It was shown, that the setup can be operated in two-grating configuration. The resulting visibility was sufficient to perform imaging experiments efficiently, and the sensitivity was comparable to that of the standard setup. Furthermore, this configuration opens up the possibility to perform electromagnetic stepping, rather than mechanical stepping of the gratings.

Electromagnetic stepping of the source spot has the advantage that no parts need to be moved mechanically, which often times leads to vibrations. Additionally, the drawback of the source grating absorbing half the intensity can be avoided.

The use of a microfocus tube has the advantage that high resolutions can be achieved. This is of great interest for material science, where time limitations are of secondary concern. For a grating interferometer, a small spot size allows to omit the source grating, which has several advantages, e.g. higher useable flux. Currently, the achievable visibility of a two-grating setup is still below that of a comparable three-grating setup. However, the possibility to perform electromagnetic stepping showed great promise. Further research could be done to optimize the setup for this type of measurement procedure.

List of Figures

2.1	Attenuation and phase shift of electromagnetic waves	5
2.2	Simulated Talbot-carpets for a grating with a duty cycle of 0.5 a phase shift of $\pi/2$ and a grating period of $5\ \mu m$	8
2.3	Sketch of a Talbot-Lau interferometer	10
2.4	Different types of deep micro-structured gratings feasible for X-ray interferometry	11
2.5	Simulated visibility as function of Talbot-distance d_T	14
2.6	Resulting data output generated by the stepping procedure.	17
2.7	Geometric magnification in curved wave setups	18
2.8	Drawing of the edge in the centre of the beam for the measurement of the source size	19
3.1	Schematic rendering of the whole setup	25
3.2	Dimensions of the source with focussing system	27
3.3	Drawing of the relative distances between the particular parts of the setup	28
3.4	Varian detector properties	30
4.1	Dependency of the detector response onto the exposure time	32
4.2	Time-stability of the source during two days	33
4.3	Power-stability of the source with fixed energy to 60 kV	34
5.1	Pictures of the knife edge and corresponding projection image	38
5.2	Illustration of the different edge positions for the measurement	40
5.3	Illustration of the projection of an edge profile	42
5.4	Fit of the projection of the projected edge and corresponding Gauss-fits .	43
5.5	Dependency of the detector PSF	45
5.6	Results of the measurement of the source size for different directions .	47
5.7	Comparison of the two spot-size measurements at 60 kVp	49
5.8	Results for the spot-size measurements at an energy of 40 and 80 kVp .	51
5.9	Illustration of the geometry of the electron-beam and the resulting X-ray beam of the source	53
5.10	Transformed spot-size into x-y coordinates	54
5.11	Selection of ellipse-fits for an energy of 60kVp	55

5.12	First image of the resolution-target at 60 kVp and 3 W in vertical and horizontal direction, respectively.	57
5.13	Images of resolution-targets for different power	59
5.14	Illustration of the projected resolution-pattern for different power	60
5.15	Obtained MTFs for different power at an energy of 60 kVp	61
6.1	Corrected and uncorrected source spectra for different peak-energies	67
6.2	Influence of the interferometer gratings onto the source spectrum	68
6.3	Energy resolved stepping and energy-visibility map	70
7.1	Illustration of different sample ROI's to obtain the DPC and DCI signal .	75
7.2	Comparison of DPC- and DCI-signal of the interferometer-setup with G_0 and without G_0	76
7.3	Images of a coffee-bean for the different phase-stepping signals	77
7.4	Illustration of visibility an stepping-curve of the electro-magnetic stepping procedure	78

List of Tables

2.1	Results for the mismatch due to a finite edge thickness Δd at different magnifications	20
5.1	Comparison of the different detector PSFs	46
5.2	Resolution limits and correlated assumed spot-sizes	62
7.1	Composition of the different setup properties and relative sample positions	74

Glossary

Cadmium-Telluride Stable crystalline compound formed from cadmium and tellurium.

In combination with small amounts of zinc (CdZnTe) often used as X-ray and gamma ray detector with highly performance up to particle energies above 100 keV..
66

flat-field Image without any sample. Used for intensity correction of images. 35, 39–41,
56, 57, 77, 79

FWHM The full width at half maximum (FWHM) is a definition for effective width of a peak and is defined over the standard deviation σ to $FWHM = 2\sqrt{2 \log 2} \cdot \sigma$..
44, 46, 63

resolution-target Chart of different geometric profiles and line patterns with different line-thickness and distances. Generally used to determine the limiting spatial resolution of an optical system.. 56, 58, 61, 63, 73

Acronyms

AMP Signal of the Amplitude modulation. 15, 74

ASTM ASTM International (former: American Society for Testing and Materials). 37

CdTe Cadmium-Telluride. 65–67

CsI Caesium Iodine. 29, 66–68

DCI Dark-field Imaging. 15, 74–76, 78, 84

DPC Differential Phase Contrast. 15, 74–76, 84

EN Europäische Norm. 37

ESF Edge spread function. 21, 22, 37–43

FWHM full width at half maximum. 12, 23, 38, 43, 44

IEC International Electrotechnical Commission. 37

LIGA Lithography and Galvanization. 9

LSF Line-spread-function. 21, 22, 42

LSI linear and shift invariant. 20

MTF Modulation transfer function. 21, 56, 60–63

OTF Optical transfer function. 21

PSF Point-spread-function. 20–23, 40, 41, 43–45, 48, 56, 61, 81

PTF Phase transfer function. 21

ROI Region of interest. 74, 75

Sf Spatial frequency. 61

SSR Spatial system response. 21, 81

Bibliography

- [1] ALS-NIELSEN, Jens: *Elements of Modern X-ray Physics*. Second Edi. A John Wiley & Sons, 2011. – ISBN 9780470973950
- [2] AMPTEC INC.: *Datasheet XR-100T-CdTe*
- [3] BAVENDIEK, Klaus ; EWERT, Uwe ; RIEDO, Adrian ; HEIKE, Uwe ; ZSCHERPEL, Uwe: New Measurement Methods of Focal Spot Size and Shape of X-ray Tubes in Digital Radiological Applications in Comparison to Current Standards. In: *18th World Conference on Nondestructive Testing* (2012), Nr. April, S. 16–20. – URL http://212.8.206.21/article/wcndt2012/papers/346_wcndtfinal100346.pdf
- [4] BECH, Martin: *PhD Thesis X-ray imaging with a grating interferometer*, University of Copenhagen Denmark, Dissertation, 2009. – 173 S
- [5] CREATH, Katherine: V Phase-Measurement Interferometry Techniques. In: *Progress in Optics* 26 (1988), Nr. C, S. 349–393. – ISBN 0079-6638
- [6] CREMER, Jay Theodore J.: *Neutron and X-ray Optics, Jay Theodore Cremer, Jr., Elsevier, 2013.pdf*. First Edit. 2013. – 1124 S. – ISBN 9780124071599
- [7] CUNNINGHAM, I a. ; FENSTER, a: *A method for modulation transfer function determination from edge profiles with correction for finite-element differentiation*.
- [8] DAVID, C. ; NÖHAMMER, B. ; SOLAK, H. H. ; ZIEGLER, E.: Differential x-ray phase contrast imaging using a shearing interferometer. In: *Applied Physics Letters* 81 (2002), Nr. 17, S. 3287. – URL <http://scitation.aip.org/content/aip/journal/apl/81/17/10.1063/1.1516611>. – ISSN 00036951
- [9] DONATH, Tilman: Quantitative X-ray Microtomography with Synchrotron Radiation. (2007), S. 209
- [10] HARMON, Katherine J. ; MIAO, Houxun ; GOMELLA, Andrew a. ; BENNETT, Eric E. ; FOSTER, Barbara a. ; BHANDARKAR, Priya ; WEN, Han: Motionless electromagnetic phase stepping versus mechanical phase stepping in x-ray phase-contrast imaging with a compact source. In: *Physics in medicine and biology* 60 (2015), Nr. 8, S. 3031–43. – URL <http://stacks.iop.org/0031-9155/60/i=8/a=3031>. – ISSN 1361-6560

- [11] HONERKAMP, Josef ; RÖMER, Hartmann: *Klassische Theoretische Physik Eine Einführung.* Bd. 3. Albert-Ludwigs-Universität, Fakultät für Physik, Hermann-Herder-Straße 3, W-7800 Freiburg ISBN, 1993. – 349 S. – URL <https://www.freidok.uni-freiburg.de/data/82.> – ISBN 3-540-55901-9
- [12] KÖHLER, Jörg: Der Talbot-Effekt / Universität Regensburg, Institut für Experimentelle und Angewandte Physik. 2008. – Forschungsbericht. – 1–12 S
- [13] LEHNERTZ: *Erzeugung von Röntgenstrahlung.* – URL <http://epileptologie-bonn.de/cms/upload/homepage/lehnertz/Roe2.pdf>
- [14] LEI, Yaohu ; DU, Yang ; LI, Ji ; ZHAO, Zhigang ; LIU, Xin ; GUO, Jinchuan ; NIU, Hanben: Fabrication of x-ray absorption gratings via micro-casting for grating-based phase contrast imaging. In: *Journal of Micromechanics and Microengineering* 24 (2014), Nr. 1, S. 015007. – URL <http://stacks.iop.org/0960-1317/24/i=1/a=015007?key=crossref.c8d5bae0afdef4852a68c7fb41ef568e>. – ISSN 0960-1317
- [15] LEWIS, Andrew J.: *Absolute length measurement using interferometry*, UNIVERSITY OF LONDON, IMPERIAL COLLEGE OF SCIENCE, TECHNOLOGY AND MEDICINE, 2002. – 324 S
- [16] LI, Ke ; ZAMBELLI, Joseph ; BEVINS, Nicholas ; GE, Yongshuai ; CHEN, Guang-Hong: Spatial resolution characterization of differential phase contrast CT systems via modulation transfer function (MTF) measurements. In: *Physics in medicine and biology* 58 (2013), Nr. 12, S. 4119–35. – URL <http://www.ncbi.nlm.nih.gov/pmc/articles/PMC3746757/> – ISBN 1361-6560 (Electronic) 0031-9155 (Linking)
- [17] LI, Ke ; ZAMBELLI, Joseph ; BEVINS, Nicholas ; GE, Yongshuai ; CHEN, Guang-Hong: Spatial resolution characterization of differential phase contrast CT systems via modulation transfer function (MTF) measurements. In: *Physics in medicine and biology* 58 (2013), Nr. 12, S. 4119–35. – URL <http://www.ncbi.nlm.nih.gov/pmc/articles/PMC3746757/> – ISBN 1361-6560 (Electronic) 0031-9155 (Linking)
- [18] LIU, Huiqiang ; WU, Xiseng: Optimization of reconstructed quality of hard x-ray phase microtomography. 54 (2015), Nr. 18, S. 5610–5618
- [19] MICHELSON, A.A.: *Studies in Optics*. Dover Publications, 1995 (Dover books on astronomy). – URL https://books.google.de/books?id=m2tUZ4_8WGMC. – ISBN 9780486687001
- [20] MODREGGER, P ; PINZER, B R. ; THÜRING, T ; RUTISHAUSER, S ; DAVID, C ; STAMPANONI, M: Sensitivity of X-ray grating interferometry. In: *Optics express*

- 19 (2011), Nr. 19, S. 18324–38. – URL <http://www.ncbi.nlm.nih.gov/pubmed/21935201>. – ISBN 1094-4087
- [21] MOHR, Juergen ; GRUND, Thomas ; KUNKA, Danays ; KENNTNER, Johannes ; LEUTHOLD, Juerg ; MEISER, Jan ; SCHULZ, Joachim ; WALTER, Marco: High aspect ratio gratings for X-ray phase contrast imaging. In: *AIP Conference Proceedings* 1466 (2012), Nr. 1
- [22] MOMOSE, Atsushi: Recent Advances in X-ray Phase Imaging. In: *Japanese Journal of Applied Physics* 44 (2005), Nr. 9A, S. 6355–6367. – ISBN 0021-4922
- [23] MUELLER, Mark: Experimental characterization of the first preclinical X-ray phase contrast CT scanner. (2013)
- [24] PFEIFFER, F ; BECH, M ; BUNK, O ; KRAFT, P ; EIKENBERRY, E F. ; BRÖNNIMANN, Ch ; GRÜNZWEIG, C ; DAVID, C: Hard-X-ray dark-field imaging using a grating interferometer. In: *Nature materials* 7 (2008), Nr. 2, S. 134–137. – ISBN 1476-1122
- [25] PFEIFFER, Franz ; WEITKAMP, Timm ; BUNK, Oliver ; DAVID, Christian: Phase retrieval and differential phase-contrast imaging with low-brilliance X-ray sources. In: *Nature Physics* 2 (2006), Nr. 4, S. 258–261. – ISBN 1745-2473
- [26] PFEIFFER, Franz ; WEITKAMP, Timm ; DAVID, Christian: X-ray phase contrast imaging using a grating interferometer. In: *Europhysics News* 37 (2006), Nr. 5, S. 13–15. – ISSN 0531-7479
- [27] QIN, Yi: *Micromanufacturing Engineering and Technology*. Second Edition. Elsevier Science, 2015 (Micro and Nano Technologies). – URL <https://books.google.de/books?id=AqDvAwAAQBAJ>. – ISBN 9780323312677
- [28] REDUS, R: CdTe Measurement of X-Ray Tube Spectra: Escape Events Application Note ANCDE1 Rev A1. (2008), S. 3
- [29] REVOL, Vincent ; KOTTLER, Christian ; KAUFMANN, Rolf ; STRAUMANN, Ulrich ; URBAN, Claus: Noise analysis of grating-based x-ray differential phase contrast imaging. In: *Review of Scientific Instruments* 81 (2010), Nr. 7, S. 1–7. – ISBN 0034-6748
- [30] SAMEI, E ; FLYNN, M J. ; REIMANN, D a.: A method for measuring the presampled MTF of digital radiographic systems using an edge test device. In: *Medical physics* 25 (1998), Nr. 1, S. 102–113. – ISBN 0094-2405 (Print) 0094-2405 (Linking)
- [31] SCIENTIFIC CROSSROADS ; AMPTEC INC.: X R F F P S o f t w a r e G u i d e V.3.30. (2008)
- [32] SPÄTH, Helmuth: Meßdatenanpassung mit Ellipsen in allgemeiner Lage und mit vorgegebenem Achsenverhältnis. In: *VGI Österreichische Zeitschrift für Vermessung und Geoinformation* 4 (1997), S. 286–288

- [33] SYSTEMS, Varian medical: *PaxScan ® 2520DX Digital Image Receptor*
- [34] TALBOT, Henry F.: Facts relating to Optical Science. In: *Philosophical Magazine and Journal of science* (1836)
- [35] THOMPSON, Albert ; ATTWOOD, David ; LINDAU, Ingolf ; LIU, Yanwei ; GULLIKSON, Eric ; PIANETTA, Piero ; HOWELLS, Malcolm ; ROBINSON, Arthur ; KIM, Kwang-Je ; SCOFIELD, James ; KIRZ, Janos ; UNDERWOOD, James ; KORTRIGHT, Jeffry ; WILLIAMS, Gwyn ; WINICK, Herman ; THOMPSON, Albert C. (Hrsg.): *Center for X-ray Optics and Advanced Light source X-Ray Data Booklet*. 3. Berkely : Lawrence Berkeley National Laboratory University of California, 2009. – URL <http://xdb.lbl.gov>.
- [36] VAN DER VEEN, Friso ; PFEIFFER, Franz: Coherent x-ray scattering. In: *Journal of Physics: Condensed Matter* 16 (2004), Nr. 28, S. 5003–5030. – ISBN 0953-8984\1361-648X
- [37] WAGNER, Robert F.: Toward a unified view of radiological imaging systems. In: *Medical Physics* 1 (1974), Nr. 1, S. 11. – ISSN 00942405
- [38] WAGNER, Robert F.: Toward a unified view of radiological imaging systems. Part II: Noisy images. In: *Medical Physics* 4 (1977), Nr. 4, S. 279. – ISBN doi:10.1118/1.594362
- [39] WEITKAMP, Timm ; DAVID, Christian ; PFEIFFER, Franz: Tomography with grating interferometers at low-brilliance sources. (2006)
- [40] WEITKAMP, Timm ; DIAZ, Ana ; DAVID, Christian ; PFEIFFER, Franz ; STAMPONI, Marco ; CLOETENS, Peter ; ZIEGLER, Eric: X-ray phase imaging with a grating interferometer. In: *Optics express* 13 (2005), Nr. 16, S. 6296–6304. – ISBN 1094-4087
- [41] X-RAY WORKX GMBH: *CAD Drawings XWT-160-SE (1 : 5)*
- [42] X-RAY WORKX GMBH: *DATASHEET*. 2013
- [43] X-RAY WORKX GMBH: *X-COM software manual*. 2013
- [44] X-RAY WORKX GMBH: *MICROFOCUS X-RAY TUBES PRODUCT LINE SE*. 2015
- [45] XIN, Liu ; JIN-CHUAN, Guo ; XIANG, Peng ; HAN-BEN, Niu: Visibility in differential phase-contrast imaging with partial coherence source. In: *Chinese Physics* 16 (2007), Nr. 6, S. 1632–1636. – ISBN 1009-1963
- [46] YASHIRO, Wataru ; TAKEDA, Yoshihiro ; MOMOSE, Atsushi: Efficiency of capturing a phase image using cone-beam x-ray Talbot interferometry. In: *Journal of the Optical Society of America. A, Optics, image science, and vision* 25 (2008), Nr. 8, S. 2025–2039. – ISBN 9780198567288

Statement of Authorship

I hereby declare that I have completed the present thesis independently and only with the named literature and aids. The thesis in this form or in any other form hast not been submitted to an examination authority.

Garching, Tuesday 17th November, 2015

.....
Markus Baier

